Computational Simulation of Urinary System

Ghazaleh Hosseini
School of Engineering and Material Sciences
Queen Mary University of London

Professor John Williams

A thesis submitted in conformity with the requirements
for the degree of Doctor of Philosophy
University of London

Abstract

The aim of the present study is to create a computational model of the ureteral system that accurately mimics its dynamic functionality. This model will be able to replicate the peristaltic movement of the ureter for a variety of physiological conditions. The objective of this research was met using our in-house fluid solid interaction model, known as coupled Cgles-Y-code in which the moving boundaries between the solid and fluid domain were replicated using a novel immersed boundary method. First, a comprehensive literature review on ureteral physiology was conducted with a focus on the anatomy of the ureter and theories behind mechanisms of ureteral peristaltic function in various physiological and pathological conditions. Next, the nonlinear tensile properties of the ureteral wall were integrated into the Y-code using the equivalent strain method and the resulting model was compared with a model with linear tensile properties. It was shown that the implementation of nonlinear tensile properties was more accurate and more closely matched the behaviour of the native ureteral wall. Next, the development of more anatomically accurate ureter model geometry was presented along with a variety of approaches to optimise the mesh resolution for this complex model. A new algorithm was then developed in order to model the Intra-Abdominal Pressure (IAP) into the Y-code. Next, two separate contraction models, constant radial and time-window-frame, were introduced. It was observed that a use of the time-window-frame contraction model coupled with the IAP algorithm exhibited a better agreement with the existing clinical data than the constant radial contraction model. Finally, a comprehensive study was conducted on the urodynamic responses when different pathological conditions are modelled. The results from using a linear tensile model, replicating an unhealthy condition, showed a high level of shear stress around the contraction lumen and a higher urine velocity in vicinity of the contraction region. In another scenario, a highly depressed amplitude of peristalsis, known to be a consequence of taking vasodilators, was simulated. It was shown that an inefficient contraction can increase the possibility of continuous reflux during the propagation of peristalsis.

Acknowledgements

First and foremost I thank my beloved mom, Tooran, for her constant love, efforts and guidance. I also thank my sister and her families for their continuous support, care and love. I thank my supervisor, Professor John Williams, for his instruction and understanding during this project. I thank my second supervisor Dr. Eldad Avital and my colleagues Professor Chuning Ji and Dr. Dong Xu without their support and guidance I would not have been able to finish the project. I thank many people in the QMUL support staff; in particular Dr. Zahir Ikram for his expertise, professionalism and patience. Finally, I thank all my friends and colleagues I have made over the course of this work for the useful discussions. Special thanks go to my husband, Dr.Amin Rezaienia and my friends, Dr.Gordon Paul, Dr.Siamak Akbarzadeh and Dr.Xin Bai, for helping me with the edition of my thesis.

Dedications

I would like to dedicate this thesis to bright memory of my dear father who always wanted me to be successful.

Nomenclature

Greek

E	Youngs modulus
μ	dynamic viscosity
ρ	density
ν	Poissons ratio
$\bar{\mu}$	damping
T	Cauchy Stress
λ	Lam's First Parameter
G	Shear Modulus
E_d	GreenSt.Venant strain tensor

Abbreviations

ALE	Arbitrary Lagrangian Eulerian
CAD	Computer-Aided Design
CBCT	Cone Beam Computed Tomography
CFD	Computational Fluid Dynamic
CG	Conjugate Gradient
CT	Computed Tomography
CV	Control Volume
DEM	Discrete Element Modelling
DICOM	Digital Imaging and Communications in Medicine
F	Force
FD	Full Distribution
FDEM	Finite-Discrete Element Method
FE	Finite Element
FR	French Catheter Size
FSI	Fluid Solid Interaction
FV	Finite Volume
HD	Half Distribution
IB	Immerse Boundary
IAP	Intra-Abdominal Pressure
IPM	Incompressible Projection Method

IUP	Intra-Uretic Pressure
IVU	Intra Venous Urogram
Q	Flow-rate
P	Pressure
MRI	Magnetic Resonance Imaging
MPI	Message Passing Interface
Re	Reynolds Number
UVJ	UreteroVesical Junction
PUJ	Pelvis Ureteric Junction
RMP	Resting Membrane Potential
RHS	Right Hand Side
T	Time
UTI	Urinary Tract Infection
u	Velocity
V	Volume
VUR	VesicoUreteral Reflux

Contents

List of Figures

List of Tables

Chapter 1

Introduction

1.1 Motivation

Ureteric peristalsis modelling and its potential application in medicine and industry has been investigated by many researchers [1, 2, 3, 4, 5, 6, 7, 8, 9, 10]. The main objective of the urinary system modelling is to investigate the urine dynamic, in particular, the pressure gradient, the conditions of reflux,the behaviour of ureter during the muscular contraction or any obstruction. In order to simulate a peristaltic movement, a set of mathematical equations are used based on different parameters and boundary conditions. They can be solved either with numerical or theoretical methods to express the relationship between these parameters. Recently, research on modelling the urinary system is introducing more complex models to accurately simulate the real situation. In this Chapter (1), a description of the physiology of the ureter and its mechanical properties are discussed. A variety of publications demonstrating theoretical and computational modelelling on the ureter and urine behavior are discussed.

1.2 Anatomy of the Ureter

The ureter is a muscular tube with a length around 28-30 cm which conveys urine from the kidney to the bladder, as shown in Figure 1.1. The ureter has thick, contractile walls, and its diameter varies considerably at different points along its length. The urine in the ureter is primarily impelled by peristaltic muscular contraction acting in a wavelike manner with a uniform low speed, although gravity and hydrostatic pressure also contribute. When the bladder is filled up with urine, the lower ends of the ureters act like valves (vesicoureteic junctions) which are compressed to prevent any retrograde flow into the ureter.

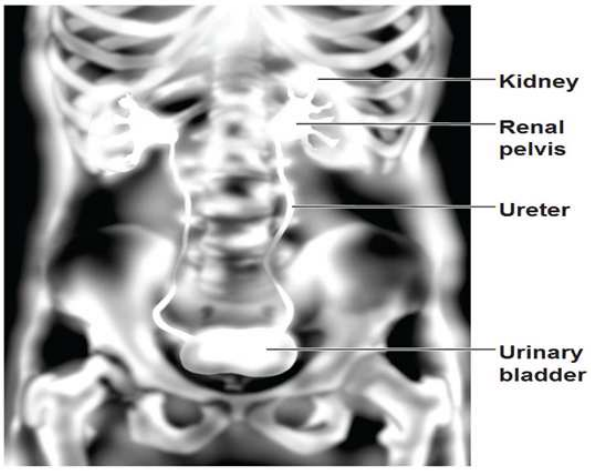

Figure 1.1: Renal System [11]

The upper and lower ureteral segments receive the sympathetic and parasympathetic innervation which can cause a change in force and frequency of ureter muscular contraction. When urine enters the renal pelvis, the contraction initiated there causes movement of the urine to the ureters. There are three layers in the ureter wall, as shown in Figure 1.2. These layers are the mucosa, the muscle coat and the adventitia. The outer layer or the adventitia is a supporting layer of fibrous connective tissue. The middle layer is a muscular coat which consists of inner circular and outer longitudinal smooth muscles.

The main function of the middle layer is to perform synchronized contractions of the muscles (peristalsis) and convey the urine to the bladder. The inner layer, mucosa, is composed of transitional epithelium and form a continuous seal with the lining of the renal pelvis and urinary bladder.

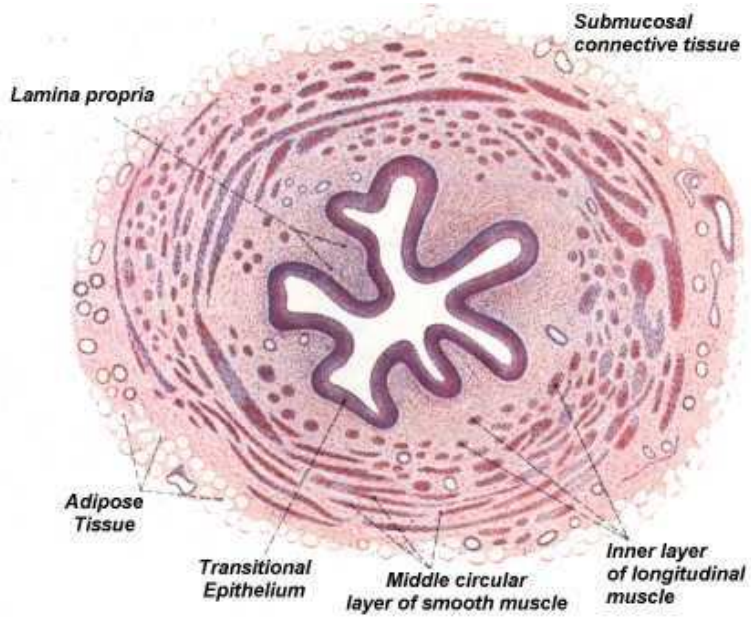

Figure 1.2: Microscopic structure of the cross section of a human ureter [12].

1.3 Ureteral Physiology

Peristaltic movement is initiated by the activity of the pacemakers region in the renal pelvis. Many researchers believe the location of the primary pacemaker is situated in the most proximal calyceal regions of the renal pelvis [1, 2, 3, 4, 5]. However, Weiss et al. [7] suggest that the primary pacemaker is located in the Pelvis Ureteric Junction (PUJ).

The ureter, like the heart, has other areas of muscle tissues and these are called latent pacemakers sites. Under normal conditions, the latent pacemakers are dominated by the activity of primary pacemakers are located in the renal pelvis. When they are not dominated by the primary pacemakers, they may act as a

pacemaker. These cells are located in all regions of the ureter. The pacemaker cells located at the UreteroVesical Junction (UVJ) cause antiperistalsis waves at a frequency lower than that of the upper segment. Retrograde peristalsis is unusual but sometimes occurs [6].

1.3.1 Propagation of Electrical Activity

The electrical activity of the pacemaker cells introduces action potentials that propagates through the ureter downwards to the bladder. This causes a peristaltic contraction in the smooth muscle cells. The electrical activity propagates from one cell to the next across cells which are close together through intermediate junctions. The conduction velocity in the ureter is around 2-6 cm/sec.

A single pacemaker region on the pelvi-calyceal border in the kidneys causes a wave of contraction. This wave propagates radially across the pelvis to create a wave that propagates distally towards the PUJ [8, 9, 10]. The ureteral smooth muscle cells membranes are polarized and they maintain an electrical potential in the resting, relaxed state. The cell contains a high concentration of potassium and is electrically negative. Depolarization of the membrane produces a characteristic action potential which is conducted downwards along the ureter. Not every pacemaker contraction of the renal pelvis propagates all the way to the ureter.

The distribution and permeability of K^+ ions across the cell membrane determines the Resting Membrane Potential (RMP) of a ureteral muscle cell which varies from -33 to 70 mV. The RMP of a non-pacemaker cell is stable and when the cell is excited by an external stimulus or propagation of electrical activity from an adjacent activated cell, the cell becomes activated. If enough of the cell membrane is depolarized to the threshold potential, an action potential will be generated and the membrane loses preferential permeability to K^+ and becomes more permeable to Ca^{2+}. The membrane then maintains a depolarized state (plateau) for a period of time and then repolarizes due to an increase in the permeability to K^+, [6], as shown in Figure 1.3.

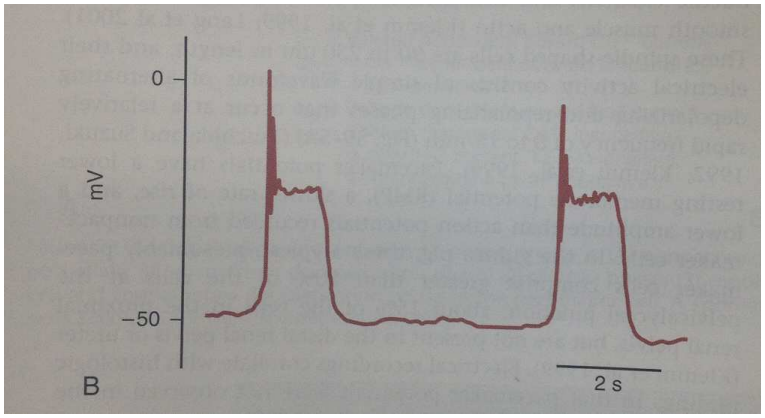

Figure 1.3: Driven action potential in guinea pig [6].

1.3.2 Effect of Diuresis on Ureteral Function

Transport of urine from the renal pelvis into the bladder in humans is affected by many variables. During normal flow, the urine between two contraction waves takes the form of a bolus which is pushed distally until it passes through the UVJ to enter the bladder. An effective contraction wave completely closes the ureteral wall.

Many studies have investigated the effect of flow rate and pressure amplitude on the frequency of the peristaltic movement by means of invasive and non-invasive methods. In-vivo studies have shown that the pressure amplitude and frequency of peristalsis can be influenced by the volume of urine production. With small amounts of urine, the renal pelvis produces only a few muscle contractions which then move down through the ureter. With a higher rate of diuresis, contractions from the renal pelvis develop until boluses coalesces and then the ureter acts as an open duct [1, 13, 14, 15, 16].

Although any parts of the pelvicaliceal system and ureter can start the contraction, the proximal part of the ureter has the highest contraction frequency due to the pacemakers. The pelvic pacemaker continues to fire at a constant rate and the periodicity of the ureteric contractions is equal to this rate. As the pelvis fills at the normal flow rate, the pressure is increased and the urine moves

to the upper ureter. When the volume of the urine in the ureter is sufficiently high , a contraction wave then passes through it. The urine, which is formed as a bolus, is propelled efficiently if the contraction closes the ureteral walls. Finally the bolus jets into the bladder.

However, Kiil [17] showed in his study that there was no relationship between the volume changes in urine flow and the rate of ureteral contraction. He found that with increasing volume of urine, the frequency of the peristaltic contraction was increased in some cases and diminished in others. He also suggested that the volume of urine transported in each contraction wave increased when urine flow increased.

Wemyss-Holden et al. [18] used an invasive fast frame renography method with ureteric spindle imaging to show that an increase of flow rate can be accompanied by no significant change in peristalsis frequency on bolus velocity in hydrated and dehydrated conditions. They concluded that the increased urine flow was affected by increases in bolus volume.

Woodside et al. [19] performed a ureteral pressure flow study in non-dilated ureters and this showed a significant linear relationship between the pressure and the perfusion rate over the range of 2 to 15 ml/min. The mean ureteral pressure of 2, 5, 10, and 15 ml/min were 4.5, 5.8, 8.3 and 10 mmHg. Their study confirms that a normal ureter responds to an increase in flow with only a moderate increase in pressure under the condition of the study.

Studies carried out by Ohlson [20, 21], described independence of contraction frequency from flow rate. His experiment on human patients demonstrated that there is a relationship between contraction frequency and body posture. Contraction intervals were significantly shorter in the upright than in the recumbent position. There were no significant differences in the patterns of contraction interval at a low and a high flow rate. Taking into account studies on the urodynamic characteristics in humans and animals leads to the conclusion that dependence of the contraction interval on flow rate appears to have been mostly observed in animals and not in humans, indicating a species difference.

The passage of urine from the renal pelvis into the bladder in a human is clearly a complex process which can be affected by many variables. For example, the effect of external pressures such as Intra-Abdominal Pressure (IAP) can be one of the important issues in the dynamics of urine flow. Karnak et al. [22] conducted an experiment in which the effect of external pressure (ureteric compression) on ureter and the Intra-Ureteric Pressure (IUP) was investigated.

The result confirmed that an increase in IAP on the ureter caused an increase in the IUP due to the wall tension. The study demonstrated that there is a high possibility of hydronephrosis (distension and dilation of the renal pelvis) as a result of increased external pressure influencing the flow of urine at a high flow rate. It is worth noting that this experiment was carried out in the absence of peristaltic contraction, and thus the diameter of the tube did not change.

1.3.3 The Myogenic Theory of Ureteral Peristalsis

The myogenic theory of ureteral peristalsis was first formed when studies indicated that ureteral peristalsis could occur without innervation. For example, peristalsis continues after ureter transplantation [23] and also after denervation of the ureter [24]. Peristalsis also occurred in an isolated in-vitro ureteral segment [13]. However, Morita et al. [3] indicated that the nervous system has a modulating role in ureteral peristalsis. That study noted that the nervous system could affect peristaltic frequency and the bolus volume.

1.3.4 Effect of Gravity

The ureteral peristaltic activity is assisted by gravity in transporting the urine through the ureter. Schick et al. [25] experimentally studied the effect of gravity on a normal dog ureter. It showed that when the dog placed head down, the antegrade peristalsis initially increased, then continued in an irregular rhythm and finally stopped. The bolus volume was decreased 50% on average. In addition, the efficiency of the ureter (number of millilitres of urine transported in bladder

each minutes) decreased as much as 62% when the dog was in a head-down position. The work done by the ureter (the number of peristaltic waves required transport 1ml) is increased as much as 360%.

1.3.5 Effect of Bladder Filling

The relationship between the ureteral intraluminal pressure and intravesical pressure (bladder pressure) has an important role in transporting the urine through the UVJ into the bladder. Ureteral activity during filling and micturition is divided in three phases: (a) phase of the free flow (b) phase of increased resistance and (c) micturition phase [6]. The phase of free flow is when the volume of urine in bladder is low. The flow of urine into the bladder is gradually stopped when the intravesical pressure is around 27-37 mmHg.

When the bladder pressure is increased, the contraction frequency increases and there is a greater amount of urine in the ureter due to the resistance of ureterovesical orifice opening. When the bladder is distended, the resistance of the uretrevesical junction is increased until transport of urine through this point is stopped. As a consequence, there is an increase in retrograde waves and the risk of retrograde flow is higher. Following micturition (bladder contraction), there is an immediate slowing of peristaltic activity.

1.3.6 Effect of the Obstruction on Ureteral Function

An obstruction influences the flow through the ureter with a magnitude dependent on the degree of obstruction, its duration, urine flow rate and occurrence of infection. When an obstruction is present, there is an increase in the baseline (resting) ureteral pressure and there is also a risk of retrograde of urine in the system. It can also increase the dimeter and length of the ureter. If the kidney continues producing urine, intraluminal pressure increases leading to an increase in length and diameter of the ureter and an increase in the volume of the urine inside the ureter. The peristaltic contraction reduces and the transport system

becomes reliant on the hydrostatic forces generated by the kidney.

1.4 Pathology of the Ureter:

There are some abnormalities which can occur in the upper tract urinary system:

- **Dysfunctional PUJ:** Dysfunctional PUJ is mainly shown by the presence of any abnormal flow occurring between the ureter and renal pelvis which consequently leads to renal pelvis dilation. Dysfunctional PUJ is responsible for a considerable number of referrals to urologists, both paediatric and adult. Figure 1.4 shows a case of hydronephrosis caused by to the reflux of urine into the renal pelvic.

Figure 1.4: Conventional IntraVenous Urography image shows the hydronephrosis in left ureter in case of disfuctionality of PUJ [26].

- **Upper Urinary Rupture:** Upper ureter rupture is considered to be another serious problem. This abnormality is a perforation of the ureter and causes a series of problems such as infection and subsequent renal impairment. There are causative factors that induce ureteric rupture, including a urinary retention, extra pressure on the ureteral wall [27, 28]. Figure 1.5

shows the leakage of the left upper urinary tract due to the rupture of the proximal part of ureter.

Figure 1.5: Postcontrast axial CT image shows leakage of radiocontrast media at the level of the upper ureter [27, 28].

- **UPJ obstruction:** A kidney stone or tumour usually can lead to an obstruction in the urinary tract and the resultant back pressure within the renal pelvis can be a source of more damage and deterioration.
- **VesicoUreteral Reflux (VUR):** VUR is another abnormality in the urinary system. It is a back flow of urine from the bladder into the two ureters, due to a malfunction in the valves in the vesicoureteic junction.
- **Primary megaloureter due to an obstruction:** A constriction at the end part of the ureter leads to dilatation. The constriction can be anatomic (anomaly of the muscle layer) or of a purely functional kind (normal histology). Above the constriction the ureter is dilated, and the wall is thickened. A primary megaloureter must be distinguished from a secondary which is due to a valve or a vesico-ureteral reflux. An infection of the entire urinary tract may cause an inflammation of the ureter which in acute situations; causes the ureter to become enlarged in both width and length.
- **Abnormal number of ureters:** Partial doubling is a rare disorder of a ureter which occurs due to an incomplete division of two ureters that

fuse again at different levels in the pelvis, lumbar, iliac or intramural regions. In incomplete doubling of the ureters there is a second renal pelvis and the upper ureter has its orifice lower down on the bladder than the lower ureter (*Weigert* and *Meyer*'s law). This abnormality often remains asymptomatic.

- **Retrocaval/Retroiliac ureter :** This is another example of abnormalities which in this case, the right ureter traces out an "S" at the L4 level behind the vena cava (retrocaval ureter). The right ureters course swings medially over the pedicle of $L_{3/4}$.

1.5 Peristaltic Motion and Diameter Variation in the Contraction of the Ureter

1.5.1 Peristaltic Motions

Ureteral peristaltic motions are the results of a combination of complicated movement of various differently aligned muscles in the ureteral wall. This is difficult to study since it is hard to analyse an individual muscle cell in isolation from its neighbours. The prevailing theory is that the circular muscles contract to cause a narrowing of the ureteral lumen, whereas, the longitudinal muscles contract to produce a shortening of the ureter. It is worth mentioning that the distribution of the outer and inner layers of longitudinal and intermediate circular muscle cells is not uniform along the ureter. These anatomical distributions produce variations in the forces that compress the ureteral wall and consequently can affect the propagation of contractions [6].

The ureteral peristalsis is combined of complex multidimensional movements of the ureteral wall. The ureteral wall contraction is not only changes in the diameter of the ureter (the transverse movement), it is involved with the axial movement, axial displacement and the rotation of the ureter. Osmon et al.[29] analysed all these movements combined together by using the video microscopic

technique. They showed the longitudinal muscles of the ureter contribute to create a vacuum effect to let the ureter segment to be filled with urine, while the circumferential muscles of the ureter aid to enclose the urine bolus within the already expanded ureteral segment and then assists the urine bolus push into downward to the urinary bladder. They also found that the synchronization between the longitudinal and circular smooth muscle is a significant factor for boules movement.

1.5.2 Diameter Variation in the Contraction of a Ureter

The change in size of the ureteral lumen during the passage of a contraction wave was studied by Woodburne et al. [30] using a dog specimen. The technique was based on the quick freezing of a section of the ureter during the peristaltic motion. From microscopic observations of the lumina, it was found that the lumen cross section had a stellate shape with five common points. Moderate urine flow rate changes the shape to a four pointed star and with a greater flow rate, the lumen becomes a square shape with a slightly curved sides. Finally, with full diuresis the lumen becomes circular, see Figure 1.6.

Although the lumen is closed completely during a contraction, Woodburnes'study [30] on dog ureter, showed that the existence of a small triangular lumen of about 0.12 mm^2 during the resting state. The segment in full diuresis (high flow rate) had a lumen of about 2 mm^2. The muscular wall becomes thin during the luminal enlargement. Both factors contribute to the enlarged lumen as shown in micrographs from the study reproduced in Figures 1.7. These Figures show the peristaltic enlargement and wave form over the above range of cross sectional areas for a length of 3cm. Weinberg [31] studied the effect of diameter of the ureteral catheter on both contractile amplitude and basal pressure level of the ureter was discussed. It was shown that an increase in catheter size from 3.6 Fr to 5 Fr resulted in a 5 mmHg rise in the basal pressure with a simultaneous increase of 35 mm Hg in the peak pressure amplitude. Fr is a unit on the French catheter scale where 3Fr is equal to a diameter of 4/3 mm.

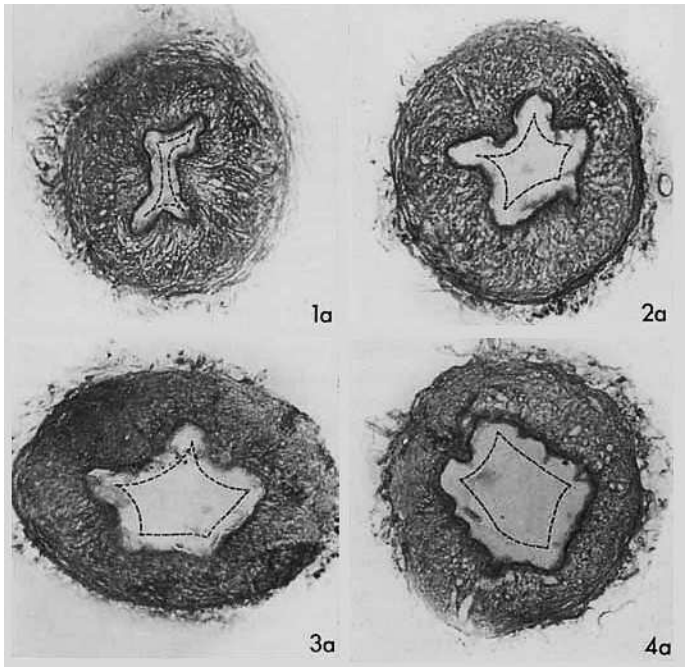

Figure 1.6: Stages of ureteral opening [30]

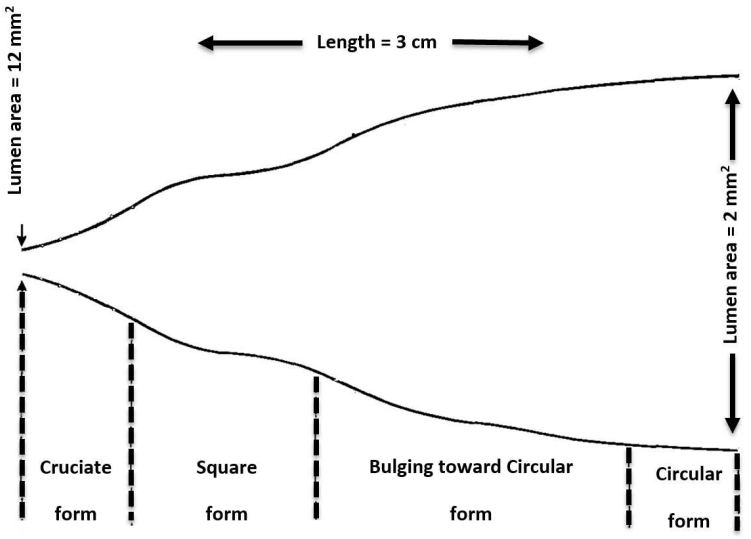

Figure 1.7: Pictorial representation of one-half of a peristaltic wave in the ureter side view. The lumen contracts to a cross sectional area of 0.12 mm^2 and opens to a cross section area of 2 mm^2 [30].

1.5.3 Effect of Drugs on the Ureter

The effect of drugs on the ureteral function has been studied by many researchers. Tilling et al. [32] used a microscopic imaging method to determine the effect of drugs such as LY274614 and Oxybutynin on peristaltic movement in rats ureters, in which peristaltic velocity and frequency, bolus length and direction of propagation were evaluated. The results showed that *Oxybutynin* caused a substantial increase in the length of the bolus and LY274614 decreased pelvic pressure, ureteral frequency and also increased the bolus length. Although, the imaging method used in this experiment is suitable for the evaluation of the anatomical aspects of the upper urinary system, the hidden structures within the renal pelvis are not very clear and the fat around both the kidney and ureter reduces transparency. Kim Davenport et al. [33] has investigated ureteral peristalsis motion under effect of the relaxation drugs such as, $Diclofenac$, $Nifedipine$, $Tamsulosin$. Their result shows that the drugs did not stop the peristalsis motion but there is 25-60% of reduction in ureteral contraction pressure and ureteral wall tension.

1.5.4 Measurements and Imaging of the Ureteral Peristalsis

Complexity of ureteral prestalsis process has led to various invasive and non-invasive methods to investigate the urine dynamics and ureteric peristalsis, namely; *X ray screening*, *Dynamic Scintigraphy*, *Doppler ultrasonography*, *Endoluminal Ultra Sonography*, *Implantable Magnetic Sensors*, *EMG*, *Impedance measurement* and external pressure transducers [34, 35, 36, 37, 38, 39]. While non-invasive techniques offer evidence on peristaltic frequency, they are not able to produce useful data on the upper urinary urodynamic system and consequently are not frequently used in clinical practice.

One invasive technique to investigate peristaltic motion is recording the uremetrogram or ureteric profilometry together with simultaneous cineradiography. Such a recording is called uremetrogram or ureteric profilometry. If the pres-

sure inside the ureter is measured with a catheter fixed in place, a recording of the pressure variations with time is obtained.

Ureteric profilometry in both normal and pathologic ureters has been recorded in-situ by means of pressure transducers. One of the first attempts was by Kiil [17] who initiated pressure measurements using electronic strain-gauge pressure transducers attached to catheters inserted into the ureter. Figure 1.8 shows an example of a human uremetrogram. This shows that, in general, the pressure in a normal ureter remains at a constant level between 1 and 6 mmHg, known as the resting pressure. This pressure periodically increases to a peak of between 20 to 40 mmHg.

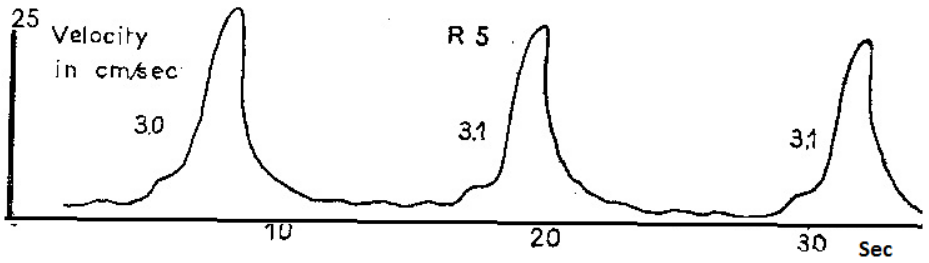

Figure 1.8: An example of an urometrogram (pressure [mmHg] vs. time [s]). The location of recording is 5 cm from the ureteral orifice [17].

Shafik [40] studied ureteric pressure profilometry in a normal and pathologic ureter.Two pressure profile patterns have been recorded in pathologic ureters including Ureteroarrhythmic (a ureteral condition when there are irregular rhythm peristalsis activities) and Silent (a ureteral condition when there is no peristalsis activities). His results show that a ureter with a normal internal diameter (as detected by an excretory urogram) might be ureteroarrythmetic which could disturb urine transport. This work also confirms, using a larger number of patients, that ureteric pressure profilometry is a diagnostically useful tool for various pathologic conditions such as strictured or refluxing ureters.

Tilling et al. [32] used microscopic imaging of the ureteral peristalsis on rats during cystometry. They investigated peristaltic velocity, frequency, bolus length, and direction of bolus propagation using indigo carmine for contrast. The velocity of the bolus was computed by measuring the time taken for a bolus to travel along

a measured distance.

Figure 1.9 shows two micrographs from this study. Image (1) shows the bolus at the beginning of the PUJ and image (2) shows the bolus located in the region of the cranial abdominal vessels. The two images were then arithmetically added and the distance between the bolus positions was measured. The micrographs shown in Figure 1.9, indicate a time difference of 0.49 s between two frames and a 5.10 mm distance traveled by the bolus, yielding a velocity of 10.41 mm/s.

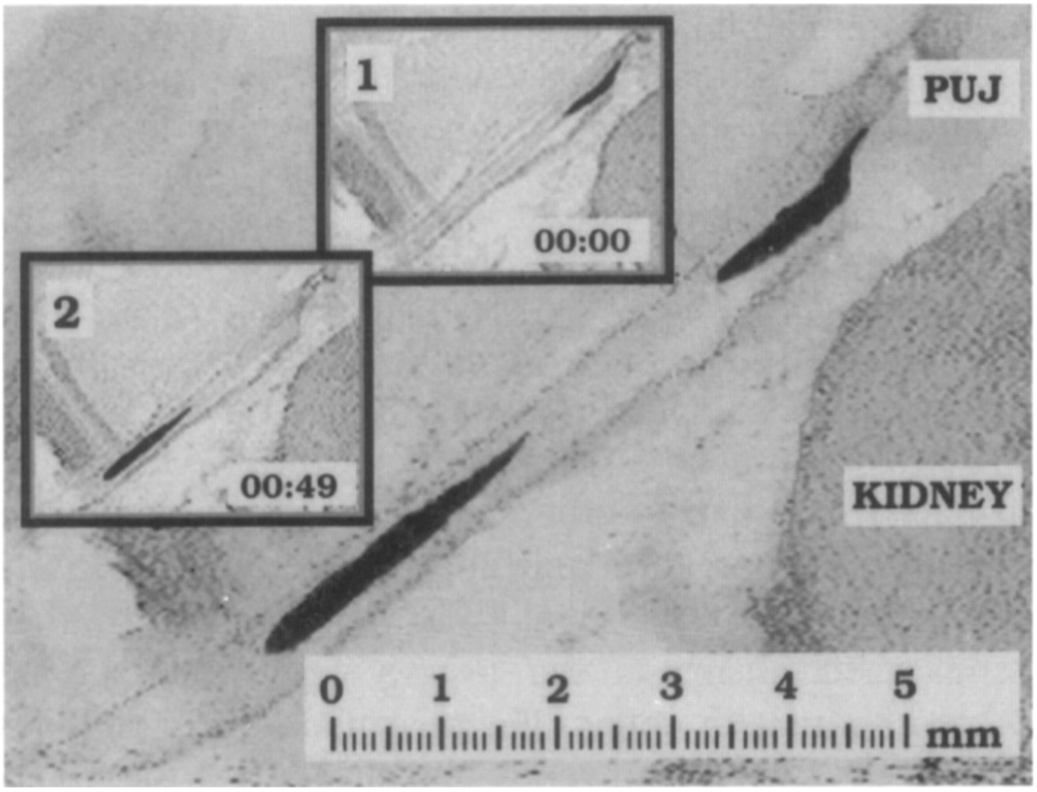

Figure 1.9: Video microscopy of ureteral peristaltic function in rats for calculation of bolus velocity [32].

Young [41] introduced an intraluminal method for pig and human ureters to study three parameters: intraluminal pressure, conduction velocity and peristaltic frequency. Table 1.1 shows the mean ureterodynamic parameters where P1 and P2 are intraureteral pressures at the tip and proximal transducers, respectively. Figure 1.10 shows the ureteral recording from pig experiments. It is worth mentioning that intraluminal devices disturb the normal function of a ureter and that the catheter might even, completely block the ureter. Such a method therefore cannot provide completely reliable results.

Table 1.1: Mean ureterodynamic parameters [41].

Parameter	Human (n=3)	Pigs (n=6)
Peristaltic interval (sec)	24 (1430)	16 (5.529)
Conduction velocity (cm/sec)	2.4 (1.72.9)	1.2 (1.11.3)
Intraureteral pressure P1 (cmH_2o)	11	18
Intraureteral pressure P2 (cmH_2o)	21	29

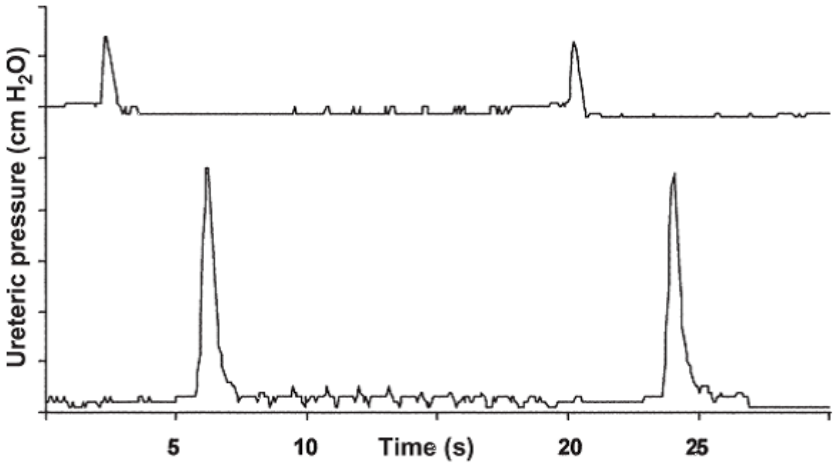

Figure 1.10: Ureteral recording from pig experiments [41].

1.6 Mechanical Properties of a Ureter

In order to simulate a computational model of a ureter, one first needs to examine its mechanical properties such as the stress/strain relationship of the wall. Watanabe et al. [42] investigated the resistance of a rupture in the transverse and longitudinal directions. Tensile tests on a human ureter were performed on samples around 5mm in diameter and a depth of 1mm. It was stretched with a constant loading speed of 5mm/min.

In Figure 1.11(a), phase one shows the relationship of the stress and stain proportionally without any tissue damage. There was a partial macroscopic rupture at phase two and some wavering of the curve was visible. In phase three, there was a decrease in stress with increasing strain. The tension in longitudinal direction was around 2.0±0.21 kgf/cm at the first yield point and 2.8±0.4 kgf/cm at the second yield point. To perform an expansion test, a physiological saline solution was injected into the ureter through a needle at a constant speed of 1.25 mL/min. Figure 1.11(b) shows an internal volume-pressure curve. The average tension of the ureter at the leak point was found to be 0.71 kgf/cm. Both the tension and expansion tests confirmed that ureter injury first occurs along the transverse direction rather than that longitudinal direction.

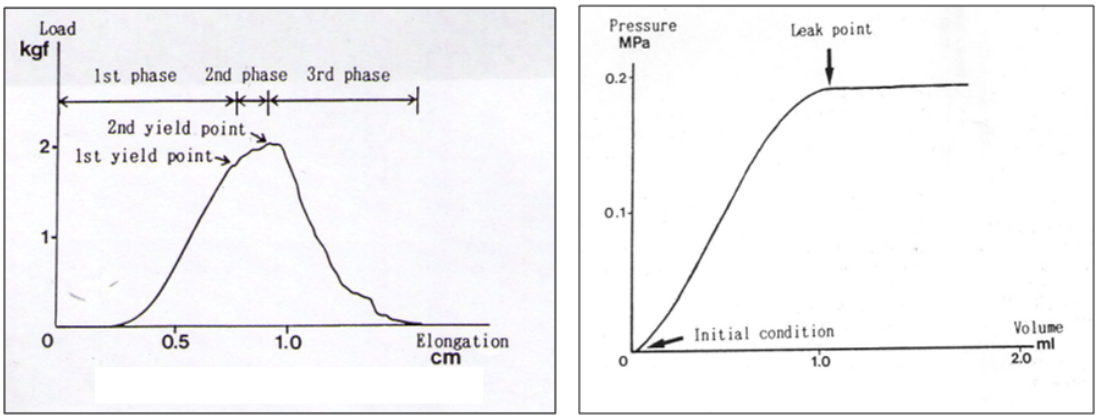

(a) (b)

Figure 1.11: (a) Stress strain relation for the human ureter, (b) Graphical results from the expansive testing of the ureter [42].

Yin et al. [43] studied the mechanical properties of isolated mammalian ureteral segments including the human ureter. In their studies, the mechanical properties in longitudinal direction are determined by using isolated segment of intact ureter subjected to simple elongation and the properties in circumferential direction are determined by using slit ring segments subjected to simple elongation. The stress and strain curve from uniaxial elongation of longitudinal segments for ureters are illustrated by typical results shown in Figure 1.12.

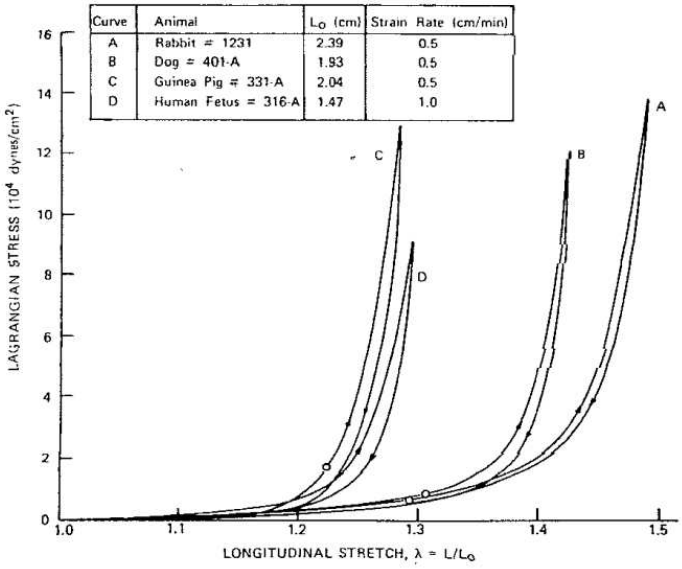

Figure 1.12: Stress /strain curve of human and animal ureter [43].

They also studied the stress relaxation test and creep test on human ureter. In stress relaxation test, a decrease in force as function of time was recorded after the specimen was stretched at a moderate strain rate to a desired strain level. In the creep test, elongation as function of time was recorded after an imposed a step constant stress on specimen. It is evident from curve shown in Figure 1.12 that the stress strain relationship for the ureter is nonlinear and that stress is not only depended on the strain but also strain history. The history depended part is time depended and it is related to the hysteresis, stress relaxation and creep. Fung [44] represents this curve as an exponential functions as presented

in Eq. 1.1:

$$\Delta T_i = T_{i+1} - Ti = (e^{\alpha^{\Delta\lambda}} - 1)(T_i + \beta) \tag{1.1}$$

where λ is the ratio of the instantaneous length divided by the reference length which will be referred to as the longitudinal stretch ratio or simply stretch, T is the stress,

α, β, T^*, and λ^* are experimentally determined constants. T^* and λ^* are a pair of specified stress and strain levels, and α and β are the elasticity parameters in the range of λ tested. If one plots $dT/d\lambda$ vs. T, α represents the slope of the line and β represents the intercept on the T axis.

Since the stretch ratio λ is dimensionless, the constant α is also dimensionless, i.e., it will be the same in any consistent units of measurement. The units of β is stress, such as dynes per square centimeter or grams per square centimeter. The constants α and β are undoubtedly related to the structure of the tissue-to the details of how the collagen and elastin fibers or fibrils arranged and coiled in the ground substance and how they interact at the points of contact with themselves or with each other-as well as to their intrinsic elasticity.

The higher the collagen content and the straighter the fibers the larger is the value α. The product $\alpha\beta$ represents the elastic modulus $dT/d\lambda$ at zero tensile stress ($T = 0$). If the material is intrinsically linear, so that it obeys Hooke's law of elasticity, then $\alpha \to 0$ but β becomes so large that a $\alpha\beta$ remains a finite constant.

Although the constitutive equation that mathematically describes the contraction process of smooth muscles by considering all aspects is still unknown, the functionality of mechanical properties of ureter wall is generally represented by three elements model in many studies [45, 46].

Apter and Mason [45, 46] formalized the viscosity properties of muscle simply as the three parameter model of Figure 1.13. The model had two elastic moduli and

one viscosity. The three parameters are necessary to describe stress relaxation curve. The spring represents any energy conserving elements in muscle and the dash pot represents energy dissipating elements. Because muscle will stress-relaxes at all levels of contractile tone, these three components are necessary and sufficient to characterize muscle at one particular level time. However if the tone becomes higher the two elastic moduli will be higher .The tendency to conserve energy is higher because of higher tone and the viscosity coefficient changes because the muscle has contracted.

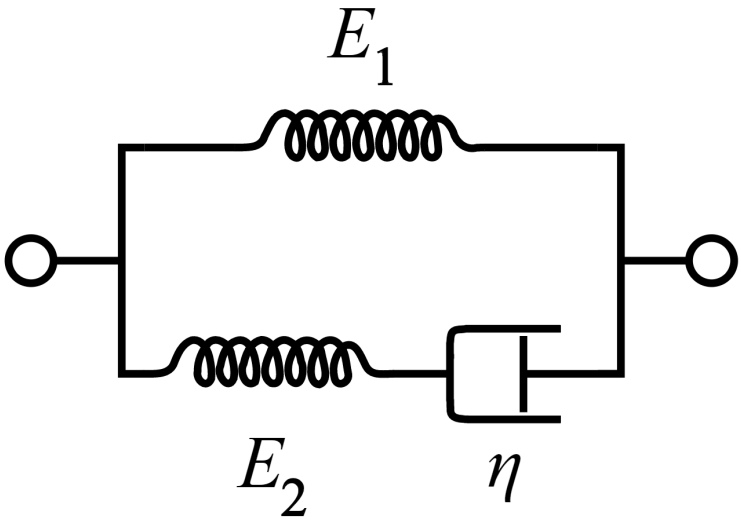

Figure 1.13: Springs E1 and E2 and dashpot η to represent the energy conserving and energy dissipating characteristics of muscle. The arrows indicate there are variables; l0 is upstretched length of the specimen.

According to their model, oscillating muscular contractions reflects oscillating membrane permeability, only if the movement of ions through the membrane is responsible for the changes in the macromolecules levels. The model is depicted as a three parameter Kelvin model, where the two springs represent the energy conserving elements, E_1 and E_2 of muscle and the dashpot represents energy dissipating elements, η. The differential equation of this model and of the muscle is given as Eq. 1.2:

$$\sigma + \frac{\eta}{E_2}\dot{\sigma} = E_{1\epsilon} + (E_1 + E_2)\frac{\eta}{E_2}\dot{\epsilon} \tag{1.2}$$

where σ, $\dot{\sigma}$, ϵ and $\dot{\epsilon}$ are stress, stress rate, strain and strain rate respectively. The elements concerned with conserving and dissipating energy as well as the unstrained length are not constant, but are thought to depend of the levels of muscular macromolecules in a relaxed form (N) and in a contracted form (NA) in the simplest, linear way. Thus with E representing E_1 and E_2 or α or l_0.

$$E = \alpha(A) + \beta(NA) \tag{1.3}$$

Where α and β are both constants. The rate at which the ion N is available to convert A to NA according to the reaction

$$N + A \leftrightarrow NA. \tag{1.4}$$

will depend on the concentration of n the ion N or:

$$\dot{n} = k_2\epsilon - k_3 n \tag{1.5}$$

In the absence of the electrical simulation $\dot{n}$ is the rate change of n. the Eq. 1.5 is the simplest representation of the movement of the ions across a mussel membrane which depolorises on strain.

Apter' work was one fundamental model of viscoelastic ueretral behaviour which made it possible to quantify ureteral wall properties in more detailed fashion than before.Their model however, failed to understand the fact that the oscillating membrane potential is not always associated with contractions. The model also did not consider the All or Nothing principle by which some a threshold level of selected ions,N, can set off sudden conversion of the macromolecules from a relaxed state (a) to a contracted state (NA).

1.7 Modelling of a Typical Ureter

Modelling uretral peristaltic transport and its potential application in the field of medicine has received much attention in recent years. A wide range of analytical studies [47] as well as numerical studies (Computational Fluid Dynamic (CFD) & Finite Element (FE)) [48, 49, 50] have been conducted by different research groups. One of the main goals has been to determine the flow behavior in a tube and determine the mechanism behind any consequent pathological conditions such as reflux or trapping. The ureter's geometry and also the governing differential equation and boundary conditions are among the factors to be considered in ureteral modelling. Parameters such as amplitude ratio, wave number, Reynolds number, pressure difference and flow rate are also necessary to derive a mathematical/numerical model of peristaltic motion.

Shapiro et al. [51] investigated peristaltic flow at small Reynolds numbers and with long waves. The effect of the amplitude ratio, from zero to a full occlusion were studied, for both plane and axisymmetric geometries. Their results showed that the theoretical pressure rise per wavelength decreased linearly with increasing time-mean flow rate. An experiment with a quasi-two-dimensional apparatus confirmed the theoretical values.

Manton [48] investigated the flow behavior from a long peristaltic wave of an arbitrary shape using an asymptotic expansion for low Reynolds number flow. They use the concept of ureteral rate-of-working, which is defined as the energy required to pump fluid through the tube by peristalsis in terms of the motion of the tube wall against the radial force exerted by the fluid on the wall.

The relationship between the mean pressure gradient and volume flux was investigated for the various rate-of-working and shear stress level. They showed that reflux occurred whenever there was an adverse mean pressure gradient, independent of wave shape, and proposed a formula to estimate the amount of reflux based on the magnitude of the adverse pressure gradient.

Zien et al. [49] also studied the mechanisms behind reflux and showed that re-

flux would not occur even in the presence of an adverse mean pressure gradient of a certain magnitude if there was an additional pressure gradient which increased the mean flux volume.

Srivastava et al. [50] carried out further investigations into peristaltic transport of fluid of variable viscosity in a non-uniform tube. They showed that the pressure rise decreased as the fluid viscosity decreased when flow rate was at zero. They also showed that it was independent of viscosity variation at a fixed flow rate, and that it increased if the flow rate was further increased. Also, for a constant pressure the flow rate increased when the viscosity of the fluid decreased.

Takabatake et al.[52, 53] used a finite difference method to study peristaltic flow in a circular cylindrical tube and found greater pumping efficiency for cylindrical tubes than for two dimensional plane channels.

Table 1.2 Lists the work carried out using numerical solutions based on the Navier Stokes equations to model peristalsis motion.

Table 1.2: Summery of analytical studies of peristaltic flow.

References	Fluid type	Reynolds N	Wave shape
Shapiro et al. [51]	Newtonian	0	s
Zien et al. [49]	Newtonian	Small	s
Manton [48]	Newtonian	Small	Arb

Vahidi et al. [54] studied a computational modelling of the ureteral wall. In their study, they used the Arbitray LagrangianEulerian (ALE) method in order to create an interaction between the fluid and structure domains. In their model, a solid wall moving along a rigid tube was used to model the ureteral peristaltic flow and the results showed that when the wave moved downwards, the possibility of backflow decreased. They showed that backflow occurred during the longitudinal propagation. However, in their model the anatomically correct shape of the ureter has not been simulated. It must be noted that the loads causing full closure of the ureteral wall are highly affected by the shape of the cross-section.

Kumar et al. [55] used the finite element method to investigate the influence of the magnitude of the Reynolds number and the wave amplitude and length on the urine flow. Their results indicated that progressive sinusoidal waves with

high amplitude and low wave numbers caused peristaltic flows with high wall shear stress variations and that an applied external magnetic field resulted in a decrease in wall shear stresses.

There have been other studies [51, 53, 56] in which the finite volume method has been used to numerically simulate incompressible fluid in urine transport. Using this approach, Xiao et al. [56] considered a wide range of Reynolds numbers, wave amplitudes and wave lengths in their computational model. Their results were in good agreement with the theoretical work of Shapiro et al. [51] and the numerical results of Takabatake et al. [53]. They showed that for small wave lengths, the inertial force can affect the peristaltic flow more than the amplitude ratio.

They also showed that the velocity profile changed from being parabolic to one with flow separation and a reversed velocity when the Reynolds number increased to 1. Also, with regard to the effect of Reynolds number on the pressure distribution, they suggested that the level of influence of inertial effects on the flow field increased with Reynolds number.

Table 1.3: Summary of computational studies of peristaltic flow.

References	Fluid type	Reynolds N	Geometry	Method
Akabatake et al. [53]	Newtonian	Moderate	Axisym	Finite Difference
Kumar et al. [55]	Newtonian	10-100	2D-plane	Finite Element
Xiao et al. [56]	Newtonian	0.01-100	Axisym	Finite volume
Vahidi et al. [54]	Newtonian	Low	Axisym	Finite Element

Experimental studies on ureter deformation and its features have also been of interest to many researchers and there is a vast literature describing experimental models to mimic the ureteral peristaltic motion. Most of published experimental research describes work carried out using flexible rubber tubes with rubber materials which are a popular way to model the viscoelastic walls of the ureter.

One such experiment is the simulation of physiological ureteral peristalsis using an enlarged model of the ureter with a lobe shaped lumen with silicon properties [57]. They focused on the influence of thickness and luminal position of the catheter on the measured pressure.

An experimental study was also carried out by Jimnez-Lozano [58]. A linear peristaltic pump on a latex rubber tube was contracted locally by an external planar surface designed to simulate the contraction of the ureter. By serial compression of the latex tube, a wave motion was produced. It showed a linear relationship between the wave speed and the flow rate. The study also investigated the effect of passing stones through the ureter to study the transportation of large particles in the tubes and their mean transit time of these particles.

1.8 Aims and Objectives

It is clear that because of the complexity of the physiological phenomena, a comprehensive simulation of every aspect of the urinary system is extremely difficult. In most research a series of basic assumptions are used for simplicity in order to model the ureter and its peristaltic motion. Actual geometrical parameters, biomechanical properties, the origin of contractions and its multi-dimensional movements are important factors which are not considered in the majority of existing works. Modelling these factors may however allow researchers to better describe the mechanisms behind ureteral pathology, leading to more effective diagnosis and treatment. Up to the present, Vahidi's studies [59] are the current state of art in computational modelling of ureter. However, in their model the shape of the ureteral cross section was not anatomically correct and the model for ureteral muscle contraction was also simplified. The aim of the present study is to computationally model the ureteral system in a manner that accurately mimics its dynamic functionality. This model will be able to replicate the peristaltic movement of an actual ureter for a variety of physiological and pathological conditions. The objective of this research will be addressed using our in-house computational fluid dynamic platform, known as $CgLes$, to model the urine flow, coupled with our in-house finite element platform, known as Y code to model the non-linear viscoelastic ureteral wall. One of the advantages of the present study is the use of the Immersed Boundary Method (IBM) to simulate Fluid Structure Interaction (FSI) in Cgles-Y code. It is worth mentioning that the ALE method, used in Vahidi's studies [59] are not recommended for a highly deformable solid due to the high probability of divergence of the solver. Compared with the ALE method, the IBM method is highly robust when solving complex FSI models with irregular boundaries, especially for highly deformable solids such as the ureter during peristaltic movement. A full description of the FSI method will be described in the next chapter.

1.9 Outline of the Thesis

A brief outline of the thesis is presented below.

Chapter 2

Our in-house code will be introduced and the governing equations for both the fluid ($Cgles$) and the solid (Y) parts will be discussed and finally the concept of the Immersed Boundary (IB) in order to couple the two codes will be presented.

Chapter 3

The difference between the linear and non-linear tensile properties of the ureteral wall will be discussed using computational and analytical analysis on a thick walled tube model.

Chapter 4

Firstly the development of an actual anatomical shape of the ureter will be presented, then a variety of approaches to optimise the mesh resolution, given the existing computational resource limitation, will be discussed.

Chapter 5

A computational simulation of the ureter peristaltic contraction will be presented. An intra-abdominal pressure model, as well as two separate contraction models, will be introduced and finally, the results of the pressure over time will be validated against the clinical data.

Chapter 6

A comprehensive study will be conducted on the ureteral peristaltic movement with focus on the urodynamic parameters and urodynamic responses under different pathological conditions.

Chapter 7

The conclusions, limitations and future works will be discussed.

Chapter 2

Methodology

2.1 Motivation

The simulation of a urinary system model which has been studied in this research is a Fluid-Structure Interaction (FSI) problem. Due to the nonlinear nature of such problems, they cannot be solved analytically and experimental analysis is restrained with its inherent limitations. The numerical study of FSI problems, are used in a wide variety of research areas. There are many different methods such as fictitious domain method [60], non-boundary fitting methods [61], Arbitrary Lagrangian Eulerian (ALE) methods [62, 63, 64] to simulate the FSI problems.

Based on the mesh types the FSI methods can be fallen into two main categories [65].

- a) Conforming mesh methods
- b) Non-conforming mesh methods.

In conforming mesh methods, the interface between fluid and solid is considered as a physical boundary whose movement/deformation updates the fluid mesh. It

requires to solve the fluid flow first at a given solid interface. Then the resulting fluid field causes an update to the structure interface based on the prescribed movement or the force from the flow. When the boundary condition for both force and displacement is satisfied at the interface then the solution can be moved to the next time step. Although, these methods are easy to be used with low computational cost, the re-meshing procedure is very time consuming for complex geometries. On the contrary, in the non-conforming mesh methods the location and boundary condition of the solid-fluid interface are treated as constraints imposed on the model equations thus no re-meshing is required [65].

One of the most widely used non-conforming mesh methods is the immersed boundary (IB) method. Peskin [66] introduced and developed the IB method for the first time to simulate blood flow in cardiac systems. The main idea of the method is to use Eulerian and Lagrangian representation for fluid and immersed solid boundary respectively. A singular force is imposed on the fluid from immersed boundary nodes while they are moving at the local fluid velocity. Then using a suitable discrete delta function, as an approximation to the Dirac function, the solid-fluid interaction can be modelled. The method has been used in many applications in a great variety of fields such as heart blood flow [66, 67, 68], flow in collapsible tubes [69], a renal arteriole [70].

In this work, due to complexity of the urinary system, the interaction between the ureteral wall and the urine is modelled by IB method which has been implemented by Ji et al.[71] by combining two pre-existing in-house CFD and FE solver codes. These solvers are called $Cgles$ [72] and Y-code [73] for fluid and solid simulation respectively.

$CgLes$ is a three-dimensional fluid solver with second order accuracy in both time and space. The $Navier$-$Stokes$ equations are solved using the projection method to decouple flow velocities and pressure. They are discretised by a second order $Adam$-$Bashforth$ method in terms of time. Spatial derivatives, diffusion and convection terms are approximated using the second order finite volume method in a rectangular uniform grid.

Y-code is a solid solver using an explicit finite element method for the defor-

mation and movement of a solid. The equation of motion is solved by an explicit time integration scheme based on a central difference method.

In this chapter, a brief introduction of fluid and solid governing equations and the numerical methods used in $Cgles$ and Y-code are presented. Moreover a detailed description of the immersed boundary (IB) method used in current research is explained.

2.2 Fluid Solver ($Cgles$ code)

2.2.1 Governing Equations

In Computational Fluid Dynamics (CFD), the $Navier$-$Stokes$ equations are the most commonly used governing equations describing the balance of mass, momentum and energy in fluid flow. The relationship of the fluid motion and the resulting pressure can be described using a set of partial differential equations. In this study, urine is modelled using an incompressible flow with a low Reynolds number which satisfies the incompressibility assumption.

Since the density (ρ) for an incompressible fluid is constant and consequently ($\frac{\partial \rho}{\partial t} = 0$), the mass continuity equation which is a constraint on the divergence of the flow field can be presented as Eq 2.1:

$$\frac{\partial \rho u_i}{\partial x_i} = 0 \tag{2.1}$$

Where u is the velocity and the subscript i is the $Einstein's$ notation, ranging from 1 to 3 to represent different direction and velocity components.

In the $Navier$-$Stokes$ equations, the momentum equations are obtained by balancing the convective acceleration, internal stresses and external forces for each control volume using $Newtons$ second law. The momentum equation (Eq:2.2) considering the mass continuity constraint (Eq:2.1) is presented in its differential

form:

$$\frac{\partial \rho u_i}{\partial t} + \frac{\partial \rho u_i u_j}{\partial x_j} = -\frac{\partial p}{\partial x_i} + \mu[\frac{\partial \tau_{ij}}{\partial x_j}] + f_i \tag{2.2}$$

where p is the pressure, f_i is the body force, τ_{ij} is the component of the viscous stress tensor and μ is the dynamic viscosity which is constant. In incompressible flow, a constant kinematic viscosity can be defined in Eq 2.3:

$$\nu = \frac{\mu}{\rho} \tag{2.3}$$

In this study, the temperature of urine is considered constant and therefore no energy equation is solved. Due to the incompressibility and assumption of constant dynamic viscosity of the urine (not being a function of temperature), the energy equation is decoupled from the continuity and momentum equations.

2.2.2 Finite Volume Method

The three commonly used methods to numerically solve the *Navier-Stokes* equations are Finite Difference, Finite Volume (FV), Finite Element (FE) methods. With the finite difference method, each partial derivative in the governing equations is expressed by an equivalent finite difference approximation. It implies that the variable values (e.g velocity and pressure) from neighboring nodes are used to approximate the desired variables at certain node. Eq 2.4 describes an approximation of the partial derivative Eq 2.1 for a one-dimensional problem.

$$\frac{\partial u_i}{\partial x_i} = \lim_{\Delta x_i \to 0} \frac{u_{x_i + \Delta x_i} - u_{x_i}}{\Delta x_i} \tag{2.4}$$

In the FV method, the computational domain is divided into a number of control volumes where the variable is positioned at the centre of each control volume. Then the differential forms of the governing equations are integrated

over each control volume. By application of the divergence theorem for derivative terms, the volume integral can be converted into surface integrals at each volume cell face to calculate the flux change over the whole control volume. A description of the discretization will be presented further in the next sections.

In *Cgles*, the *Navier-Stokes* equations are discretised on a fixed staggered Cartesian grid by the finite volume approach. In the finite volume method, volume integrals in a partial differential equation that includes a divergence term are transformed to surface integrals by applying the divergence theorem. These terms are then assessed as fluxes at the surfaces of each finite volume. These methods are described as conservative because the flux entering a given volume through a surface is identical to that leaving the adjacent volume. The method is used in many computational fluid dynamics packages.

The integral form of the simplified incompressible continuity equation can be written in the form of Eq 2.5:

$$\int_v \frac{\partial u_i}{\partial x_i} dv = 0 \tag{2.5}$$

Eq 2.5 indicates the net flux change of Control Volume (CV) is zero which constrains the sum of the flux through each boundary face, as given in Eq 2.6.

$$\int_s u_i.(n_i ds) = 0 \tag{2.6}$$

where n is the normal vector to the face (s) of the control volume. Similarly the momentum equation can be described as:

$$\int_v \frac{\partial u_i}{\partial t} dv + \int_v \frac{\partial u_i \partial u_j}{\partial x_j} dv = -\int_v \frac{1}{\rho} \frac{\partial u_i \partial u_j}{\partial x_j} dv + \int_v \frac{\partial \tau_{ij}}{\partial x_j} dv + \int_v \frac{f_i}{\rho} dv \tag{2.7}$$

$$\frac{\partial u_i}{\partial t}\Delta V + \int_s u_i u_j n ds = -\frac{1}{\rho}\frac{\partial P}{\partial x_i}\Delta V + \int_s \tau_{ij} n ds + \frac{\overline{f_i}}{\rho}\Delta v \tag{2.8}$$

2.2.3 Mesh Construction and Indexing

The computational domain is divided into a finite number of discrete points at which the governing equations can be solved. A structured mesh is used in this model and its connectivity to the grid points can be expressed by a two or three dimensional array. Figure 2.1 shows that the uniformly-distributed rectangular mesh used in the simulation of the flow domain in this work can be easily represented by a 2D array of 64×64.

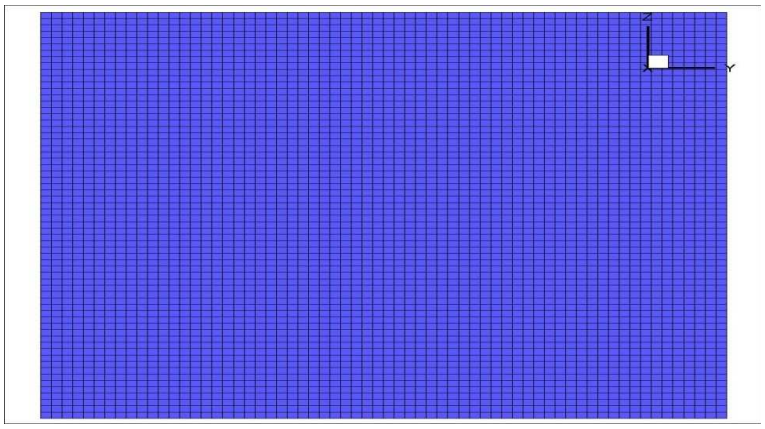

Figure 2.1: The structured grid used in current simulation.

The advantage of this mesh is that it's generation is easy and it requires less storage compared with other types of mesh. This grid setting also takes full advantage of the IB method as the calculation is carried out on the whole computational domain and only requires the coordinates of the IB points to determine the grid cell it lies in and make further corrections. Figure 2.2 shows the Cartesian grids used by the IB method.

In $Cgles$ code, the staggered grid variable arrangement is used. In the staggered mesh, each variable is stored in its own sub grid shifted half a cell in one or more directions relative to the other grids. Each pressure node is in the center

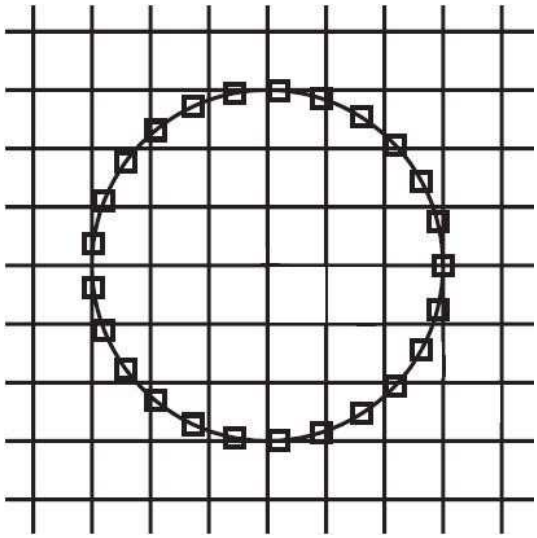

Figure 2.2: The Cartesian grids used by IB method.

of each cell and flow is described as flow though orthogonally adjacent cell walls, as shown in Figure 2.3. The advantage of the staggered grid is to reduce any oscillations in pressure due to calculation of the pressure at cell centers. On staggered grids, the pressure gradient at the cell face is described by Eq 2.9 where $P(x+\frac{\Delta x}{2}, y+\frac{\Delta y}{2}, z+\frac{\Delta z}{2})$ is the pressure at the node located at the centre of the control volume and $\Delta x, \Delta y, \Delta z$ are the grid spacings in the three spatial dimensions.

$$\frac{\partial}{\partial x}P[x, y+\frac{\Delta y}{2}, z+\frac{\Delta z}{2}] = \frac{P[x+\frac{\Delta x}{2}, y+\frac{\Delta y}{2}, z+\frac{\Delta z}{2}] - P[x-\frac{\Delta x}{2}, y+\frac{\Delta y}{2}, z+\frac{\Delta z}{2}]}{\Delta x} \tag{2.9}$$

The gradient of the pressure in each direction in Eq 2.9 corresponds with the location of u, v, w velocity and thus can couple pressure perfectly with velocity [74].

Indices are assigned to the nodes instead of their coordinates. All the grid points are identified by indices i, describing x position, j, describing y position, and k, describing z position. In $Cgles$, each index variable has an associated

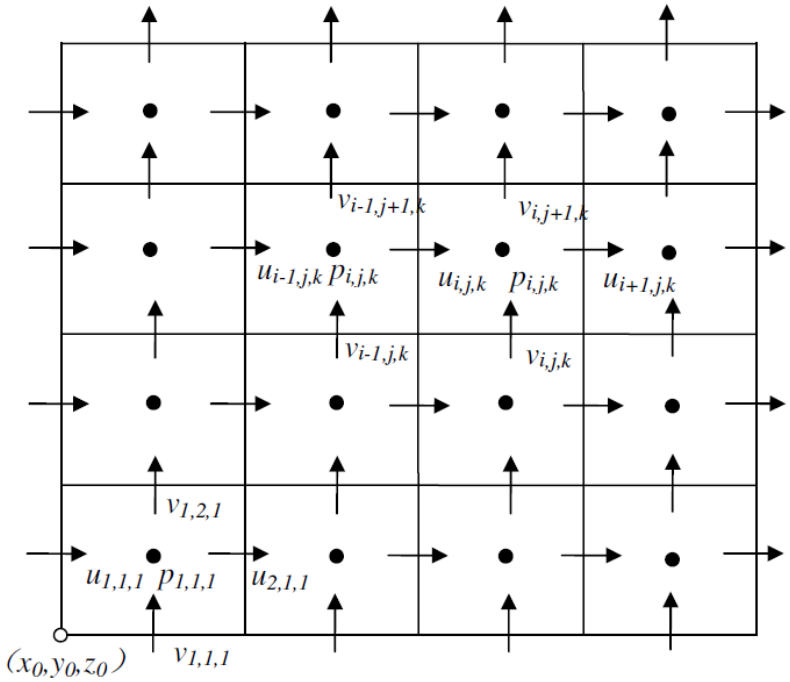

Figure 2.3: Fluid variable in the staggered grids.

control volume and its location can be calculated using the indices i, j and k as shown below in Eqs(2.10, 2.11, 2.12).

$$u_{i,j,k} = u(x_0 + i.\Delta x, y_0 + (j + \frac{1}{2}).\Delta y, z_0 + (k + \frac{1}{2}).\Delta z) \tag{2.10}$$

$$v_{i,j,k} = v(x_0 + (i + \frac{1}{2}).\Delta x, y_0 + j.\Delta y, z_0 + (k + \frac{1}{2}).\Delta z) \tag{2.11}$$

$$w_{i,j,k} = w(x_0 + (i + \frac{1}{2}).\Delta x, y_0 + (j + \frac{1}{2}).\Delta y, z_0 + (k.\Delta z) \tag{2.12}$$

$$P_{i,j,k} = P(x_0 + (i + \frac{1}{2}).\Delta x, y_0 + (j + \frac{1}{2}).\Delta y, z_0 + (k + \frac{1}{2}).\Delta z) \tag{2.13}$$

Where (x_0,y_0,z_0) is the location of the left bottom corner vertex of the first grid cell as shown in Figure 2.3.

2.2.4 Discretization in *Cgles* Code

The *FV* governing equations derived above can be discretized in space by means of a uniform Cartesian grid. For a 2D control volume of mass, shown in Figure 2.4, dx and dy represent the length of the edge in each direction. Thus, the continuity equation can be give as Eq 2.14.

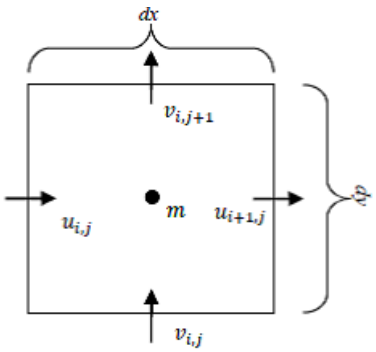

Figure 2.4: 2D control volume of mass.

$$\int_s u_i(n_i ds) = u_{i+1,j}dy - u_{i,j}dy + v_{i,j+1}dx - v_{i,j}dx = 0 \tag{2.14}$$

The continuity equation over a mass control volume for a 3D case, with indices of i, j, k can be expressed as:

$$\int_s u_i(n_i ds) = (u_{i+1,j,k}-u_{i,j,k})dydz+(v_{i,j+1,k}-v_{i,j,k})dxdz+(w_{i,j,k+1}-w_{i,j,k})dxdy = 0 \tag{2.15}$$

For the momentum equation (Eq 2.15), for $i = 1, 2, 3$ respectively, each of the terms in that equation characterize for an integrated value over a similar u-

control volume. For space discretization, the control volume was chosen for $u_{i,j,k}$, where i, j, k is the index showing the location of each variable on the staggered grid and $u_{i,j,k}$, $v_{i,j,k}$, $w_{i,j,k}$ represent the velocity in three directions respectively.

2.2.4.1 Convective Term

From Eq 2.15, the convective acceleration over a velocity control volume can be defined as:

$$\int_v \frac{\partial(u_i u_j)}{\partial x_j}.dV = \int_s (u_i u_j) n_i ds \tag{2.16}$$

On a 3D rectangular *Cartesian* grid, the convective acceleration over the u-control volume for $u_{i,j,k}$ can be discretised in space using the averaged values on each cell face of the control volume as presented in Eq 2.17:

$$\begin{aligned}\int_s (u_i u_j) n_i ds = \int uudydz + \int uvdxdz + \int uwdxdy = \\ (u_{i+\frac{1}{2},j,k} u_{i+\frac{1}{2},j,k} - u_{i-\frac{1}{2},j,k} u_{i-\frac{1}{2},j,k})dydz + \\ (u_{i,j+\frac{1}{2},k} v_{i-\frac{1}{2},j+1,k} - u_{i,j-\frac{1}{2},k} v_{i-\frac{1}{2},j,k})dzdx + \\ (u_{i,j,k+\frac{1}{2}} w_{i-\frac{1}{2},j,k+1} - u_{i,j,k-\frac{1}{2}} v_{i-\frac{1}{2},j,k})dydx\end{aligned} \tag{2.17}$$

The velocities on the cell face can be approximated using the averaged value from neighbouring velocity grids as presented in Eq 2.18:

$$u_{i-\frac{1}{2},j,k} = 0.5 \times (u_{i-1,j,k} + u_{i,j,k}) \tag{2.18}$$

2.2.4.2 Pressure and Viscous Stress Terms

For each velocity control volume on a staggered grid, the pressure nodes are on the cell faces and the pressure gradient at the cell centres can be directly obtained using the face value. Then, the integrated pressure term over the whole u-control volume can be written as Eq 2.19:

$$-\int_v \frac{1}{\rho} p n_i ds = -\frac{1}{\rho}\frac{P_{i,j,k} - P_{i-1,j,k}}{dx} dxdydz \tag{2.19}$$

The deformation rate is expressed as Eq 2.20:

$$e_{ij} = \overline{e_{ij}} + \overline{\overline{e_{ij}}} = \frac{1}{2}[\frac{\partial u_i}{\partial x_j} + \frac{\partial u_j}{\partial x_i} - \frac{2}{3} \bigtriangledown .u_j \delta_{ij}] + \frac{1}{3}\frac{\partial u_r}{\partial x_r}\delta_{ij} \tag{2.20}$$

Where $\overline{e_{ij}}$ is the volume constant deformation rate and $\overline{\overline{e_{ij}}}$ is the uniform rate of expansion. δ_{ij} is the $Kronecker$'s $delta$.

For an isotropic fluid the viscous stress tensor is a linear function of $\overline{e_{ij}}$ and $\overline{\overline{e_{ij}}}$ as shown in Eq 2.21

$$\tau_{ij} = \lambda\overline{\overline{e_{ij}}} + 2\mu\overline{e_{ij}} \tag{2.21}$$

Whereas for a Newtonian fluid, λ is second viscosity which is often considered zero, μ is dynamic viscosity which is assumed to be constant for the current study.

The viscous stress tensor can thus be expressed as:

$$\tau_{ij} = 2\mu\overline{e_{ij}} = \mu[\frac{\partial u_i}{\partial x_j} + \frac{\partial u_j}{\partial x_i} - \frac{2}{3} \bigtriangledown .u_j \delta_{ij}] \tag{2.22}$$

From the continuity equation, Eq 2.22 reduces to Eq 2.23:

$$\tau_{ij} = \mu[\frac{\partial u_i}{\partial x_j} + \frac{\partial u_j}{\partial x_i}] \tag{2.23}$$

The stress acting on the surface of each control volume depends on the surface orientation and can be expressed as a product of the stress tensor $\overline{\tau}$ and the surface normal vector $\overrightarrow{n}$ as shown in Eq 2.24.

$$\int \bigtriangledown \tau.dV = \int_s \tau_{ij} n_i ds = \int_s \mu[\frac{\partial u_i}{\partial x_j} + \frac{\partial u_j}{\partial x_i}] n_i ds \tag{2.24}$$

For instance in a 3D u-control volume, the integrated viscous stress term can be expanded, as presented in Eq 2.25:

$$\int_s \mu[\frac{\partial u_i}{\partial x_j}+\frac{\partial u_j}{\partial x_i}] n_i ds = \int \mu[\frac{\partial u}{\partial x}+\frac{\partial u}{\partial x}]dydz + \int \mu[\frac{\partial u}{\partial y}+\frac{\partial v}{\partial x}]dxdz + \int \mu[\frac{\partial u}{\partial z}+\frac{\partial w}{\partial x}]dxdy \tag{2.25}$$

In Eq 2.25 the terms $\frac{\partial u}{\partial x}, \frac{\partial u}{\partial y}, \frac{\partial u}{\partial z}$ describe the velocity gradients at the centres of the faces of the control volume cell, so the discretization can be written as:

$$\int \mu[\frac{\partial u}{\partial x} + \frac{\partial u}{\partial x}]dydz = 2 \times \mu(\frac{u_{i+1,j,k} - u_{i,j,k}}{dx} - \frac{u_{i,j,k} - u_{i-1,j,k}}{dx})dydz \tag{2.26}$$

$$\int \mu[\frac{\partial u}{\partial y} + \frac{\partial v}{\partial x}]dxdz = \mu(\frac{u_{i,j+1,k} - u_{i,j,k}}{dy} + \frac{v_{i,j+1,k} - v_{i-1,j+1,k}}{dx}) - (\frac{u_{i,j,k} - u_{i,j-1,k}}{dy} + \frac{v_{i,j,k} - v_{i-1,j,k}}{dx})dxdz \tag{2.27}$$

$$\int \mu[\frac{\partial u}{\partial z} + \frac{\partial w}{\partial x}]dxdy = \mu(\frac{u_{i,j,k+1} - u_{i,j,k}}{dz} + \frac{w_{i,j,k+1} - w_{i-1,j,k+1}}{dx}) - (\frac{u_{i,j,k} - u_{i,j,k-1}}{dz} - \frac{w_{i,j,k} - w_{i-1,j,k}}{dx})dxdy \quad (2.28)$$

2.2.4.3 Other Forces

External forces (f_i) include gravity, electromagnetic force, and centrifugal force. In a numerical simulation, this kind of force is usually stored at the centre of the continuity control volume the same as the pressure.

2.2.5 Boundary Conditions

2.2.5.1 Inlet and Outlet

The correct boundary conditions must be specified at each time step to correctly solve the momentum and continuity equations. In this work, the pressure inlet and outflow are used to define the inlet and outlet boundary conditions. The urine flow is simulated such that it is driven by the pressure difference. To do so, fixed pressure values are defined at the inlet and outlet and zero gradient velocity boundary condition is applied on both the inlet and outlet.

- Inlet boundary condition:

  $p = p_{inlet}$

  $\frac{\partial u}{\partial n} = 0$, $\frac{\partial v}{\partial n} = 0$, $\frac{\partial w}{\partial n} = 0$, n is the normal vector to the boundary

- Outlet boundary condition:

  $p = p_{outlet}$

$\frac{\partial u}{\partial n} = 0,\ \frac{\partial v}{\partial n} = 0,\ \frac{\partial w}{\partial n} = 0$

2.2.5.2 Wall Boundary Conditions

There are two types of boundary conditions used to define a solid wall: free-slip and no-slip boundary conditions. A no-slip boundary is when the velocity of the fluid set to zero at the wall and there is no flow across the boundary. For the free slip boundary, the gradient of velocity parallel to the wall is set to zero in order to have a stress free condition on the wall. In this work, a free slip boundary condition is used for the outer boundary and a no slip boundary condition on the boundary between the fluid and solid.

2.2.6 Non dimensionalization of Governing Equations

In *Cgles* code the non-dimensional governing equations are implemented. In order to obtain non-dimensional governing equation, the following substitutions are made in Eq 2.29 using reference velocity u_{ref} and reference length L_{ref}.

$$\begin{aligned} u_x &= u_x^* u_{ref} \\ p &= p^* u_{ref}^2 \rho \\ t &= t^* t_{ref} = t^* L_{ref}/u_{ref} \\ x &= x^* L_{ref} \\ f_x &= f_x^* \rho u_{ref}^2 / L_{ref} \end{aligned} \tag{2.29}$$

Where the variables with superscript star are the dimensionless quantities. By implementing the above substitution in the momentum equations, the following equation (Eq 2.30) can be obtained.

$$\frac{\partial u_x^*}{\partial t^*} + u_x^* \frac{\partial u_x^*}{\partial x^*} + u_y^* \frac{\partial u_x^*}{\partial y^*} + u_z^* \frac{\partial u_x^*}{\partial z^*} = \frac{\partial p^*}{\partial x^*} + \frac{\nu}{u_{ref} L_{ref}} [\frac{\partial^2 u_x^*}{\partial x^{*2}} + \frac{\partial^2 u_x^*}{\partial y^{*2}} + \frac{\partial^2 u_x^*}{\partial z^{*2}}] + f_x^* \tag{2.30}$$

The dimensionless Reynolds number is also expressed as: $Re = \frac{\rho u_{ref} L_{ref}}{\mu} = \frac{u_{ref} L_{ref}}{\nu}$

2.2.7 Incompressible Projection Method (IPM)

The projection method was originally introduced by Chorin [75] and Temam [76]. For an incompressible Newtonian fluid, the momentum equations can be written as follows in which an explicit time marching scheme is used for illustration:

$$\frac{u^{n+1} - u^n}{\Delta t} + u^n . \bigtriangledown u^n = - \bigtriangledown p^{n+1} + \bigtriangledown(\nu(\bigtriangledown u^n) + (\bigtriangledown u^n)^T)) + f^n \tag{2.31}$$

$$(\frac{\partial u}{\partial t})^n = \frac{u^{n+1} - u^n}{\Delta t} \tag{2.32}$$

where n and $n+1$ refer to the time step level.

The projection method is based on the two stage fractional scheme, which means several calculations steps are performed in each time step to approach the final result. In the first stage a predictor step for the intermediate velocity u^* is

computed by ignoring the pressure term, as presented in Eq 2.33.

$$\frac{u^* - u^n}{\Delta t} + u^n . \bigtriangledown u^n = \bigtriangledown(\nu(\bigtriangledown u^n) + (\bigtriangledown u^n)^T)) + f^n \tag{2.33}$$

Since all the terms are known at time step n, the Eq 2.33 can be solved and the value of u^* is obtained. Then, in the corrector step, the velocity u^{n+1} is obtained by using Eq 2.34 in which p^n firstly needs to be solved.

$$u^{n+1} = - \bigtriangledown p^n . \Delta t + u^* \tag{2.34}$$

In order to find p^n, the *Poisson* equation can be derived by subtracting the momentum equations with regards to u^* and u^{n+1} and taking the divergence of both sides:

$$\frac{1}{\Delta t}\frac{\partial {u_i}^{n+1}}{\partial x_i} + \frac{\partial {u_i}^*}{\partial x_i} + \frac{1}{\rho}\frac{\partial^2 p^{n+1}}{\partial {x_i}^2} = 0 \tag{2.35}$$

By applying $\bigtriangledown . u^{n+1} = 0$, the following equation is obtained.

$$\bigtriangledown^2 p^n = \frac{\bigtriangledown . u^*}{\Delta t} \tag{2.36}$$

2.2.7.1 Time Stepping Schemes

When the final velocity is obtained for a given time step, the scheme marches/steps to the next time step and the whole projection-correction process is restarted until the desired wall time criteria have been met. In the $Cgles$ code, the 2nd order $Adams\text{-}Bashforth$ time stepping scheme is used because this method is known to provide higher accuracy than other methods.

By applying $Adams\text{-}Bashforth$, the momentum equation in Eq 2.31 can be

discretized in time as shown in Eq 2.37,

$$u^{n+1} = u^n + dt(\frac{3}{2}RHS^n - \frac{1}{2}RHS^{n-1} - \frac{3}{2} \bigtriangledown p^n + \frac{1}{2} \bigtriangledown p^{n-1}) \tag{2.37}$$

where the Right Hand Side (RHS) stands for the convective and viscous term and can be expanded as in Eq 2.38:

$$RHS = (\nu \bigtriangledown^2 u^n + (\bigtriangledown u^n)^T) f^n \tag{2.38}$$

and the intermediate velocity can be obtained by Eq 2.39:

$$u^* = u^n + dt(\frac{3}{2}RHS^n - \frac{1}{2}RHS^{n-1} + \frac{1}{2} \bigtriangledown p^{n-1}) \tag{2.39}$$

Then the *Poisson* equation can be drived as Eq 2.40 :

$$\bigtriangledown^2 p^n = \frac{2 \bigtriangledown .u^*}{3dt} \tag{2.40}$$

The correction step can be written as Eq 2.41:

$$u^{n+1} = u^* - \frac{3}{2} dt \bigtriangledown p^n \tag{2.41}$$

2.3 Solid Solver (Y-code)

To simulate the deformation of a solid structure the combined Finite-Discrete Element Method ($FDEM$), which was originally described by Munjiza [73], is used in Y-code.The $FDEM$ merges the finite element-based analysis of continua with the discrete element-based transient dynamics, contact detection and contact interaction solutions. It is beyond the scope of this thesis to provide a comprehensive explanation for the combined $FDEM$. However, a very brief

description of the method will be given in the following section.

2.3.1 Introduction to Finite District Element method (FDEM):

The microstructure of engineering materials is discontinuous; however, in many engineering problems the discontinuous nature of the material is neglected. This is because engineering problems generally use materials in quantities sufficiently large that the microstructure of the material can be described by averaged material properties, which are continuous. The averaged material properties are given as continuous functions of volume. These physical properties allow the definition of constitutive equations such as conservation of mass or conservation of energy. Governing equations are usually given as a set of partial differential equations or integral equations. The governing equations can be coupled with external actions in the form of boundary and initial conditions such as loads, supports or initial velocity. Hypothesis of discontinua describe the interactions between particles and balance equations. Because these equations cannot be solved analytically, and approximate numerical solutions are sought instead. The most advanced numerical methods are Discontinuous Deformation Analysis (DDA) and Discrete Element Methods (DEM). These methods are designed to handle contact situations for a large number of irregular particles. DDA is more suitable for static problems, while DEM is more suitable for problems involving transient dynamics until a state of rest or steady state is achieved. To model deformation under stress or load, the state of the art method is the Finite Element Method (FEM). To model discontinuum-based phenomena (interaction and motion of individual particles), the state of the art method is the District Element Method (DEM). The new method is therefore a combination of both FEM and DEM and is denoted the combined finitediscrete element method ($FDEM$). In the combined $FDEM$, each particle (body) is characterized by a single discrete element that interacts with discrete elements that are close to it. Moreover, each discrete element is discretized into finite elements. Each finite element mesh describes the deformability of a single discrete element (particle, body). So far the combined

FDEM has been applied to a wide range of engineering problems such as rock mechanics, soil mechanics, mining, powders, composites, bone mechanics and biological tissues. Figure 2.5, shows an FDEM problem comprising two discrete elements. Each discrete element is discretized into finite elements.

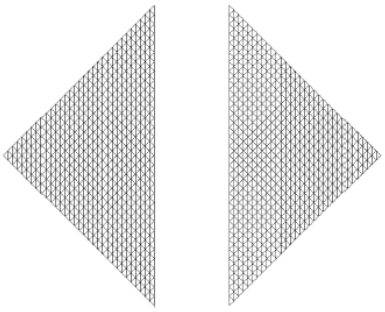

Figure 2.5: The combined finite-discrete element problem comprising two discrete elementsin the combined finite-discrete element method, each discrete element is discretised into finite elements

2.3.2 Stress and Strain Relationship

In this study, the ureter structure is meshed with tetrahedral elements, one of which is shown in Figure 2.6.

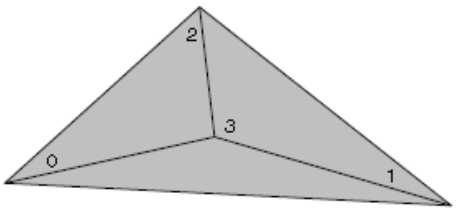

Figure 2.6: A solid tetrahedron finite element

The deformability of the elements is controlled by nodal forces and the corre-

sponding displacement. The deformation of the solid can be written as Eq 2.42

$$f(p) = p + u(p) \tag{2.42}$$

Where p is a set of positions, f is a smooth function mapping the initial positions to the deformed positions and $u(p)$ is a set of displacement vectors. Eq 2.43 and 2.44 illustrate the deformation gradient and deformation gradient tensor of each material position.

$$F(p) = \bigtriangledown f(p) = I + \bigtriangledown u \tag{2.43}$$

$$F = \bigtriangledown f = \bigtriangledown \begin{bmatrix} x + u(x,y,z) \\ y + v(x,y,z) \\ z + w(x,y,z) \end{bmatrix} = \begin{bmatrix} 1 + \frac{\partial u}{\partial x} & \frac{\partial u}{\partial y} & \frac{\partial u}{\partial z} \\ \frac{\partial u}{\partial x} & 1 + \frac{\partial v}{\partial y} & \frac{\partial v}{\partial z} \\ \frac{\partial w}{\partial x} & \frac{\partial w}{\partial y} & 1 + \frac{\partial w}{\partial z} \end{bmatrix} \tag{2.44}$$

From the strain tensors, the $Cauchy$ stress is calculated using the constitutive law. Different constitutive laws can be employed at this point. In Y-code, a constitutive law for homogeneous isotropic material derived by analogy with the Hooke's constitutive law. Eq 2.45 represents the modified Hooke's constitutive law.

$$T = \frac{E}{(1+\nu)} \frac{1}{(|detF|)^{2/3}} E_d + \frac{E}{(1+2\nu)} \frac{1}{(|detF|)^{2/3}} E_s + \frac{2\bar{\mu}}{(|detF|)^{2/3}} D \tag{2.45}$$

where $E_d = \frac{1}{2}[\frac{FF^T}{(|detF|)^{2/3}} - I]$ is the $GreenSt.\ Venant$ strain tensor caused by the deformation, $E_s = I[\frac{(|detF|)^{2/3}-1}{2}]$ is the $GreenSt.\ Venant$ strain tensor due to volume changing stretch and $[\frac{2\bar{\mu}}{(|detF|)^{2/3}}]$ represents the viscous stress which is responsible for material damping. D is the rate of deformation obtained from velocity gradient. E is the Young's modulus, ν is $Poissons$ ratio, $\bar{\mu}$ is damping

due to deformation.

Based on the integrated modified Hooke's constitutive law in Eq 2.45, the viscoelastic materials can undergo strain and volume change without being damaged. The nonlinear tensile property of the ureteral wall was extracted from the clinical data [43] and integrated directly in Eq 2.45, using the equivalent strain. A comprehensive description of this methodology was explained in chapter 3.

The *Cauchy* stress is applied to a deformed tetrahedral element (Figure 2.6) used in ureter simulation and the traction force, S, for over each of the surface of the tetrahedron is calculated by using the normal on the edge of the deformed tetrahedron. Surface traction for each of the four surfaces is distributed equally to each node and an equal force is allocated to each node.

$$f = \frac{1}{3}S \tag{2.46}$$

The Y-code solver uses an explicit finite element method for dynamic simulations, the deformation and movement of a solid. This can be solved by an implementation of *Newtons* second law:

$$F = M.a = M.\ddot{X} \tag{2.47}$$

where F is the total force acting on each node, which include the internal forces due to *Cauchy* stress or the interaction force between the wall and the fluid force acting on the surface nodes. M is the mass represented by the node, a is the acceleration to be determined, X is a set giving the node coordinates in three dimensions which will be updated at each time step.

The FE method explicit scheme based on a central difference method [73] can be summarized as follow:

- Calculation of internal forces based on the deformation of particles.
- Contact detection, for instance by using the Munjiza-NBS contact detection

algorithm.

- Calculation of forces resulting from contact interaction using a penalty function method.
- Summing external forces and solution of the equation of motion for each element separately.

The equation of motion is stable for a given time step dt because:

$$dt < \frac{dx}{\sqrt{\frac{\lambda+\frac{2G}{3}}{\rho}}} \tag{2.48}$$

Where dx is the smallest element size, λ is Lam's first parameter, G is the shear modulus and ρ is the density.

2.4 Coupling Between Fluid and Solid Codes (Immersed Boundary (IB))

Fluid-solid interactions need to be determined by solving the equations of motion of the fluid in conjunction with the governing equations for the elastic body. The equations governing the fluid flow are solved for the whole computational domain on a Cartesian grid; the effect of the immersed solid boundary is then imposed on the flow through a body force term in the $Navier$-$Stokes$ equations.

The force on the interface boundary is calculated by the governing equations of the solid and extrapolated onto the nearby fluid grids with an extrapolation function and is then used to calculate a new fluid velocity. The new velocity field is then interpolated again onto the interface where a non-slip boundary condition applies to give a velocity of the virtual surface by which the new surface location can be updated accordingly. In the next time step the body force on the interface can be calculated again by Hooke's Law and then extrapolated to the nearby fluid domain.

The fluid motion equations are discretized on a fixed $Cartesian$ grid. The conservative form of the second order $Adam\text{-}bashforth$ temporal discretised governing equations of incompressible fluid using the IB method point is presented in Eq 2.49:

$$u^{n+1} = u^n + dt[\frac{3}{2}RHS^n - \frac{1}{2}RHS^{n-1} - \frac{3}{2} \bigtriangledown p^n + \frac{1}{2} \bigtriangledown p^{n-1}] + f^{n+\frac{1}{2}}dt \quad (2.49)$$

An extra singular body force, f, is added into the momentum equation to take the solid boundary into account.

There are also two new functions: $I(\theta)$ is interpolation of the solid mesh on to the CFD grid points and $D(\Theta)$ is the distribution function on the immersed boundary points. The θ represents the fluid variables on the grids, such as the velocity vector (u), pressure (p), body force (f), and the Θ denotes the variables on the IB points, such as the interpolated velocity U, and f_i. The interpolation function projects the physical fluid field from the grids to the IB points and the distribution function maps the calculated results from the IB points back to the $Cartesian$ grids.

In Eq 2.50 and Eq 2.51, U^{n+1} is the interpolated velocity on the IB points and the V^{n+1} is the desired velocity on the IB points.

$$U^{n+1} = V^{n+1} \quad (2.50)$$

where

$$U^{n+1} = I(u^{n+1}) \quad (2.51)$$

By substituting Eq 2.51, Eq 2.49 into Eq 2.50 and rearrange the equations, the

body force on the grid points is obtained as presented in Eq 2.52:

$$F(t) = \begin{cases} D[V^{n+1} - I[u^n + dt[\frac{3}{2}RHS^n - \frac{1}{2}RHS^{n-1} - \frac{3}{2} \bigtriangledown p^n + \frac{1}{2} \bigtriangledown p^{n-1}]]], & Inside\, IB \\ 0, & Outside\, IB \end{cases} \tag{2.52}$$

When distributing the body force from the IB points to the grids, either a Full Distribution (FD) forcing strategy or a Half Distribution (HD) forcing strategy can be used depending upon the model simulation.

In FD forcing strategy, using a delta function the body force f acting on an IB point is spread over several grids both inside and outside the immersed boundary. It has been reported that the convergence rate is in this method is fast due to smooth body force transferring. In contrary to HD method which is proposed for high Reynolds number simulation flows [77], the FD method is widely used for low Reynolds applications. More detail about the schemes and the applications can be found in the paper by Ji et al. [71]. Due to the low speed of the urine flow, the main forcing strategy used in this work is FD forcing strategy.

The iterative IB method involves a two-step predictor-corrector procedure similar to the projection method in which body force and the pressure are solved iteratively. The first step is the prediction step in which the intermediate velocity u^* is predicted by using Eq 2.53

$$u^* = u^n + dt[\frac{3}{2}RHS^n - \frac{1}{2}RHS^{n-1} + \frac{1}{2} \bigtriangledown p^{n-1}] \tag{2.53}$$

Then, the intermediate pressure $p^{n,k}$and the body force $f^{\frac{n+1}{2},k}$ iteratively, using the procedure outlined in the following pseudo code, where k is the iteration step.

Let $p^{n,k}$=p^{n-1}, and k=1.

Outer loop begins:

- Update body force $f^{\frac{n+1}{2},k}$

  Substitute u^* into Eq 2.52,

$$f^{(\frac{n+1}{2},k)}dt = D(V^{n+1} - I([u^* - \frac{3}{2}dt \bigtriangledown p^{n,k-1}]) \tag{2.54}$$

$$f^{n+\frac{1}{2},k} = \begin{cases} D[V^{n+1} - I[u^* - \frac{3}{2}dt \bigtriangledown p^{n,k-1}]], & Grids\ Inside\ IB \\ 0, & Grids\ Outside\ IB \end{cases} \tag{2.55}$$

- Update the intermediate velocity u^{-k}

$$\bar{u}^k = u^* + f^{(n+\frac{1}{2},k)}dt \tag{2.56}$$

- Update pressure intermediate $p^{n,k}$

$$\bigtriangledown^2 p^{n,k} = \frac{2 \bigtriangledown .\bar{u}^k}{3dt} \tag{2.57}$$

- Apply convergence criteria

  If the norm of $I[u^* - \frac{3\delta t}{2}\frac{\partial p^{n,k}}{\partial x}]$-$I[u^* - \frac{3\delta t}{2}\frac{\partial p^{n,k-1}}{\partial x}]$ is smaller than a given tolerance, break the loop.

- Let k=k+1

- Outer loop ends

  The next step after the iterative process is completed is the correction step. The correction step is applied with $p^n = p^{(n,k)}$ and the final velocity is as follows:

$$u^{n+1} = \bar{u}^k - \frac{3}{2}dt\bigtriangledown^n \tag{2.58}$$

It is worth noting that the pressure Poisson equation (Eq 2.57) is solved using the iterative $Bi-Conjugate\,Gradient$ $(BiCG)$ method and the pressure from one

iteration is used regardless of convergence. It is just an intermediate pressure and there is no need the exact value at this intermediate stage. Also in this iterative IB method, the coefficient matrix for pressure never changes which means it is independent.

To verify this iterative IB method, a series of numerical simulations were carried out and can be found in the paper of Ji et al. [71]. They include a simulation of turbulent flow with moderate Reynolds number (Re+ =1000), turbulent flow past a 3D static cylinder, laminar flow past a two-dimensional stationary cylinder, laminar flow past a two-dimensional stationary elliptic cylinder and laminar flow past a stationary sphere.

2.5 Summary

The in-house code (Coupled $Cgles$-Y) was introduced. The $Cgles$ is a three-dimensional fluid solver using the $NavierStokes$ equations. The discretization of different $Navier$-$Stokes$ equation terms in the control volume method is explained. Then, the projection method and boundary conditions used in $Cgles$ code to solve the fluid domain were described. The simulation of the ureteral wall deformation was conducted using the in-house the Y-code. The stress and strain relationship of the finite element method in the solid domain was explained and the corresponding governing equations were introduced. Finally, to simulate the interaction between the fluid and solid domains, an existing novel Immersed Boundary method was introduced to simulate moving boundaries.

Chapter 3

Deformation of a Thick Walled tube under Confining Pressure

3.1 Motivation

One of the principal difficulties with finite element modelling is modelling the correct mechanical properties for the materials involved. This is especially difficult with biological tissue. A stress-strain curve is an extremely important graphical measure of a materials mechanical properties. As well as mechanical properties the simulation must also correctly factor in geometry, mesh, boundary conditions, loads, and contact parameters. Because most deformations of biological materials are nonlinear, as shown in Figure 3.1, the capability of a simulation to model nonlinear mechanical properties is essential. In many previous studies [54], the stress-strain relationship was assumed to be linear behaviour for simplicity, which produced inaccurate results except at small deformations at which the linear assumption gives a reasonable approximation.

In this chapter, firstly, a comparison between the computational model and the theoretical solution for the radial deformation of a thick wall tube for a linear material properties is presented. Secondly, in order to use the stress-strain curve

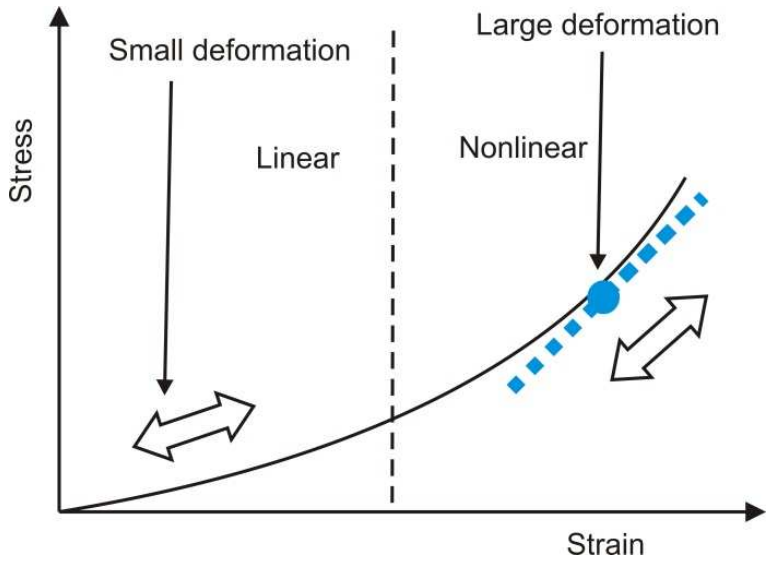

Figure 3.1: Nonlinear stress-strain relationship in a biological material.

for a non-linear material property, an equivalent strain is formulated in the Y-code. Then, by use of this formulation and stress-strain curve, a computational simulation model is studied. To validate this computational simulation, a novel analytical solution for nonlinear material deformation is introduced. This solution was implemented using C programming. Comparisons are made between the results of the analytical and computational models for a nonlinear material property to give greater confidence in the results presented in the following chapters.

3.2 Predication of Radial Deformation by Modelling a Linear Stress/Strain Relationship

3.2.1 Model Description

A thick walled circular cylindrical shell of outer radius r_0 and inner radius r_i is considered and the pressures on the inner and outer surfaces of the circular cylindrical shell are P_i and P_0, respectively, as shown in Figure 3.2. The stress

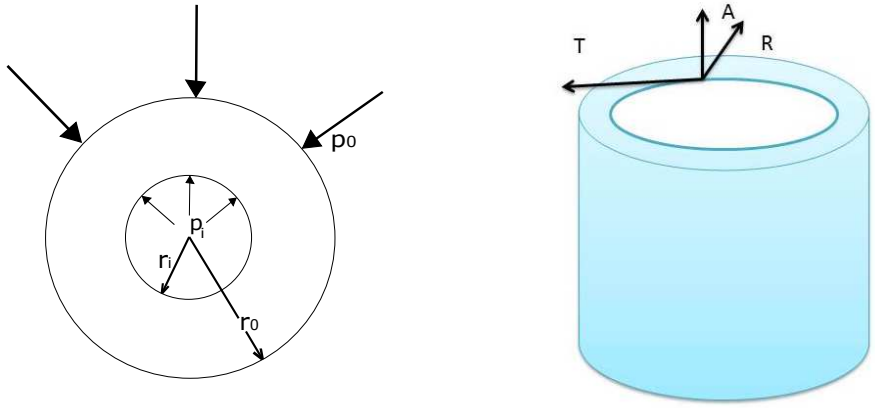

Figure 3.2: A cross-sectional and isometric view of a thick walled circular cylindrical shell.

components are respectively, defined in terms of tangential (T), radial (R) and axial (A) stress. In this case the circular cylindrical shell has open ends (as in the current model) and there is no axial component of stress. The exact elastic solution for the circular cylindrical shell under stress can be obtained using Lames equation.

For this particular example we consider a circular cylindrical shell of 0.6 cm outer diameter, 0.1 cm thickness and of length of 8 cm is simulated. As the thickness is greater than one-tenth of the radius, it can be treated as a thick walled cylinder. The modulus of elasticity (E) of the elastic material was defined as 5 Kpa and *Poissons* ratio (ν), was defined as 0.35.

3.2.2 Analytical Model

Radial displacement can be obtained from Eq 3.1, the equation of equilibrium for an element of material in polar coordinates for axisymmetric problems assuming there are no body forces. This equation describes how the internal/external pressures on the circular cylindrical shell relate to its radial displacement [78].

$$\frac{d\sigma_r}{dr} + \frac{\sigma_r - \sigma_\theta}{r} = 0 \tag{3.1}$$

Figure 3.3 shows an element of radius r defined by an angle increment dθ, a radial increment dr and the radial and tangential stresses denoted σ_r and σ_θ (a function of r) . The shear stress on the element is zero and, for an element of unit thickness, the equation of equilibrium can be written as follows in Eq 3.1:

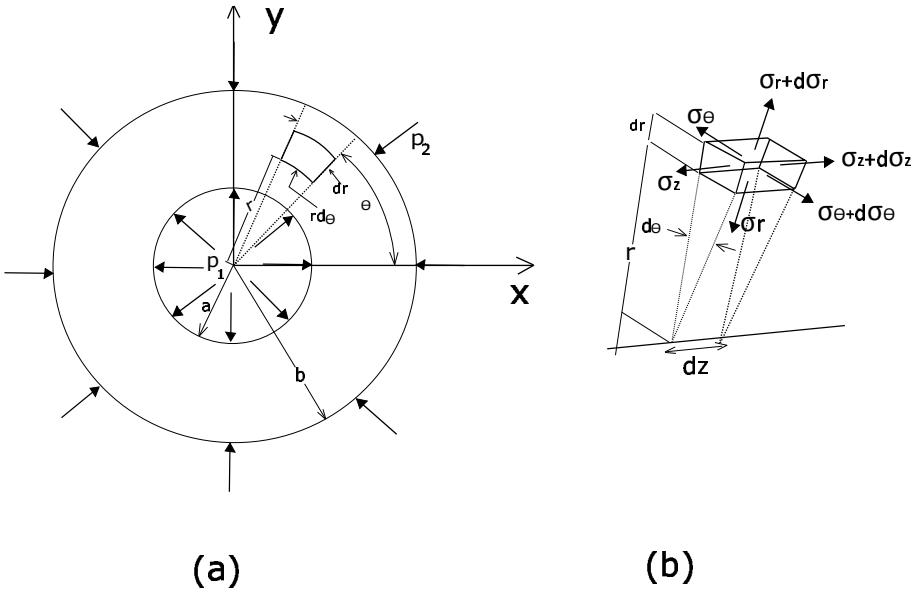

Figure 3.3: Stress in thick-wall cylinder. (a) Thin annulus of thickness dz. (The Z axis is perpendicular to the plane of figure.) (b) Cylindrical volume element of thickness dz.

The radial strain and tangential strain are respectively described as $\epsilon_r = \frac{du}{dr}$ and $\epsilon_\theta = \frac{u}{r}$ respectively where u is the radial displacement and, since the end of the model is open, axial stress σ_z=0. From Hooke's law, ϵ_r and ϵ_θ can be desired as;

$$\epsilon_r = \frac{du}{dr} = \frac{1}{E}(\sigma_r - \nu\sigma_\theta) = 0 \tag{3.2}$$

$$\epsilon_\theta = \frac{u}{r} = \frac{1}{E}(\sigma_\theta - \nu\sigma_r) = 0 \tag{3.3}$$

where E is the Young's modulus and ν is the Poisson's ratio.

Solving for the stresses yields equations 3.4 and 3.5

$$\sigma_r = \frac{E}{1-\nu^2}[\frac{du}{dr} + \nu\frac{u}{r}] \tag{3.4}$$

$$\sigma_\theta = \frac{E}{1-\nu^2}[\frac{u}{r} + \nu\frac{du}{dr}] \tag{3.5}$$

After substituting these expressions into the equation of equilibrium (Eq 3.1), we obtain:

$$\frac{d^2}{d}\frac{u}{r^2} + \frac{1}{r}\frac{du}{dr} - \frac{u}{r^2} = 0 \tag{3.6}$$

The solution of this (radial displacement) is $u = c_1 r + \frac{c_2}{r}$ giving stresses are:

$$\sigma_r = \frac{E}{1-\nu^2}[c_1(1+\nu) - c_2(\frac{1-\nu}{r^2})] \tag{3.7}$$

$$\sigma_\theta = \frac{E}{1-\nu^2}[c_1(1+\nu) - c_2(\frac{1-\nu}{r^2})] \tag{3.8}$$

The following boundary conditions can then be applied:

- $\sigma_r(r_i) = P_i$
- $\sigma_r(r_0) = P_0$

Constant c_1 and c_2 can be obtained from Eq 3.9 and Eq 3.10.

$$c_1 = \frac{(1-\nu)}{E}[\frac{(-P_i r_i^2 + P_0 r_0^2)}{r_0^2 - r_i^2}] \tag{3.9}$$

$$c_1 = \frac{(1+\nu)}{E}[\frac{(-P_i + P_0) r_i^2 r_0^2}{r_0^2 - r_i^2}] \tag{3.10}$$

U_r in Eq. 3.11 is the displacement in radial direction due to external and internal pressurization.

$$U_r = \frac{(1-\nu)}{E}[\frac{(-P_i r_i^2 + P_0 r_0^2)}{r_0^2 - r_i^2}]r + \frac{(1+\nu)}{E}[\frac{(-P_i + P_0) r_i^2 r_0^2}{r_0^2 - r_i^2}]\frac{1}{r} \tag{3.11}$$

where P_i is uniform internal pressure, P_0 is uniform external pressure and r is the radius that varies between r_i and r_0.

3.2.3 Analytical Solution with a Linear Stress-Strain Relationship

Assuming the pressure values in Table 3.1, the radial displacement is calculated by the model equations described above. The result from the model are listed in Table 3.1 where

r_0= 0.3 cm, r_i= 0.2 cm, P_i =0 Barye, E=50000 Barye and ν is 0.35.

Table 3.1: The Parameters used in the Model.

P_o=Pressure = force/Area (Barye)	Radial displacements (cm)
2500	0.0345
3750	0.0517
6250	0.086
8750	0.012
11250	0.15525

3.2.4 Computational Simulation

3.2.4.1 Model geometry

A circular cylindrical shell with the geometrical features described below was designed using the *Abaqus* software resulting in a model with 10433 tetrahedral elements. Fig 3.4 shows the three dimensional model geometry of the circular cylindrical shell and the cross section of the model used for this simulation.

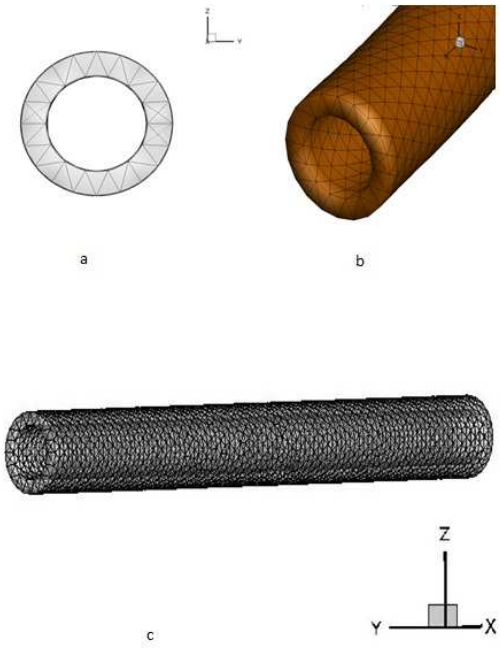

Figure 3.4: Mesh arrangement, (a,b) in cross section of the tube and (c) in tube

A cylinder with a 0.1 cm thickness is considered. The geometrical parameters are the same as in analytical model with the length around 8 cm . The model was meshed using *Abaqus* software, resulting in 10353 tetrahedral elements and 3475 nodes. The minimum size of each element was around 0.01cm and the nodes were uniformly distributed. Since CGS unit is used in Y code, all parameters are calculated in CGS unit Table 3.2.

Table 3.2: The CGS unit used in Y-code.

Quantity	Force	Length	Velocity	Pressure	Viscosity
Abrivation,Definition	dyne , g.cm2/s2	cm	cm/s	Barye(Ba),g/(cm.s2)	poise, g/(cm.s)

3.2.4.2 Boundary Conditions

The tube wall was fixed at the axial faces of the tube and forces were applied to each node on the outer surface to simulate the external pressure. This pressure was varied from 2500 to 11250 Barye, which is equivalent to forces from 20 to 90 dyne at each node. To apply the force on each node on the surface, a centre line was assumed as a reference, $\vec{X_p}$= (x_p,y_p,z_p) was defined as a point on the surface and $\vec{X_c}$= (x_c,y_c,z_c) = (x_c,0,0)) was defined as a point on the central line. The force components can be obtained using the following equations:

$$n_x = \frac{x_p - x_c}{\sqrt{(x_p - x_c)^2 + (y_p - y_c)^2 + (z_p - z_c)^2}} \tag{3.12}$$

$$n_y = \frac{y_p - y_c}{\sqrt{(x_p - x_c)^2 + (y_p - y_c)^2 + (z_p - z_c)^2}} \tag{3.13}$$

$$n_z = \frac{z_p - z_c}{\sqrt{(x_p - x_c)^2 + (y_p - y_c)^2 + (z_p - z_c)^2}} \tag{3.14}$$

$$f_x = f * n_x \tag{3.15}$$

$$f_y = f * n_y \tag{3.16}$$

$$f_z = f * n_z \tag{3.17}$$

Because of the coordinate of (x_c,0,0), then f_x= 0.

$$n_x = 0 \tag{3.18}$$

$$n_y = \frac{y_p - y_c}{\sqrt{(y_p - y_c)^2 + (Z_p - Z_c)^2}} \tag{3.19}$$

$$n_z = \frac{z_p - z_c}{\sqrt{(y_p - y_c)^2 + (Z_p - Z_c)^2}} \tag{3.20}$$

$$f_x = 0 \tag{3.21}$$

$$f_y = f * n_y \tag{3.22}$$

$$f_z = f * n_z \tag{3.23}$$

3.2.4.3 Computational Solution with a Linear Stress-Strain Relationship

To apply the correct force on the each node on the model, the equivalent force is obtained by using the same pressure value which was used in the analytical sections. The area and force are calculated as:

Area S = $\frac{\pi DL}{N}$ = 0.008 cm^2, Number of surface nodes (N)= 2024,

Table 3.3 shows the computational results with linear stress-strain relationship.

Table 3.3: Computational results with linear stress-strain relationship

Force(dyne)	Pressure(Barye)	Radial displacements (cm)
20	2500	0.0254
30	3750	0.04538
50	6250	0.07897
70	8750	0.115
90	11250	0.1518

3.2.5 Comparison between the Analytical and and Computational Results

The predicted deformation obtained from the analytical theory of a thick-walled circular cylindrical shell (*Lam*s equations) and the computational simulation are compared to verify the validity of the analytical model. Figure 3.5 shows a graphical representation of the analytical and computational results for external force. In this figure radial displacements obtained from both the analytical and computational methods appear to linearly with the applied external pressures. The results obtained from the two techniques are in good agreement.

3.3 Predication of Radial Displacement with non-linear Stress/strain Relationship

3.3.1 Model Description

The Mechanical properties of the ureter have been discussed in pervious chapters and it shows for highly deformable ureteral wall, a nonlinear stress/strain relationship material property or viscoelastic models represent ureteral wall more realistically. A non-linear stress strain relation data from Yin et al. [43] is used to simulate the non-linear stress strain relationship. Figure 3.6 shows the extracted points from their results which are used to calculate the shear modulus in order to

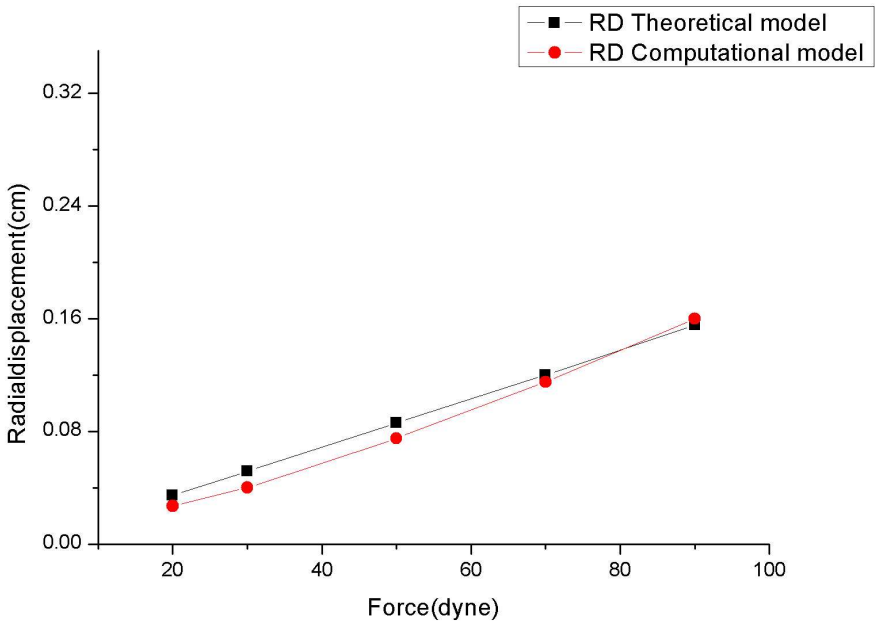

Figure 3.5: Comparison between theoretical and computational radial displacements.

obtain the strain tensor. Since the radial displacement equation uses a constant E, it needs to be modified to account non-linear changes, see Figure 3.6.

3.3.2 Computational Simulation

To introduce the nonlinear tensile properties of the ureter into the Y-code, a scalar quantity called *Equivalent Strain* is used to mimic the nonlinear stress/strain curve. Equivalent strain (also called *Von Mises* strain) is often used in design work because it allows any arbitrary three-dimensional strain state to be represented as a single positive strain value. In the mechanics of materials, an equivalent strain is defined by Eq 3.24 where ν is Poisson ratio and ϵ_{11}, ϵ_{22}, ϵ_{33}

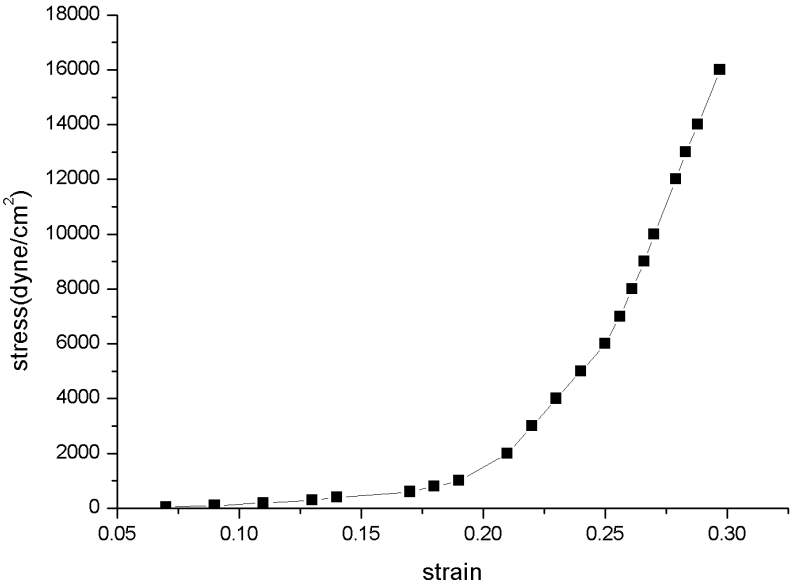

Figure 3.6: Stress strain curve extracted from experimental data obtained by Yin et al. [43].

are principal strains and ϵ_{12}, ϵ_{23}, ϵ_{31} are shear strains from the strain tensor E.

$$\epsilon_\nu = \frac{1}{1+\nu}\sqrt{\frac{(\epsilon_{11}-\epsilon_{22})^2+(\epsilon_{22}-\epsilon_{33})^2+(\epsilon_{11}-\epsilon_{33})^2+6(\epsilon_{12}^2+\epsilon_{23}^2+\epsilon_{31}^2)}{2}} \tag{3.24}$$

Where

$$E = \begin{bmatrix} \epsilon_{11} & \epsilon_{12} & \epsilon_{13} \\ \epsilon_{21} & \epsilon_{22} & \epsilon_{23} \\ \epsilon_{31} & \epsilon_{32} & \epsilon_{33} \end{bmatrix} \tag{3.25}$$

By implementing the equivalent strain in the Y-code, the multitude of strains in computational model become equivalent to the uniaxial strain from the experimental study.

From the stress-strain curve (Figure 3.6), a dataset defining the shear modulus/equivalent strain is extracted. This data set is used as an input file into Y-code for the simulation.

When the strain tensor is calculated, the equivalent strain is also calculated according Eq 3.24. Then, by referring to the shear modulus/equivalent strain input files , the correct shear modulus is determined and the Cauchy stress is calculated in terms of that shear modulus.

Before the method was applied to the circular cylindrical shell model, the equivalent strain design was used to simulate the deformation of a single element with an axial displacement in the z direction as shown in Figure 3.7. Figure 3.7 shows a tetrahedral element under uniaxial displacement in the Z direction. For this element, uniaxial displacement is caused by displacing node 3 in the Z direction. During the deformation, output data from the equivalent strain is obtained every few time steps and plotted against the experimental data, as shown in Figure 3.8. The results are also in good agreement with those measured experimentally.

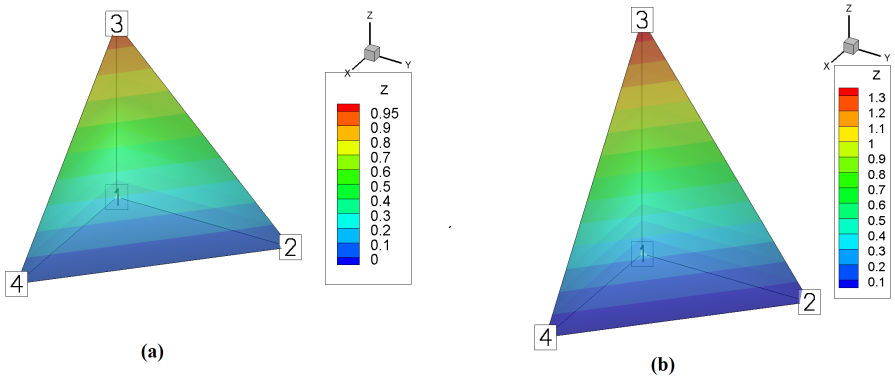

Figure 3.7: Displacement in the principle direction of one element (a) before deformation and (b) after deformation. Contours show the Z position on the element surface in cm.

For further validation of the accuracy of the computational model, the second simulation is studied by applying displacement in the principle direction in such a way that it is applied at 3 nodes in each time step, as shown in Figure 3.9. Node 3

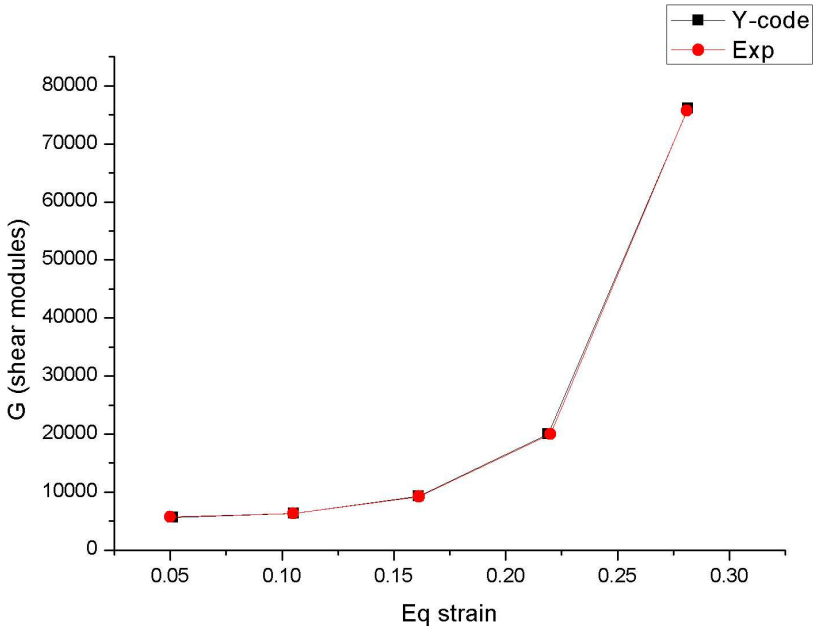

Figure 3.8: Comparison of relationship between shear modulus (dyne/cm2) and *Equivalent Strain* for a single element.

in the Z direction (ϵ_{33}), node 4 in the X direction (ϵ_{11}) and node 2 in the y direction (ϵ_{22}) are moved while node 1 is fixed. The black arrows show the direction of the deformations. As shown in the Figure 3.10 the equivalent strain/shear modulus results are very close to the experiment data. These results confirm the accuracy of the computational code for a single element, supporting the use of this technique for further investigation using the aforementioned circular cylindrical shell model.

The graphs 3.8 and 3.10 showing deformation of a single element in one and two directions confirms the accuracy of the computational simulation technique with use of the nonlinear stress/strain curve and they show good agreement with experiment data. This computational simulation of a thick walled circular cylindrical tube under deformation with nonlinear tensile properties is now investigated. The geometry and mesh properties are the same as the linear model. Table 3.4 shows the external pressures values and corresponding radial displace-

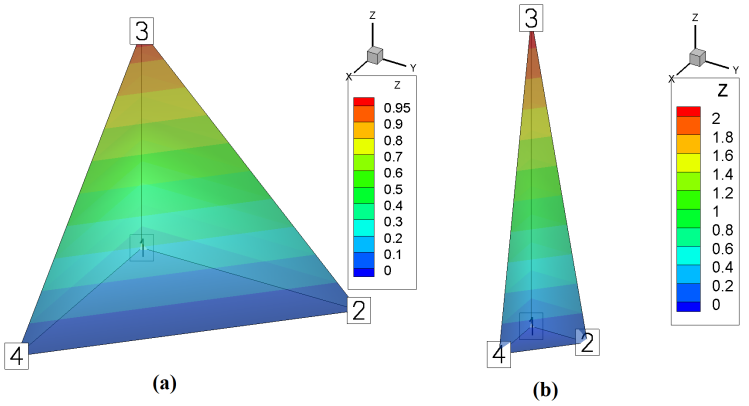

Figure 3.9: Displacement in the principle direction of one element (a) before deformation and (b) after deformation. Contours show the Z position on the elements surface in cm.

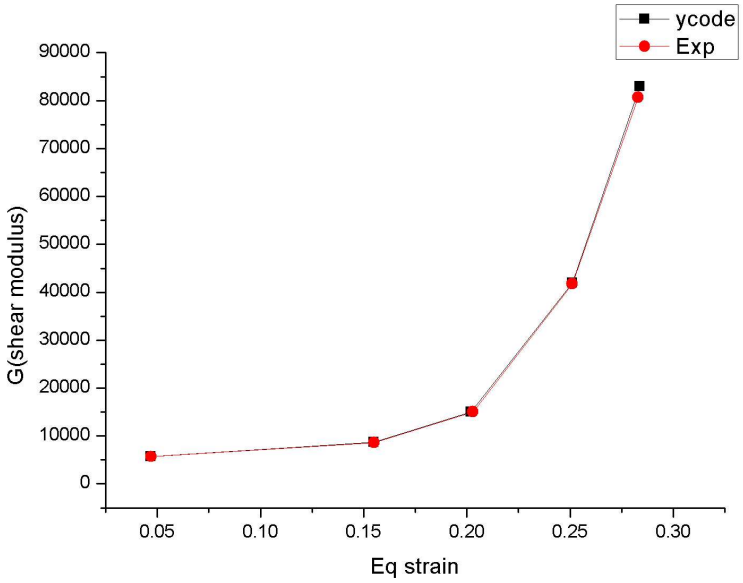

Figure 3.10: The comparison graph of shear modulus (dyne/cm2)/equivalent strain relationship in simulations and experiments.

ments predicted by the simulation.

Table 3.4: The parameters are used in model with nonlinear material properties.

P_o=Pressure = force/Area (Barye)	Force (dynes)	Radial displacements (cm)
2500	20	0.055
6250	50	0.078
11250	90	0.097
15000	120	0.1

To better understand the effect of the nonlinear tensile properties in our model, Figure 3.11 shows a comparison between the numerical simulations with linear and nonlinear stress-strain relationships. It is clear that the linear theory overestimates the displacement at forces of greater than 50 dyne. For example, when the force is around 70 dyne, the linear and nonlinear models predictions of radial displacement are 0.11 and 0.085 respectively, giving an overestimate of 29.4% from the linear model. The linear stress/strain only provides an accurate prediction at small deformations. Further validation for our computational code is provided by comparing the analytical and computational solutions for radial displacement using a nonlinear stress-strain relationship in the tube wall.

3.3.3 Analytical Solution

Since a theoretical solution for the radial displacement of a material with a nonlinear stress/strain relationship is not published in the literature, an iterative solution was designed to calculate the radial displacement based on data from the nonlinear stress/strain graph (Fig. 3.6).

The developed method was based on the linearization of segments. The following flowchart (Fig. 3.13) shows the algorithm of this method. An input file of equivalent strain/shear moduli according to the previously described experimental study was used. The algorithm can be described as follows:

- Step1: External and internal pressure are divided by i=100. Then P_{outer} and P_{inner} are estimated as $P_{outer} = P_0 /100$ and $P_{inner} = P_i/100$ respectively.

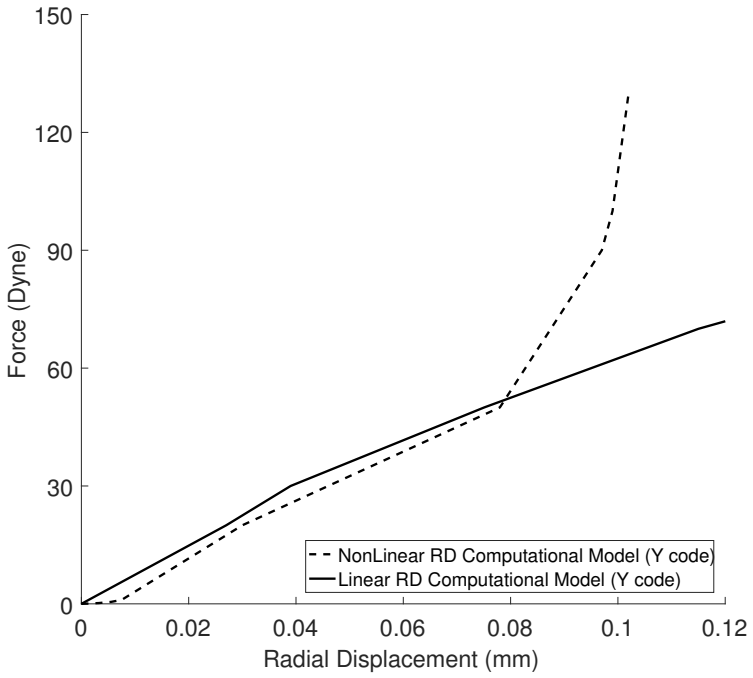

Figure 3.11: The comparison between linear and non -linear radial displacement.

- Step2: In this step, the initial values of strain and radial displacement are set to zero as follows (where i=0)

  e_r^i=0

  Δu_r^i=0

- Step 3: In this step, a loop is initiated to measure radial displacement incrementally by use of P_{outer} and P_{inner}. According to the value of strain e_r^i , the Young's modulus, E_i is obtained from the input data file ($Young's$ modulus/$Equivalent\ strain$ data) by mean of interpolation based on the value of strain $e^j{}_r$.

- Step 4: In this step, the radial displacements of two points located on the inner and outer surface of the shell respectively, are calculated by use of equation 3.11. The difference between these values is also obtained. u_r^i = u_{ii}^i - u_{00}^i, where r_{inner} =0.2cm and r_{outer} = 0.3cm.

- Step 5: In this part, the strain value is obtained.

  $\Delta e_r^j = \frac{\Delta u_r^i}{r_{inner} - r_{out}}$

- Step 6: The new radius r_{inner} and r_{outer} are updated as follows:

  $r_{inner} = r_{inner} - u_{ii}^i$

  $r_{outer} = r_{inner} - u_{00}^i$

- Step7: The strain is updated as follows:

  $e_r^j = \sum_{i=1}^{n} \triangle e_r^j$

- Step 8: Radial displacements U_{inner} and U_{outer} are also updated for the two points located on the inner and outer circle of the shell:

  $U_{inner} = \sum_{i=1}^{n} u_{ii}^i$

  $U_{outer} = \sum_{i=1}^{n} u_{oo}^i$

- Step 9: This step is a decision box which, if satisfied, returns to step 3 and a new E_i is obtained through the data file (*Young's* modulus/*Equivalent Strain* data) according to the updated strain. If the condition is not satisfied, the loop ends and moves to step 7.

- Step 10: In this step, the final value of radial displacement U_{inner} and U_{outer} for any point on the inner surface and outer surface is returned.

3.3.4 Comparison between Computational and Analytical Results

The nonlinear stress/strain relationship discussed in Section 3.3.2 was used to numerically/computationally simulate the thick walled tube with the same geometry as used in section 3.2.5. Three different values of the force ranging from 0.2 to 130 dynes were used to give the radial displacements of the nodes on the outer surface. The analytical results based on the description in Section 3.3.3 for the radial displacement of a cylindrical circular shell with a nonlinear stress/strain relationship are plotted in Figure 3.12. The result shows the agreement between

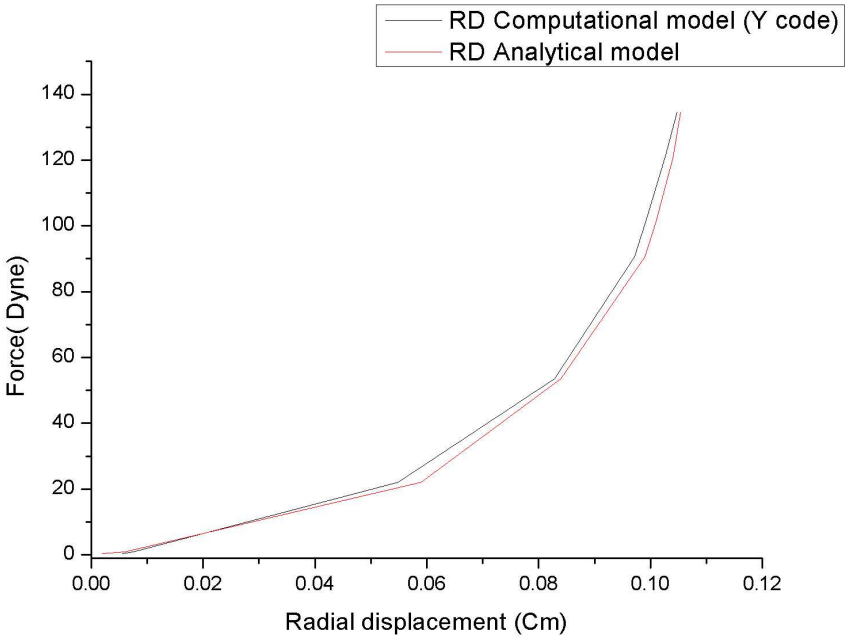

Figure 3.12: Comparison between the analytical model and computational simulation of the thick walled tube with a nonlinear stress-strain relationship under radial compressive stress.

the theoretical and computational models. In both cases the materials stiffness clearly increases as more force is applied.

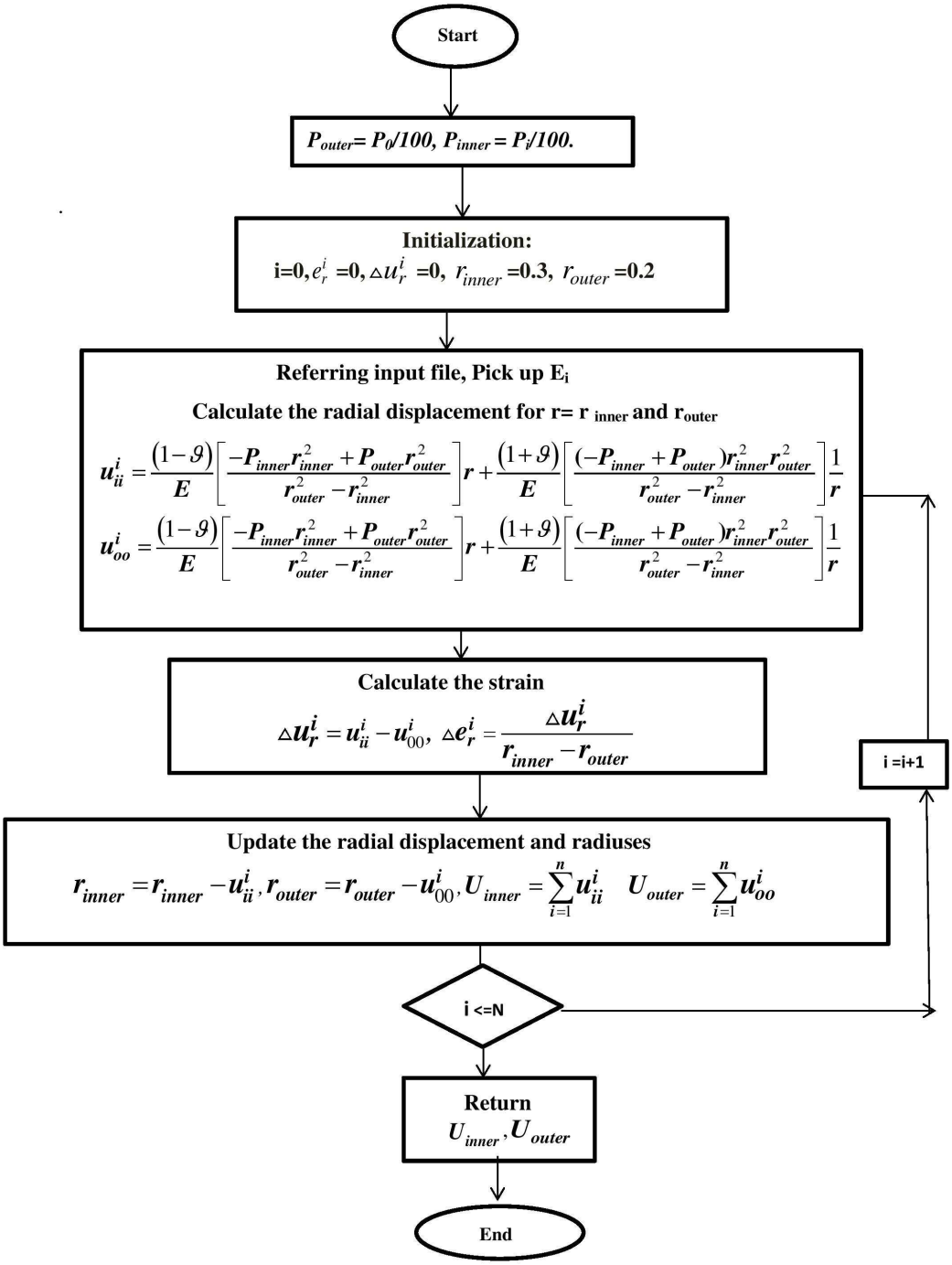

Figure 3.13: Flowchart of the iterative approaches to theoretical solution of a Radial displacement of cylindrical shell with nonlinear material property.

3.4 Summary

In this chapter an equivalent strain is implemented in the Y-code for a nonlinear material. The deformation of a circular cylindrical shell under external pressure with linear and nonlinear material properties are evaluated with analytical and computational solutions. For a material with nonlinear properties, an analytical solution is introduced by using an iterative approach in order to validate the computational model. From comparison between linear and nonlinear stress/strain models, it is clear that the deformation of a ureter will be more accurate and similar to reality of the ureter wall using a nonlinear stress/strain curve relationship. All results show good agreement with the experimental data. Based on the work described in this chapter, the computational technique can be extended to a more geometrically complex ureter model and further investigations can be carried out, as described in the next chapters.

Chapter 4

Development of an Anatomical Computational Model of the Ureter

4.1 Motivation

This chapter describes the use of an anatomically correct finite element model of a ureter system. Although the computational simulation of ureters has been investigated in prior studies [54, 79], an anatomically correct ureter geometry has not been investigated to the best of our knowledge. This geometry is difficult to model due to its complexity and asymmetrical shape. There is also a wide range of curvatures on the ureter geometry, so this model requires a high grid resolution for both solid and fluid parts in order to obtain reliable computational results. This adversely affects the computational time and cost. The model presented in this study demonstrates a computational result which more closely matches the clinical data.

4.2 Development of a Finite Element Model for the Ureter

This part of the study was conducted in collaboration with *Whipps Cross* Hospital and *Urology Innovation* centre. Fifty different *CT* scans of urinary systems of female and male patients aged over 30 years old were obtained from both organisations. Each image has been examined individually to ensure it is free from any obstruction or disconnection. The CT scans were obtained as a series of 350 *DICOM* (Digital Imaging and Communications in Medicine) images, each slice with a thickness of 1.5 mm, as shown Figure 4.1. Among all the *CTs*, the best one from a female candidate that showed a clear geometry of the ureter without any complication was selected.

Figure 4.1: One of the slices of a typical IUV scans (contrasted)

4.2.1 Creation of 3D Geometry of the Ureter.

The *CT* scans were imported into the image-processing package *Mimics* 14.01 which is software developed by *Materialise* Company specifically for medical image processing. This software takes in a number of 3D medical image segmentations of a patients anatomy, which can be extracted from *CT*, *MRI*, *micro-CT*, *CBCT*, 3D *Ultrasound* and *Confocal Microscopy*, and converts them into an accurate 3D model. The 3D model can then be exported to other software, such as statistical, *CAD*, or *FE* packages.

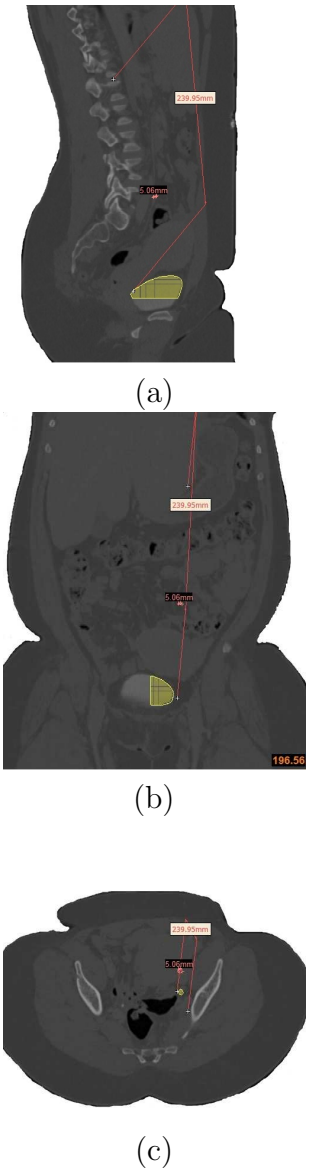

Figure 4.2: Unmodified *DICOM* images imported into *Mimics* 14.01. These scans are visible in the (a) coronal, (b) transverse and (c) sagittal planes.

In this work, a data set of more than 335 transverse *CT* scan slices with an in-plane resolution of 0.80 mm and slice to slice separation of 1.5 mm were processed. Figure 4.2 (a,b,c) show the unmodified scans of the coronal, transverse and sagittal plane in *Mimics*.

The *CT* scans of the ureter should be separated from the surrounding soft tissue. This was achieved by using the *thresholding* function in *Mimics*, which identifies the greyscale regions in the images with values between 260 and 3071.

Figure 4.3 shows the extracted 3D model of the ureter from the original scanned images where the length and the average diameter of ureter are around 239.95 mm and 5.06 mm respectively. The yellow sections at the bottom and top of the image are parts of the bladder and renal pelvis.

Because we are focusing only on the computational analysis of the ureter, the bladder and renal pelvis were ignored and removed from the model to leave just the ureter. This was achieved by manually deleting the bladder and renal pelvis segments. Figure 4.4 shows a cropped 3D model of the ureter which has a length of 199.52 mm. It can be seen that there is evidence of deformations, which we assume to be the peristaltic contractions. The diameter and length of the ureter can be obtained from the produced 3D model, however, due to its microscopic scale and consecutive cross-sectional changes along its length, this model failed to provide a clear geometrical information.

This problem was resolved by adopting the cross-section shape used in the study conducted by Hammersen et al. [12]. Figure 1.2 from the Introduction (1) shows the coordinates of the outer and inner surface of the cross-section, extracted from the study conducted by Hammersen et al. [12] using *Plot Digitizer* 2.6.8 software. A 3D model of the ureter was created using *ICEM* software using the

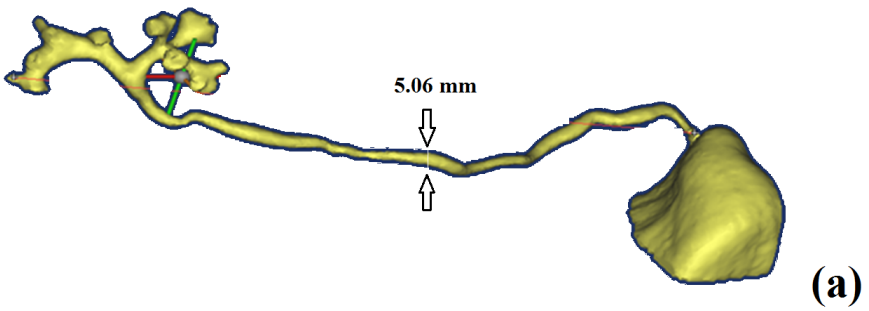

Figure 4.3: Extracted 3D model of the ureter.

assumption that the ureter cross-section was constant along the ureters centre line, as shown in Figure 4.5.

The centre line of the 3D geometry was obtained using *Mimic* software and the resulting 3D model gave a fair approximation of the ureters geometry. In this model the complex geometry of the iliac vessels is preserved. This model is more complex than the model used in previous computational studies [54] in which the shape of the ureter is simplified to a thick walled tube.

4.2.2 Initial Meshing of Ureter Model

For this study, *ICEM* 15.0 was used to create the tetrahedral mesh to be used for the structural model. The cross-section surface was meshed using the curve mesh function in *ICEM* for both the inner and outer surface curves. Next, the surface mesh was extruded along the models centre line with a fixed spacing to create a longitudinal 3D mesh. All generated elements were converted into tetrahedral elements and finally all node numbers in each slice were rearranged in ascending order from 1 to the maximum number in order to be compatible with the Y-code.

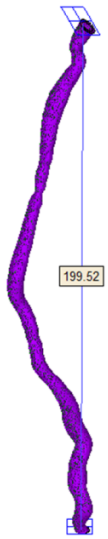

Figure 4.4: Cropped 3D model of the right ureter.

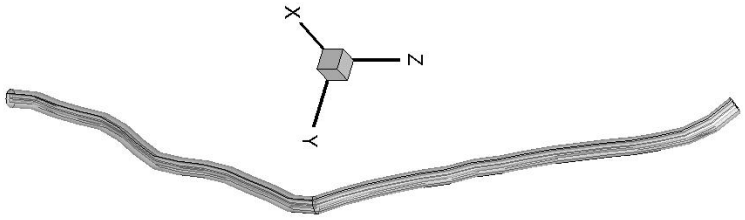

Figure 4.5: The modified geometry of the 3D mimic software model.

Due to the complex shape of the ureters lumen, it was important to keep the number of nodes high enough to ensure that the geometry of the native organ was accurately preserved. Consequently, a mesh quality study was performed at this point in the process to ensure a suitable compromise between computational performance and time.

As described in Chapter 2, the fluid code (*Cgles*) is **fully parallelised** but the solid codes (*Y*-code) are only **partially parallelised**. *Cgles* and *Y*-code use *MPI* and Open *MP* respectively for parallelisation. Further there were a limited number of nodes for this project available to concurrently run the solid and fluid parts in parallel. The UK National Supercomputing Service (*Archer*), with more than 4920 computational nodes, was also available for our research. However our access to this was sporadic, since Archer only offered limited hours with limited number of nodes for academic research projects. This limit to the available computational power constrained the compromise between dense meshes which maximised accuracy and coarser meshes that could be completed in a reasonable time frame.

4.2.3 Mesh Quality Study

To evaluate the effect of mesh resolution on the computational time, we created five different solid meshes using the described anatomically accurate ureter model with different numbers of nodes and elements. These are presented in Table 4.1. By increasing the element sizes, the solving time decreases. The length of the time step is dependent on the smallest edge of an element. The approximate

computational time required to solve Meshes 1 to 5 decreases from 30 s to 1.3 s on the QMUL cluster.

Table 4.1: The approximate computational time required to run mesh 1 to 5 with the current existing computational resources.

Solid	Number of elements	Number of nodes	Min element size (cm)	Element size in longitudinal direction(cm)	Number of nodes in cross section	Solid Time step (sec)	Number of threads / Average time of solving solid on Archer cluster (sec)	Number of threads /Average time of solving on Apocrita cluster (sec)
Mesh 1	88608	18550	0.0001	0.7	420	e-7	6/9	8/30
Mesh 2	33930	7688	0.0008	0.7	248	e-7	6/4	8/20
Mesh 3	18000	4309	0.001	0.7	139	e-7	6/3	8/12
Mesh 4	6700	1891	0.005	0.7	61	e-5	6/1.5	8/4
Mesh 5	5039	1271	0.04	0.7	41	e-5	6/0.3	8/1.3

Figure 4.6(a-e) shows the cross-sections of the ureter model with different numbers of nodes. Figure 4.6(a) has the finest mesh with the maximum number of nodes and Figure 4.6(e) has the coarsest mesh with the minimum number of nodes. Although for fine mesh cases such as Meshes 1 and 2, the anatomically accurate stellate shape of a native ureter is clearly preserved, 8-10 seconds are required to solve the solid part in each small time step. The time for Meshes 4 and 5 is much less.

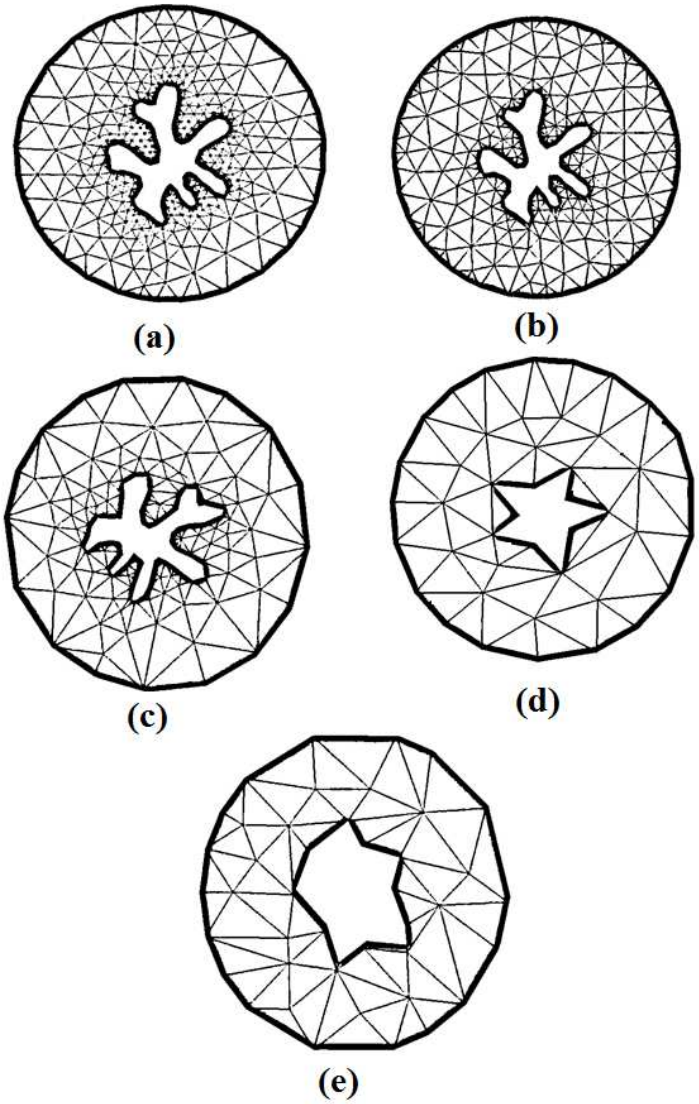

Figure 4.6: Different number of mesh quality was created to use in order to find the best one for this simulation.

For this study, it was not feasible from the time perspective to run the cases with the fine and medium mesh (Mesh 1, 2, 3). To give maximum accuracy with a reasonable solution time, Mesh 4 was selected for this investigation. To ensure that the structural simulation results with Mesh 4 would not be altered by further mesh refinement, a mesh-independent analysis was carried out.

Similar to a study conducted by Shashikant et al. [80], for this study the Von Mises stress variable was selected as a benchmark for mesh-independent analysis of the solid part. Von Mises stress is a scalar value which is computed from the Cauchy stress tensor (shear stress and principle stress) as presented in equation 5.1.

$$\sigma_\nu = \sqrt{\frac{(\sigma_{11} - \sigma_{22})^2 + (\sigma_{22} - \sigma_{33})^2 + (\sigma_{11} - \sigma_{33})^2 + 6(\sigma_{12}^2 + \sigma_{23}^2 + \sigma_{31}^2)}{2}} \tag{4.1}$$

The Von Mises stress was calculated on a single observation node in the contraction area. A radial force with a magnitude of 500 dyne was imposed on the outer wall, and Von Mises stress was calculated after 10 time steps for Meshes 1 to 5.

Figure 4.7 shows the Von Mises stresses from the different mesh resolutions. Mesh 5, with the highest resolution, has the greatest stress of $4.8\times e^4$ (barye) and mesh 1 with the coarsest resolution shows the lowest stress of $3\times e^4$ (barye).

Mesh 4, which has been selected for our study, shows a stress of $4.7e^4$ (barye) and an error of less than 5% compared to Mesh 1. The mesh-independent analysis has therefore shown that the selection of mesh 4 is a suitable compromise between accuracy and computational cost.

4.3 Development of the Fluid Domain

Figure 4.8 shows the fluid domain used for the ureter model. The fluid domain has a rectangular cuboid shape which extends 22.5 cm in the Z direction, 0.5 cm in the X direction and 4 cm in the Y direction. As shown in Figure 4.8, due to the asymmetric volute shape and long length of the ureter, a large fluid domain is required to enclose the whole ureter model.

A wide range of fluid grid resolutions was examined in order to obtain an optimal compromise between accurate computational results and computational cost. Table 4.2 shows the required computational times to solve for seven tested fluid domains with different resolutions in the x and y and z directions. For all cases, the boundary conditions were an inlet pressure of 1 cm h_2o and an flow boundary condition at the outlet.

Table 4.2 shows that as the grid resolution improves, the computational cost increases. It is shown that Domain 1, with an element size of $0.015 \times 0.017 \times 0.046$ results in a computational time of 4 and 90 seconds per time step on Archer

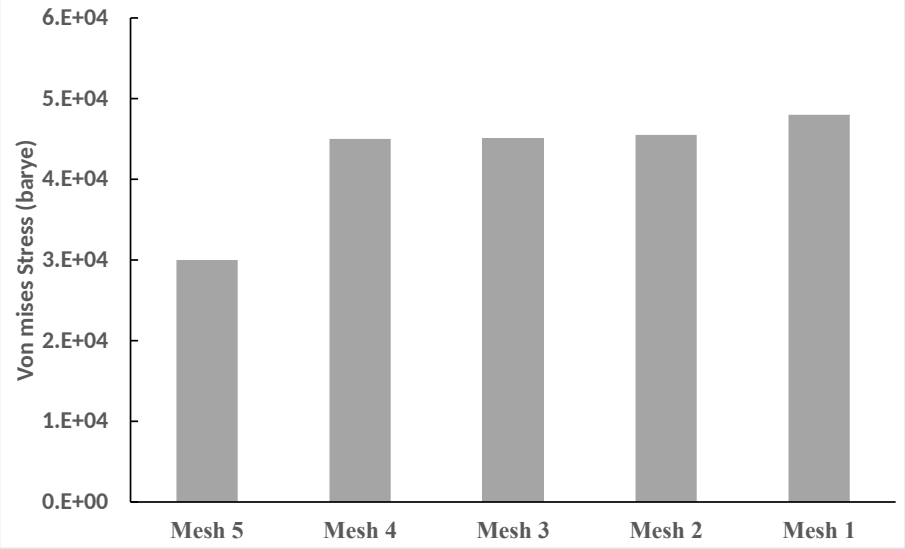

Figure 4.7: The graph of von misses stress against the different mesh resolutions

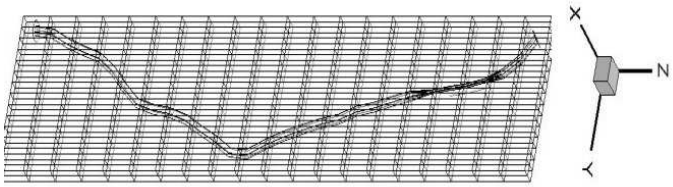

Figure 4.8: Fluid domain with used and unused block elements.

Table 4.2: The comparison of different fluid resolutions.

Fluid Domain	Number of grid in x,y,z	Grids size in x,y,z	Fluid time step	Number of processors / Average time of solving fluid on Archer cluster (sec)	Number of processors /Average time of solving fluid on Apocrita cluster (sec)
Domain 1	$32 \times 224 \times 480$	$0.015 \times 0.017 \times 0.046$	e-4	32/4	24/90
Domain 2	$32 \times 224 \times 448$	$0.015 \times 0.017 \times 0.046$	e-4	32/5	24/90
Domain 3	$64 \times 448 \times 480$	$0.0078 \times 0.0089 \times 0.045$	e-4	32/4	24/100
Domain 4	$64 \times 448 \times 680$	$0.0078 \times 0.0089 \times 0.0367$	e-4	32/6	24/150
Domain 5	$64 \times 448 \times 960$	$0.0078 \times 0.0089 \times 0.02$	e-5	32/9	24/160
Domain 6	$128 \times 768 \times 640$	$0.0039 \times 0.0052 \times 0.035$	e-5	32/20	48/200
Domain 7	$128 \times 768 \times 960$	$0.0039 \times 0.0052 \times 0.02$	e-6	32/30	48/200

and Apocrita clusters respectively, whereas Domain 7 with an element size of $0.0039 \times 0.0052 \times 0.02$, eight times smaller than an element in Domain 1, results in a computational time of 30 and 300 seconds per time step on the Archer and Apocrita clusters respectively.

A mesh independent study was performed on the seven fluid domains presented in Table 4.2, in order to ensure the accuracy of our computational results. These simulations were conducted in the absence of solid contractions, and the maximum velocity at the centre of lumen was selected as the variable to determine mesh independence. For each domain, a simulation was conducted for 1000 time steps, the maximum velocities were determined and compared. Figure 4.9 shows the maximum velocity in each domain. It is evident that from Domain 1 to Domain 5, as the grid resolution improves, the maximum velocity increases gradually, however from Domain 4 to Domain 7 there was no significant difference in the maximum velocity. The mesh independent studies for the fluid domain therefore indicate that Domain 4 is a sufficiently accurate grid resolution and can

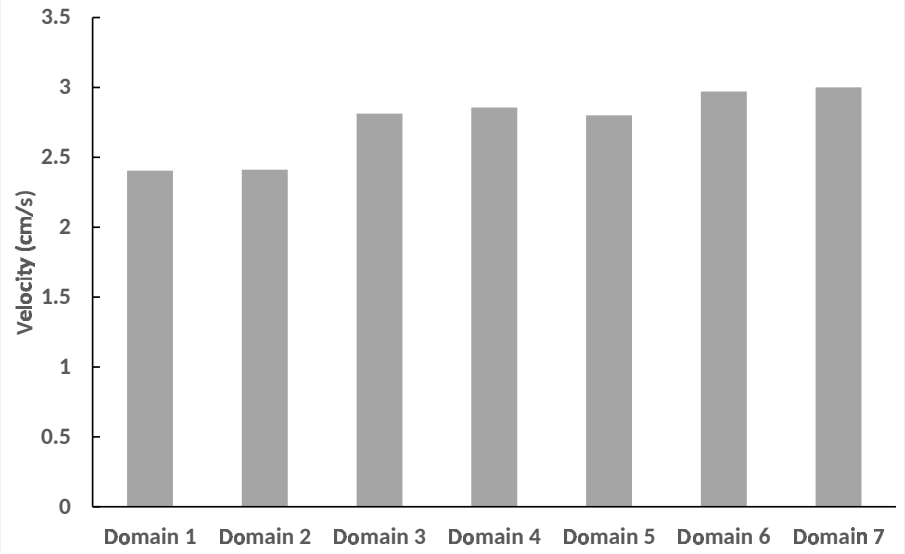

Figure 4.9: Graph of maximum velocity against the various domains.

be used for this work. Our investigation to obtain the optimal grid resolutions for the solid and fluid domains has concluded that mesh 4 for the solid part and Domain 4 for the fluid part should be selected the computational investigation of the ureter.

Using Mesh 4, the solid part takes approximately 3-4 seconds per time step on the Apocrita cluster to run the isolated solid part (ureter). Using Domain 4, it takes approximately 150 seconds per time step on the Aprocrita cluster to run the isolated fluid domain. Because the time step increment is e^{-5} s for the solid part and e^{-4} s for the fluid part, time step synchronisation is required between the fluid and solid time steps in order to obtain a time step in which both solid and fluid parts can be solved. The time step synchronisation is calculated using Eq 4.2;

$$\Delta t_{sychro} = \frac{\Delta t_{fluid}}{\Delta t_{solid}} \tag{4.2}$$

Where Δt_{fluid} and Δt_{solid} are the fluid and solid time steps, respectively. Considering Δt_{fluid} is equal to e^{-4} and Δt_{solid} is equal to e^{-5} the synchronisation time

step will be equal to ten, implying that for each fluid time step, ten solid time steps must take place. The total computational time per time step is calculated as follows:

Total computational time per one time step = computational fluid time + computational solid time×synchronization = 150 + (4×10) = 190 seconds.

In order to illustrate the actual computational time on the QMUL cluster, the computational time for a few fluid Domains (4, 5, 6) using Mesh 4 is tabulated in Table 4.3. It is worth mentioning that for 1 second simulation, the contraction only move 3.5 cm in the ureter.

Table 4.3: An approximation of the total computational time.

Fluid Domain	Fluid Time Step	Solid time step for Mesh 4	Synchronization between fluid and solid time step	Computational time for 1 time step for both solvers (s)	Computational time for 1 second (s)	Number of days to move the contraction 3.5 cm/s in ureter
Domain 4	e-4	e-5	10	150+(10×4)	10000×190	21
Domain 5	e-5	e-5	1	160+(1×4)	100000×160	185
Domain 6	e-5	e-5	1	200+(1×4)	10000×204	236

Considering the total computational time of 190 seconds per time step, it would take approximately 42 days on Apocrita and 5 days on the Archer cluster to move a contraction along the ureter. Due to the existing limitations for the assigned time and memory on each cluster, it was not practically feasible to run a single case continuously on either Apocrita or Archer cluster. Therefore, a new solution was improvised to reduce computational cost.

The fluid domain previously shown in Figure 4.8 consists of a substantial num-

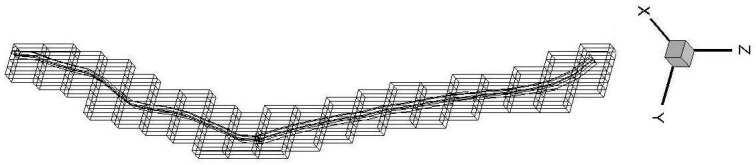

Figure 4.10: Reduced fluid domain with no unused block elements.

ber of unused blocks, which not only have no impact on the computational results, but also increase the computational cost significantly. Consequently, the size of the fluid domain was reduced by removing the unused blocks, thereby reducing the computational time. For the new fluid domain, shown in Figure 4.10, all remaining blocks are connected to each other using the free slip boundary conditions.

The new fluid domain has 213 blocks, compared to 413 in the original fluid domain. The reduced domain reduced the fluid solution computational time from 160 seconds to 75 seconds per time step, resulting in an improved computational time of approximately 20 days on the QMUL cluster.

4.3.1 Generation of Immersed Boundary Points

To establish communication between an immersed boundary (IB) point and a fluid cell point, there should exist at least one IB point for each fluid cell. A solid elements size cannot be more than twice that of a fluid grid cell/element. For mesh 4, the size of the solid element size in the Z direction is 0.7 cm, whereas the fluid size is 0.036 cm. It is apparent that there are fewer IB points than fluid cells, indicating that there will be fewer fluid cells with no connections to any IB points. To overcome this problem, the number of IB points has been interpolated from 2 to 15 for one element. Figure 4.11 shows the extracted boundary element nodes along the ureter.

The first step to create IB points is to extract the boundary surface nodes from the total solid elements. In this work, due to the asymmetric and complex geometry of the ureter model, the extraction of the boundary element surface, which is not connected to the other internal nodes, was not a straightforward procedure. An algorithm was developed specifically for this task to enable the extraction of these nodes from the boundary surface of the ureter.

In this algorithm first the nodes with a distance of more than 2 cm from the centre of the ureter cross-section will be isolated. Next, the joint elements will

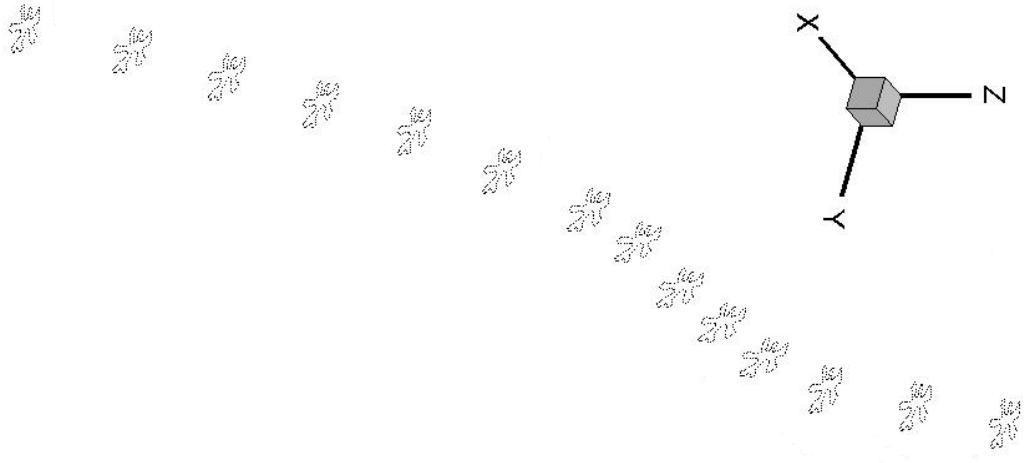

Figure 4.11: The extracted boundary element nodes on the ureter using our code.

be selected by comparing each element with other elements. Next, the algorithm checks if the summation of the distance from the furthest node to the centre of an element and the distance from the furthest node of element centre in another element are greater than the distance between the centres of each of these two elements. Next, the algorithm checks if two elements have a joint surface. Figure 4.12 shows two elements denoted A and B. The algorithm checks whether the two elements A and B are in contact with the same surface when the summation of the node IDs for element A subtracted from node ID, not in contact with element B, is equal with the summation of the node IDs for element B subtracted from node ID, not in contact with element A.

It is evident that node 1 of element A is not in contact with node 5 of element B. Therefore, the summation of the node IDs for element A is 10 (=4+3+2+1) and for element B is 14 (=4+3+2+5). It is apparent that by subtracting the non-contact node IDs (1 for A & 5 for B) from the total summation for each individual element of A and B, the same result (= 9) is obtained.

Finally, the algorithm creates a set of nodes from boundary surface nodes and transfers the velocity and coordinates from immersed boundary points. Figure 4.13(a,b) shows the interpolated set of nodes along a single fluid element

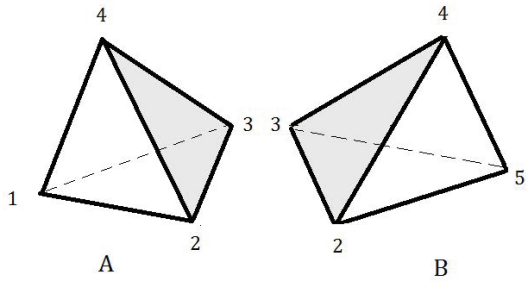

Figure 4.12: Element A result: 10-1 =9, Element B result: 14-5 =9

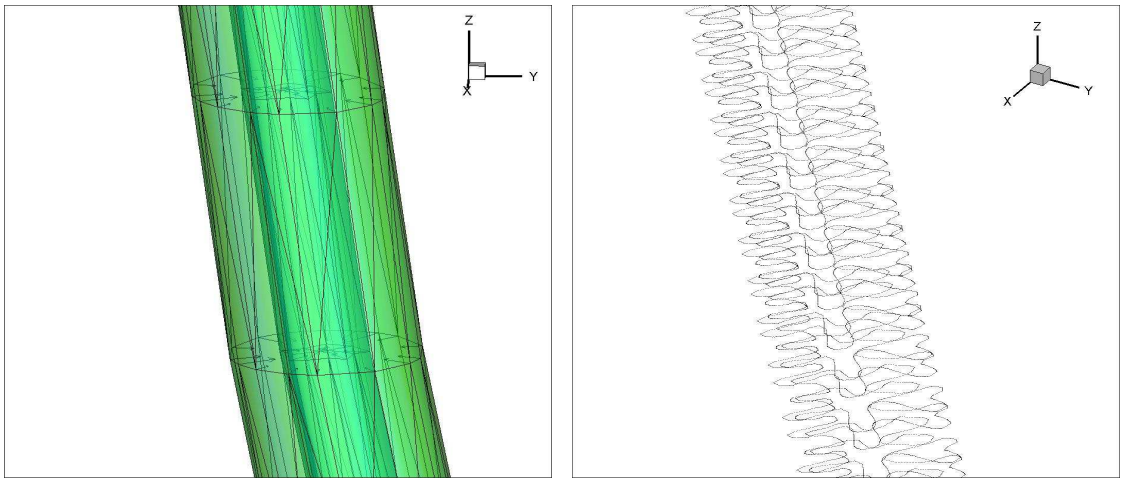

(a) (b)

Figure 4.13: One solid element with two sets of nodes on axial facing element surfaces/facets. (b) A set of 15 interpolated nodes along the same element along the Z direction.

along the Z direction.

A detailed description of the algorithm is presented in a sequential order from step 1 to step 15 as follows.

- Step 1) Calculate the coordinate of the centre for each element i.
- Step 2) Calculate the centre of each surface (triangle) of element i (each element has 4 faces) by using Step (1).

- Step 3) Calculate the distance between central lines using interpolation and calculate the centre of the sub-triangle.
- Step 4) Define (index_i) as a variable for counting the summation of node ID number in each element i , check the condition (1): if the distance is greater than 2 cm, then the element is not on the boundary surface, otherwise it is on the boundary surface.
- Step 5) Calculate the distance between the centre of the element i and each node in element i. Select the longest distance as di
- Step 6) Select the element j which is not the same as the element i
- Step 7) Define (index_j) as a variable for counting the summation of node ID number in each element j
- Step 8) Calculate the distance between the centre of the element j and each node in element j, and record the longest distance as d j.
- Step 9) Calculate variable d as the distance between two centre of two elements i and j Check the condition (2) (dj+ di ¡d), then go to step 6 and select element j+1 , if the condition 2 is not satisfied, indicating that elements i and element j may have a joint surface then, go to the next step.
- Step 10) for each node of element i, calculate i = ($index_i$) node ID which is the difference between summation of all node IDs of one element and that node ID.
- Step 11) for each node of element j, calculate j = ($index_j$)-node ID which is the difference between summation of all node IDs of one element and that node ID. Check the condition (3), If the (i==j) go to the step 12, if it is not satisfied go to step 10.
- Step 11) for each node of element j, calculate j = ($index_j$)-node ID which is the difference between summation of all node I of one element and that node ID. Check the condition (3), If the (i==j) go to step 12, if it is not satisfied go to step 10.

- Step 12) define a variable Found , for counting the number of nodes which are the same.
- Step 13) compare all nodes IDs in element i and element j and if the IDs are the same, update Found.
- Step 14) If Found =3, these node IDs are not in the inner boundary surface.
- Step 15) Select the velocity and coordinates of the boundary surface nodes, then calculate the area of the triangle using the geometry coordinates.
- Step 16) Divide each triangle surface to 64 triangles and calculate the centre of each triangles by using an interpolation techniques.
- Step 17) Update the area of each sub triangle.
- Step 18) Transfer the coordinate and velocity of each of triangle centre as a new immersed boundary node.

Figures 4.14 and 4.15 show the flowchart of the algorithm in which the whole procedure is described step by step.

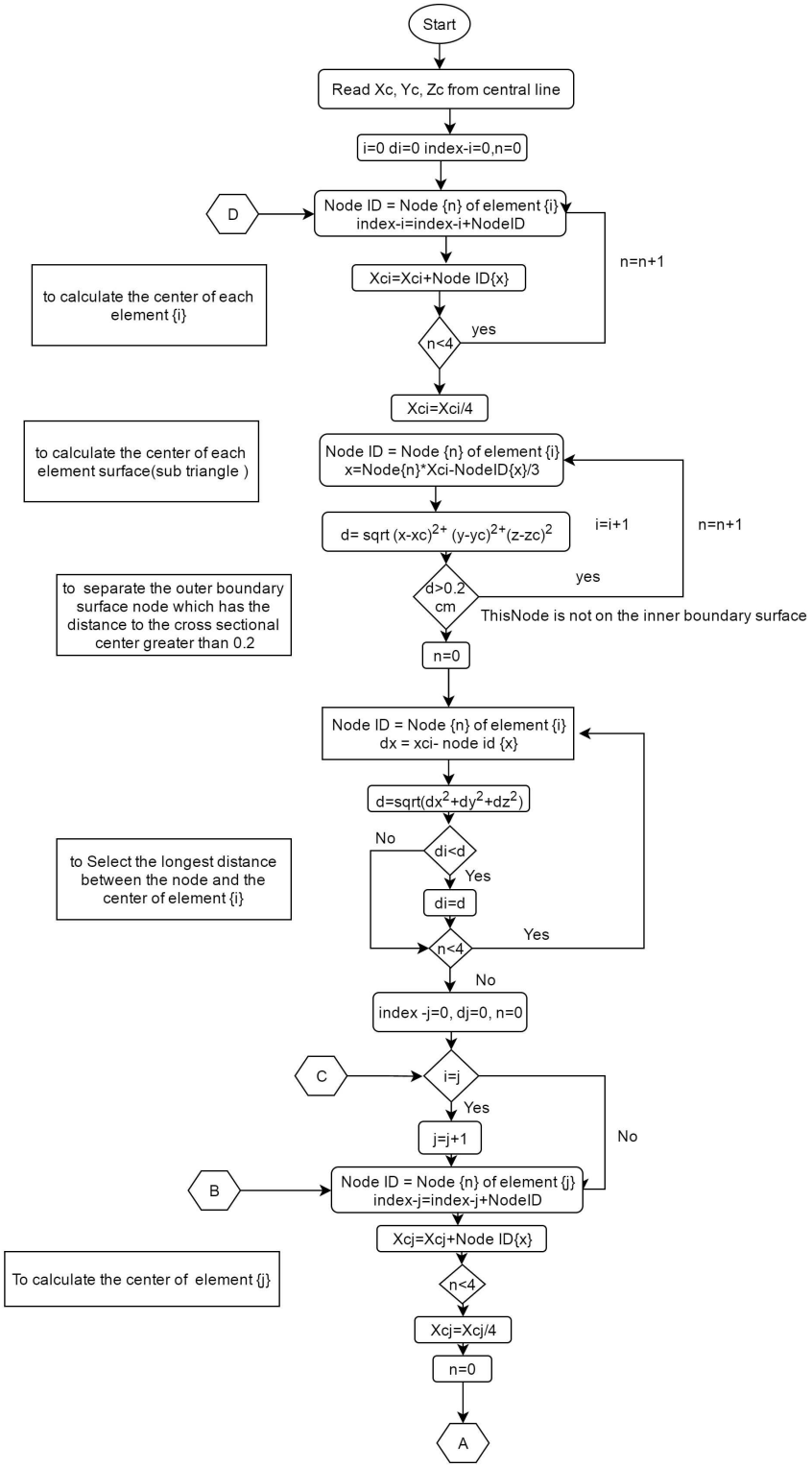

Figure 4.14: The algorithm flowchart developed to select the IB points (I).

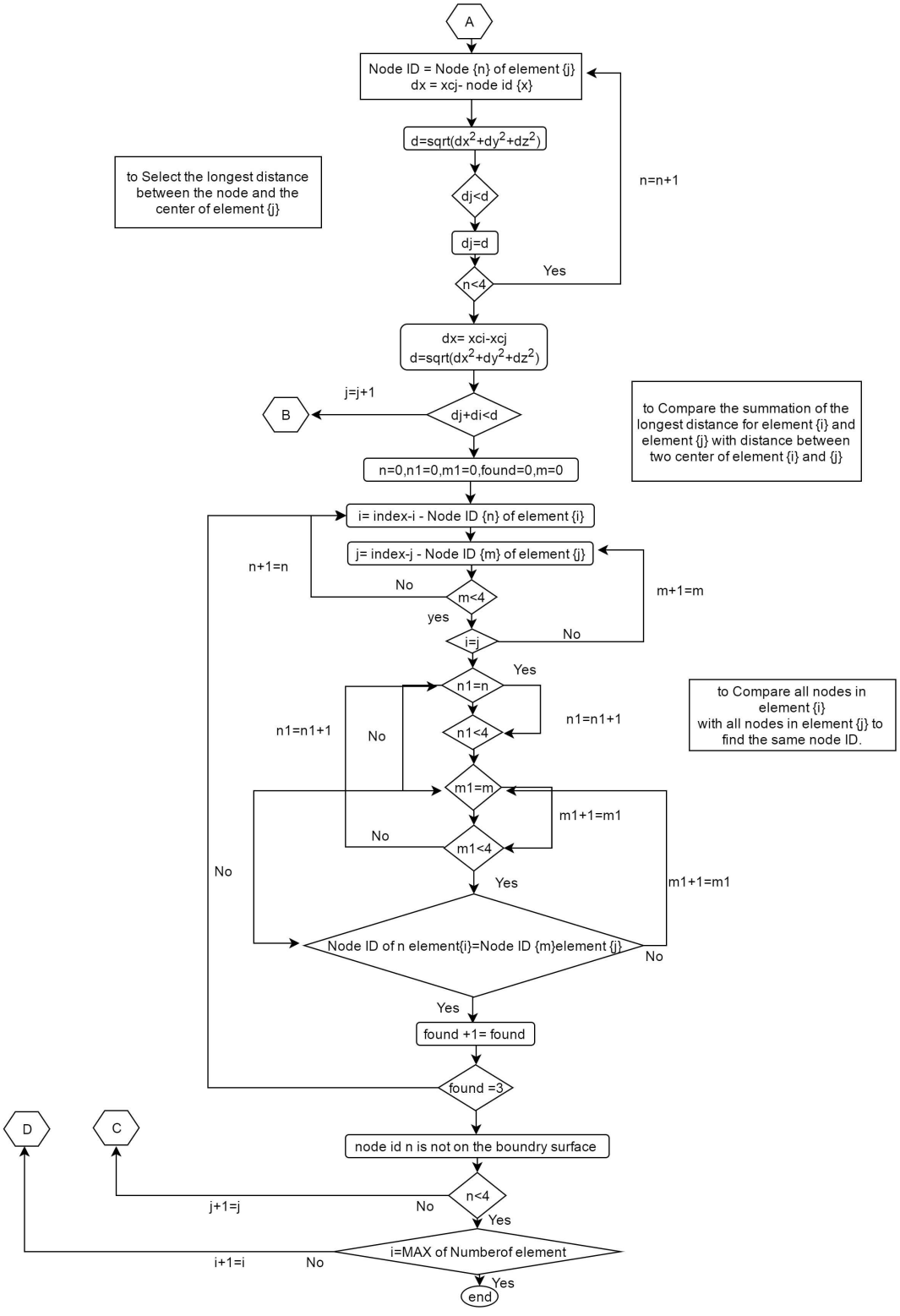

Figure 4.15: The algorithm flowchart developed to select the IB points (II).

4.4 Summary

This chapter has described the mesh generation analysis for the solid, fluid and immersed boundary parts of the 3D ureter model. Considering the limited computational resources available at QMUL, a wide range of fluid and solid grid resolutions have been examined to obtain an optimised resolution which can provide the most accurate computational results possible. For the solid part (ureter), mesh 4 was selected and for the fluid part (urine) Domain 4 were selected. For each mesh type, a mesh independent study was performed to ensure that the use of coarser mesh elements would not cause inaccuracy in the computational results. To further improve the computational performance, the fluid domain was shrunk by removing the unused blocks. An algorithm was developed with the purpose of creating immersed boundary points between the fluid and the solid parts. Finally a series of C programming codes were developed and introduced into the main codes in order to initialise the 3D model of the ureter to be compatible with the structural code.

Chapter 5

Peristalsis modeling estimation based on Numerical Simulations.

5.1 Motivation

The aim of this chapter is to report firstly, on the simulation of ureteralperistaltic contraction by considering the Intra-Abdominal Pressure (IAP) and secondly, to investigate the effect of ureteral wall contraction on the pressure pulse magnitude and finally, to validate the computational results against other experimental studies. In order to reproduce the pressure/time graph, an approximation of the contact pressure between the solid walls resulting from contact forces acting on cross-sectional nodes of the computational model was obtained. Two separate contraction models were investigated in order to find the most precise results: one with a constant radial force and the second one, an improved version obtained by adding a specific time-window with the purpose of muscle contraction in time and location.

5.2 Ureteral Pressure estimation on Numerical Simulations

An accurate determination of pressure is significantly important in understanding the ureteral function. Most of intra-ureteral pressure profile studies have been investigated by using the fluid-filled catheters connected to displacement type pressure transducers [81]. It is evident that pressure measurements highly rely on the movement of urine in and out of a transducer chamber. In an actual situation, the highest pressure occurs in the contraction area when the ureter collapses completely around the tip of fluid filled catheter.

By using of a stationary probe with an opening parallel to urine flow (inside the ureteral wall), an approximate static pressure can be measured. The dynamic pressure can also be estimated in the ureter, if the opening in the probe is placed normal to the direction of urine flow. The low velocity of urine makes the dynamic pressure contribution less than 1% of the total pressure. So, in the absence of a peristaltic contraction, the total pressure measured by a pressure transducer will be mainly static pressure which can be interpreted as the resting pressure in the ureter.

The effect of pressure transducer/catheter on pressure recordings in the ureter has been discussed widely in other studies [82]. According to a study by Kiil et al. [17], the catheter did not cause any urine retention; thereby no ureteric function disturbance was observed and hence the pressuretime recording was not sensitive to the catheter.

In a healthy ureter, the resting pressure is around 4-7 mmHg and a peak pressure is around 24-26 mmHg with a corresponding amplitude of 15 mmHg for a pulse which takes around 2-3 seconds. The UreteroVesical Junction (UVJ) performs as a check valve through which urine can be discharged into the bladder when the pressure in the ureter is higher than the vesical (bladder) pressure. Each urine spurt enters into the bladder when a peristaltic wave arrives in UVJ. The resting pressure is the same before and after each wave. The net pressure rise

due to the movement of the wave is zero.

Moreover, as long as the vesical pressure does not exceed 25-29 mmHg, the resting pressure is unaffected and remains at the same level. Figure 5.1 shows a schematic diagram of the pressure distribution in a ureter. Pressure pulse measurement in the ureter is one of the main tools to investigate peristaltic activities. These recording can provide useful information about the frequency, periodic cycle, interrelation and the velocity of the contraction along the ureter. Moreover, the magnitude and the feature of the pressure waveform generated by peristaltic movement in a ureter can be investigated through experimental pressure pulse recordings. The physical significance of each individual pressure pulse, consisting of the static and dynamic function of the ureter, has not been investigated.

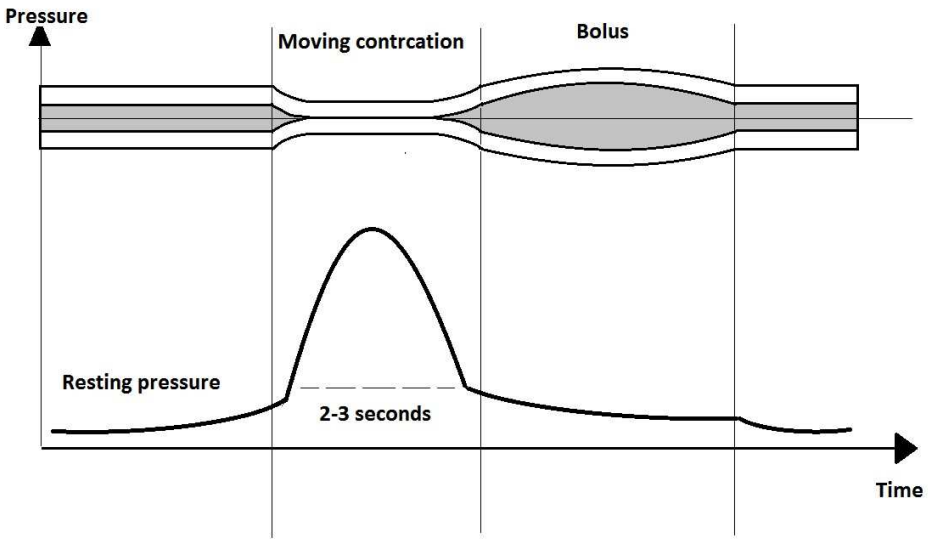

Figure 5.1: Schematic diagram of pressure distribution in the ureter.

In a peristaltic contraction, the maximum pressure occurs during the contraction phase and that leads to a complete closure of the cross-sectional area (lumen), thus zero fluid pressure is expected. This is because there will not be any fluid inside the closed lumen and thus the total present forces are only as a

result of contact forces generated between the ureteral walls. In the absence of the catheter, the muscle contraction closes the cross sectional area completely, so the pressure distribution over time is only a function of the muscle action.

The aim of this chapter is to report firstly, on the simulation of ureteral peristaltic contraction by considering the intra-abdominal pressure; secondly, to investigate the effect of ureteral wall contraction on the pressure pulse magnitude and finally, to validate the computational results against published experimental studies [81, 82].

The ureteral peristaltic motions forming due to consecutive contractions and relaxations of the circular and longitudinal smooth muscle layers, results in a complete closure of the lumen. However, for this study only the radial contractions of circular muscle were modelled and the longitudinal contractions of the smooth muscle will be investigated in future study.

5.3 Contraction Modelling

The ureteral peristaltic contraction was simulated by integrating two separate contraction models in order to find which provides the most precise results. One model implemented a constant radial force acting on the cross-sectional area which travels axially along the ureter model with the same speed as the actual human ureter contraction. The second model uses an individual time-window frame for each cross-section along the ureter with the purpose of emulating the relaxation and contraction of individual muscles with fixed positions across time. Both contraction models used the same set of parameters from clinical studies [40, 17] as presented in Table 5.1.

Table 5.1: Joint parameters used in both contraction models.

Velocity of contraction (cm/s)	Force magnitude (Dyne)	Contraction length (cm)
3.5	1200	3

5.3.1 Peristaltic Motion as a Constant Force

To simulate the contraction using a constant radial force, a specific time-window was defined at the beginning of the ureter. This specific time-window travels along the ureter longitudinal direction with a velocity of 3.5 cm/s similar to the clinical data [6]. The force was applied to close the lumen in order to push the urine down the ureter with the purpose of mimicking realistic pacemaker activity. A maximum force of 1200 dynes was applied radially on the ureter to mimic contraction. A window of 3 cm of contraction travelled with the speed of 3.5 cm/s along the length of the tube. The maximum force is calculated according to Eq 5.1.

$$Force_{max} = \frac{Pressure_{max}}{A} \tag{5.1}$$

where A is the area $= \frac{2\pi rL}{n}$, and n is the maximum number of nodes in the time window.

The time-window with initial position Z_1 is updated for each time step. All nodes with Z coordinate between Z < Z_1 and Z > Z_1-L, where L is contraction length, will have a maximum constant force as shown in the following steps:

- Step 1) For each cross section the centre coordinate is calculated according to the initial coordinate of all nodes,

$$X_c = \frac{\sum_0^{maxN} x_{initial}}{maxN}, \tag{5.2}$$

$$Y_c = \frac{\sum_0^{maxN} y_{initial}}{maxN} \tag{5.3}$$

$$Z_c = \frac{\sum_0^{maxN} z_{initial}}{maxN} \tag{5.4}$$

where Max N which is the maximum number of nodes in each cross section.

- Step 2) The distance between the centre and the current coordinate is calculated as follows:

$$dis = \sqrt{(X_C - X_{C_{current}})^2 + (Y_C - Y_{C_{current}})^2 + (Z_C - Z_{C_{current}})^2} \quad (5.5)$$

- Step 3) The normal vectors are calculated :

$$n_x = \frac{X_{current} - X_{C_{current}}}{dis}, \quad (5.6)$$

$$n_y = \frac{Y_{current} - Y_{C_{current}}}{dis} \quad (5.7)$$

$$n_z = \frac{Z_{current} - Z_{C_{current}}}{dis} \quad (5.8)$$

- Step 4) The force vector is calculated as a product of the magnitude of the force and normal vectors:

$$\overrightarrow{f_x} = (Force)\overrightarrow{n_x} \quad (5.9)$$

$$\overrightarrow{f_y} = (Force)\overrightarrow{n_y} \quad (5.10)$$

$$\overrightarrow{f_z} = (Force)\overrightarrow{n_z} \quad (5.11)$$

5.3.2 Peristaltic Motion as a Piecewise Linear Force

In this section, the peristalsis movement is modelled as a piecewise linear function which can be seen in Eq 5.15. A time-window, as shown in Figure 5.1, indicates that each cross-section of the ureter has an individual time-window in order to

be exposed to a linear force and this time-window is dependent on the current time.

It is worth mentioning that, because each section is allocated assigned an individual time-window with a time span of 2 to 3 sec, the force is applied to the section when the current time reaches a particular time window.

In Figure 5.2, n is the beginning time of the contraction and m is the total number of sections of the contraction. The other two main variables are defined as S and T where S is defined as the time that a contraction is required to transfer from one cross-section to another cross-section of the ureter. T is the time at the beginning of the window for each cross-section. The steps need to be taken the force on a cross-section are presented below:

- Step 1) Calculates the centre of cross section regarding the current coordinate of each node ID on the same cross-section

$$X_{C_{current}} = \frac{\sum_0^{maxN} x_{C_{current}}}{maxN} \tag{5.12}$$

$$Y_{C_{current}} = \frac{\sum_0^{maxN} y_{C_{current}}}{maxN} \tag{5.13}$$

$$Z_{C_{current}} = \frac{\sum_0^{maxN} z_{C_{current}}}{maxN} \tag{5.14}$$

- Step 2) The function contraction model which shows the force acting on each cross section is defined as:

$$F(t) = \begin{cases} \frac{F_{max}}{s}t, & 0 < t < s \\ F_{max}, & s < t < (m-1)s \\ \frac{F_{max}}{s}(ms - t), & ms < t < (m-1)s \end{cases} \tag{5.15}$$

Windows Time		
Section Number	Begin	End
N	(-m)s	0
n-1	(-m+1)s	1s
n-2	(-m+2)s	2s
n-m	0	ms
1	(-m+n-1)s	(n-1)s

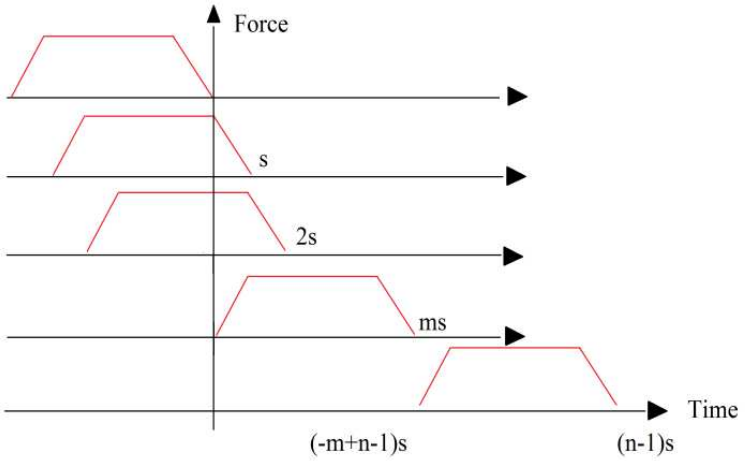

Figure 5.2: The time window of each cross section experiences the contraction.

- Step 3) The distance between the current coordinate of each node and the current centre of each cross section is calculated as:

$$dis = \sqrt{(X_{current} - X_{C_{initial}})^2 + (Y_{current} - Y_{C_{initial}})^2 + (Z_{current} - Z_{C_{initial}})^2} \tag{5.16}$$

- Step 4) The normal vector between these centres is calculated by using the estimated distance from step 3:

$$n_x = \frac{X_{current} - X_{C_{current}}}{dis} \tag{5.17}$$

$$n_y = \frac{Y_{current} - Y_{C_{current}}}{dis} \tag{5.18}$$

$$n_z = \frac{Z_{current} - Z_{C_{current}}}{dis} \tag{5.19}$$

- Step 5) The force components are calculated as:

$$\overrightarrow{f_x} = (Force)\overrightarrow{n_x}, \tag{5.20}$$

$$\overrightarrow{f_y} = (Force)\overrightarrow{n_y} \tag{5.21}$$

$$\overrightarrow{f_z} = (Force)\overrightarrow{n_z} \tag{5.22}$$

- Step 6) The resultant force in x,y,z directions is calculated for each individual cross-section:

$$\overrightarrow{F_{X_{results}}} = \overrightarrow{F_{X_{results}}} + \overrightarrow{f_x}, \tag{5.23}$$

$$\overrightarrow{F_{Y_{results}}} = \overrightarrow{F_{Y_{results}}} + \overrightarrow{f_y}, \tag{5.24}$$

$$\overrightarrow{F_{Z_{results}}} = \overrightarrow{F_{Z_{results}}} + \overrightarrow{f_z}, \tag{5.25}$$

- Step 7) The force to each node on each cross section is applied as:

$$\overrightarrow{F_{X_{final}}} = \frac{\overrightarrow{Force_{X_{final}}} + \overrightarrow{f_x} + \overrightarrow{F_{X_{result}}}}{\sum Nodes} \tag{5.26}$$

$$\overrightarrow{F_{Y_{final}}} = \frac{\overrightarrow{Force_{Y_{final}}} + \overrightarrow{f_y} + \overrightarrow{F_{Y_{result}}}}{\sum Nodes} \tag{5.27}$$

$$\overrightarrow{F_{Z_{final}}} = \frac{\overrightarrow{Force_{Z_{final}}} + \overrightarrow{f_z} + \overrightarrow{F_{Z_{result}}}}{\sum Nodes} \tag{5.28}$$

5.4 Intra-Abdominal Pressure (IAP) modelling

The ureter is surrounded by connective tissue which makes the ureter remained in horizontal position. Intra-Abdominal Pressure (IAP) is the pressure within the abdominal cavity which varies between 5 and 7 mmHg in men and is the same as the resting pressure [6]. In the present study, in order to keep the ureter in a horizontal position, an IAP model was introduced to the Y-code. A detailed descriptions of the algorithm is presented in a sequential order from step 1 to 5 as follows:

- Step 1) The centre of each cross-section is calculated with regard to the initial coordinates of each nodes ID on the same cross-section where max N is the maximum number of nodes in each cross section.

$$Y_{C_{initial}} = \frac{\sum_0^{maxN} y_{C_{initial}}}{maxN} \tag{5.29}$$

$$Z_{C_{initial}} = \frac{\sum_0^{maxN} z_{C_{initial}}}{maxN} \tag{5.30}$$

- Step 2) The centre of each cross-section with regard to the current coordinates of each nodes ID on the same cross-section is calculated as:

$$X_{C_{current}} = \frac{\sum_0^{maxN} x_{C_{current}}}{maxN} \tag{5.31}$$

$$Y_{C_{current}} = \frac{\sum_0^{maxN} y_{C_{current}}}{maxN} \tag{5.32}$$

$$Z_{C_{current}} = \frac{\sum_0^{maxN} z_{C_{current}}}{maxN} \tag{5.33}$$

- Step 3) The distance between the initial centre and current centre of each

cross-section is calculated as:

$$dis = \sqrt{(X_{current} - X_{C_{initial}})^2 + (Y_{current} - Y_{C_{initial}})^2 + (Z_{current} - Z_{C_{initial}})^2} \tag{5.34}$$

- Step 4) The normal vector between these two centres is calculated by using the estimated distance from step 3.

$$n_x = \frac{X_{C_{initial}} - X_{C_{current}}}{dis}, \tag{5.35}$$

$$n_y = \frac{Y_{C_{initial}} - Y_{C_{current}}}{dis}, \tag{5.36}$$

$$n_z = \frac{Z_{C_{initial}} - Z_{C_{current}}}{dis} \tag{5.37}$$

- Step 5) The force vector components is calculated as:

$$\overrightarrow{f_x} = Force(\overrightarrow{n_x}.dis), \tag{5.38}$$

$$\overrightarrow{f_y} = Force(\overrightarrow{n_y}.dis), \tag{5.39}$$

$$\overrightarrow{f_z} = Force(\overrightarrow{n_z}.dis) \tag{5.40}$$

This force is applied to all nodes along the ureter model at each time step by keeping the current coordinates of the centre of each cross-section in a manner similar to initial coordinates of centre of each cross-section during the contraction. The resting pressure, similar to the IAP, is around 3-8 mmHg The magnitude of Force in step 4 is obtained from the following calculation where r is the radius of ureter, L is length of ureter, N= number

of surface nodes in the computational model.

$$Force = Pressure_{resting} \times Area \tag{5.41}$$

where Area=$\frac{2\pi rL}{N}$=$\frac{2\times\pi\times0.25\times21}{1302}$=0.025 cm^2

$Force = 4000 \times 0.025 = 100\ dynes$

5.5 Results and Discussion

In this section, firstly the computational results on the effect of IAP on the ureteral wall deformation will be discussed. Secondly, the computational results from the two contraction models, constant force and piecewise linear force, will be presented.

5.5.1 Comparison between the contraction models with and without IAP

Figure 5.3(a-b) shows a comparison between the two computational models of the peristaltic movement in the presence and absence of the IAP.

Figure 5.3(a) shows that with the absence of the IAP the ureter model is not constrained and start moving in an eccentric direction. Figure 5.3(b) shows that with the presence of the IAP, the ureter model is fully constrained and the applied radial force leads to a centric contraction, similar to an actual human ureter.

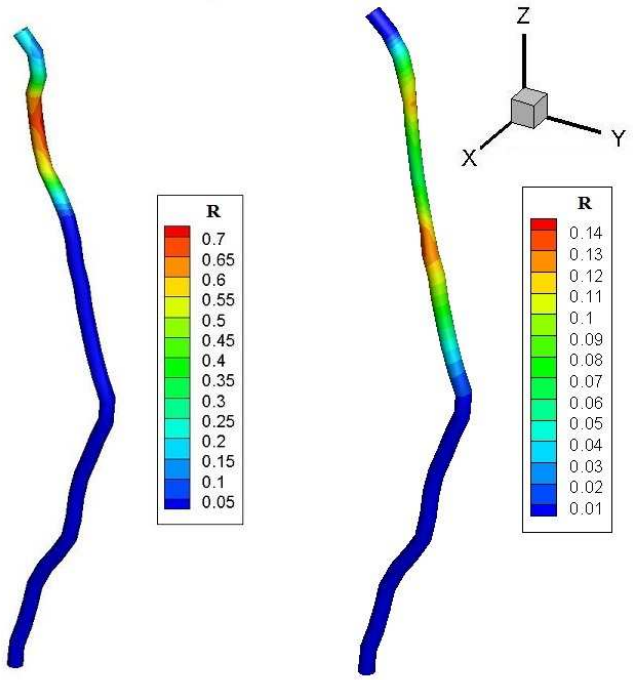

Figure 5.3: Comparison between the two simulations in the absence (a) and in the presence (b) of the IAP

5.5.2 Comparison between the Models with Constant and Linear Force

A length of contraction of 4cm and the maximum force of 1200 dynes were applied. A constant intra-abdominal force of around 100 dynes was applied to maintain the ureter in a horizontal position. The contact wall pressure on an arbitrary point located around the middle of the ureter is computed and results are plotted for both models with a constant force and linear force. Figure 5.4 shows non-filtered results of contact pressure during the passing of a complete contraction as a result of applying the constant force model. Figure 5.5 shows non-filtered results of contact pressure during the passing of a complete contraction as a result of applying the linear force model.

Figure 5.6 shows the filtered computational results of pressure against time for the constant force and linear force models, in comparison with the experi-

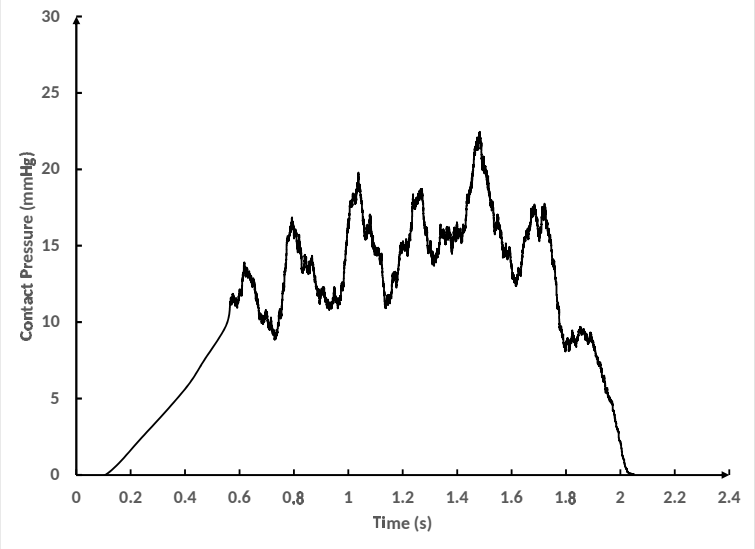

Figure 5.4: Non-filtered results of contact force model for an arbitrary point in the middle of the ureter during passing of a complete peristalsis movement.

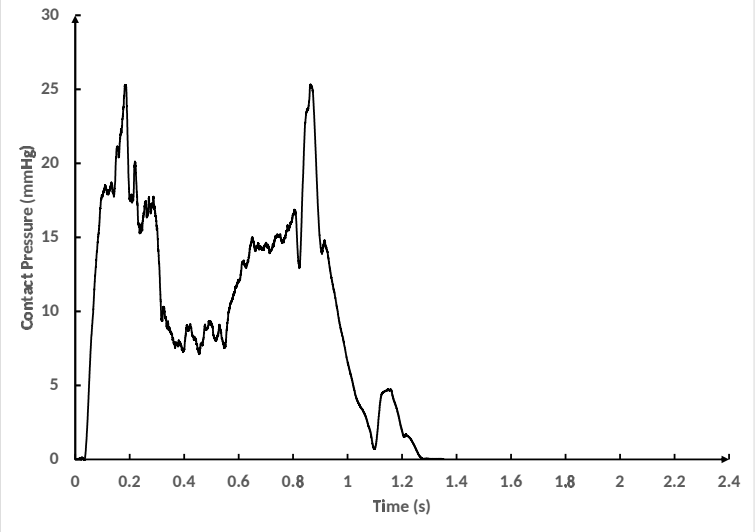

Figure 5.5: Non-filtered results of contact force for an arbitrary point in the middle of the ureter during passing of a complete peristalsis movement.

mental study by Kill et al. [17]. The data was filtered using the SavitzkyGolay filtration method. The maximum contact pressure is obtained by dividing the contact forces by area for each element. Figure 5.6 shows a similar amplitude of 20 mmHg for both computational and experimental data. It is evident that

the results from the piecewise linear function shows a better match with the experimental study [17]. The pulse duration, shown in this figure, is the time when the contact pressure increases to its maximum value and then gradually drops as the contraction travels away. It can be seen that the pulse duration for the linear force model is about 2.3 seconds and for the constant force is about 1.25 second. It is concluded that the linear force model exhibits a better performance. Figure 5.7 shows the deformation of a cross-section over the same period of the contraction time. R is defined as the radius displacement of the ureter in cm. This figure confirms the complete closure of the ureteral cross-section, where maximum pulse pressure occurs.

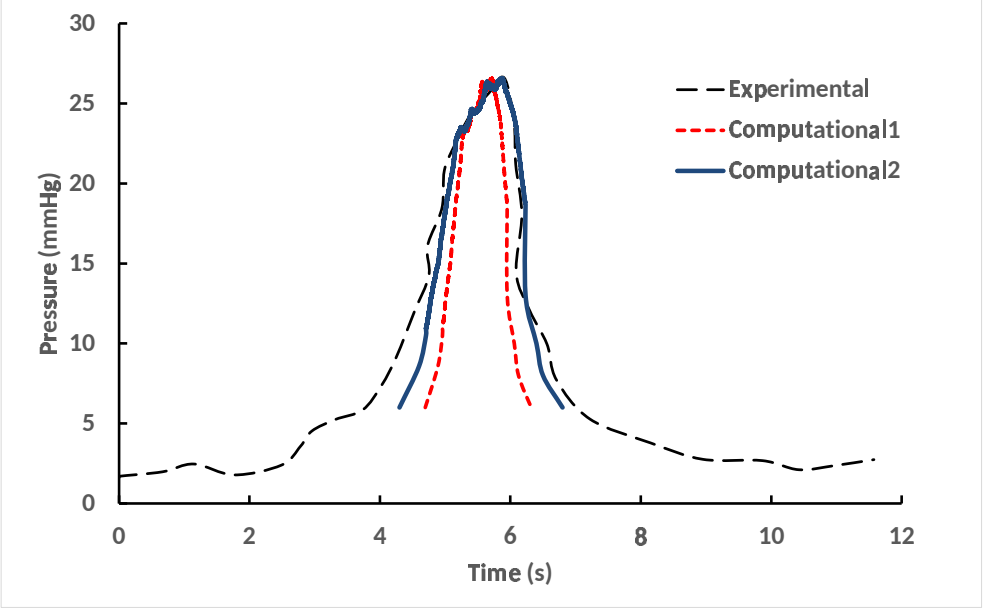

Figure 5.6: The filtered computational results of pressure over time with a constant force model (Computational 1) and the linear force model (Computational 2), compared with the experimental study by Kill et al. [17].

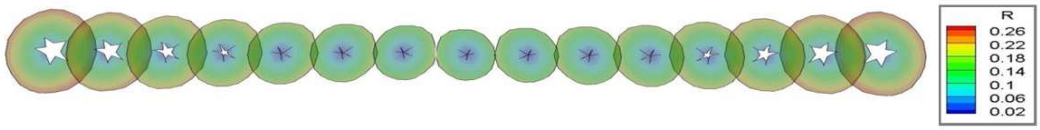

Figure 5.7: The deformation of a cross-section over the same period of the contraction time, where R is the radius of the cross-section in cm.

Figure 5.8 (a-d) shows four consecutive time sequence plots of the ureteral contraction travelling along the longitudinal direction. In this figure P is the radial displacement resulting from peristaltic contraction. The maximum deformation of the outer surface in a radial direction is around 0.1 cm.

During the contraction phase, the ureteral diameter reduces up to 60% of the maximal diameter during resting phase [83]. As shown in Figure 5.7, the maximum radial displacement of the outer surface during the contraction phase is around 0.1 cm which makes the outer diameter of around 0.2 cm which is in a close agreement with experimental study [83].

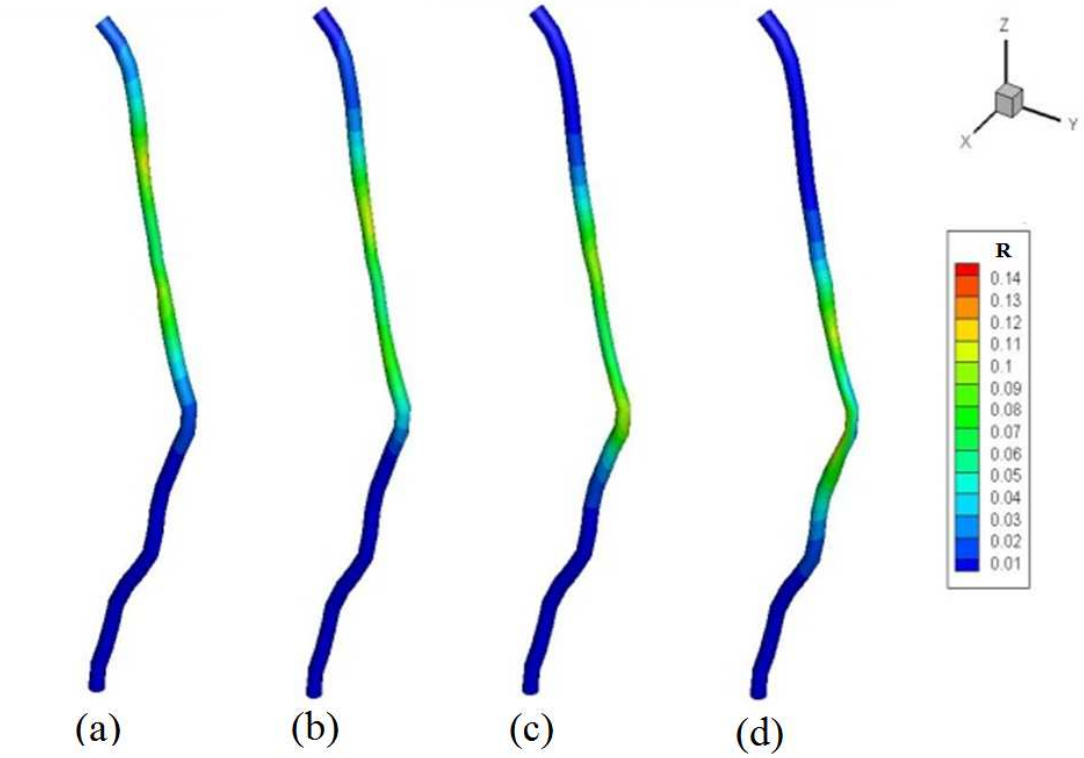

Figure 5.8: The movement of the contraction at T= 0.5 ,1 ,1.5 and 2.5 seconds (a-d).

5.6 Summary

In this chapter, an intra-abdominal pressure model is introduced into the Y-code for the purpose of constraining the ureter position. Two types of force models were tested in order to mimic a realistic peristalsis movement. Results from using a piecewise linear force were in very good agreement with experimental studies in terms of maximum magnitude and pulse duration.The deformation of the ureter surface of the ureter is in the range of experimental studies.

Chapter 6

An Investigation in Healthy and non-Healthy Ureter

6.1 Motivation

In Chapter 5, a realistic 3D model of peristaltic contraction travelling in a longitudinal direction was presented. This model accurately mimics the cell to cell peristaltic movement of a ureteral wall.

The dynamics of the upper urinary tract and the effect of bladder pressure variation on urodynamic parameters have been studied by other researchers [84, 16]. However, there are many urodynamic phenomena that have still not been fully explained. For instance, explaining the mechanism behind (ureteral) reflux is one of the biggest challenges in urodynamic research. The interaction between the kidney pressure and bladder pressure has been described in very few analytical or computational simulations.

In this chapter firstly, the effect of linear and nonlinear tensile properties on urine bolus velocity will be discussed. Next, two types of ureteral abnormalities known as Dysfunctional Pelvis Ureteric Junction (PUJ) and inefficient peristaltalsis will be simulated by implementing different boundary conditions. The urodynamic responses as well as the effect on ureteral wall shear stress level will be analysed under these conditions. Particularly, the presence of reflux in the absence of a pressure difference and the effects of dysfunctional PUJs will be investigated. Furthermore, the efficiency of peristaltic contraction will be evaluated by studying the relationship between contraction amplitude and backflow. The results from this chapter will assist medics to understand the impaired ureteral function in more detail.

6.2 Simulation Setup and Configuration

For this study the following configurations were specified.

- **Urine properties**: Urine is an incompressible laminar, Newtonian fluid with dynamic viscosity of 0.01 poise and a constant density of 1 g/cm3. The initial velocity of urine was set to 0.01 cm/s.
- **Material properties of the ureter**: Linear and nonlinear tensile properties are modelled for the ureter wall. For the linear material the Young's modulus is assumed 5 Kpa and for the nonlinear material the stress-strain curve from Yin etals study [43] was adopted and incorporated in the Y-code. The $Poisson$s ratio of the ureter wall is 0.35 for all simulations in this chapter.
- **Contraction model**: The simulation of normal contractions in the ureter was conducted by describing two pacemaker activities in the ureter model referred to as contraction A and contraction B. Contraction A is located in the proximal part of the ureter and Contraction B is located in the distal part. Figure 6.1 shows the location of the two contractions A and B in the ureter. Two contraction models are used in the simulation is to

accurately model the pacemaker activities in different parts of the native ureter. In an actual ureter the pacemaker cells are located along the ureter and they initiate the contraction [6]. In this study, to simulate a normal and depressed ureteral contraction, a force of 1200 and a relatively low force of 450 dynes is applied in the model. The low force contraction prevents a complete closure of the lumen area as a consequence of taking vasodilators. Since, vasodilators resulting in a significant reduction in ureteral contraction pressure of between 20 to 65%, the magnitude of contraction force of 450 dynes is considered to model the simulation [33].

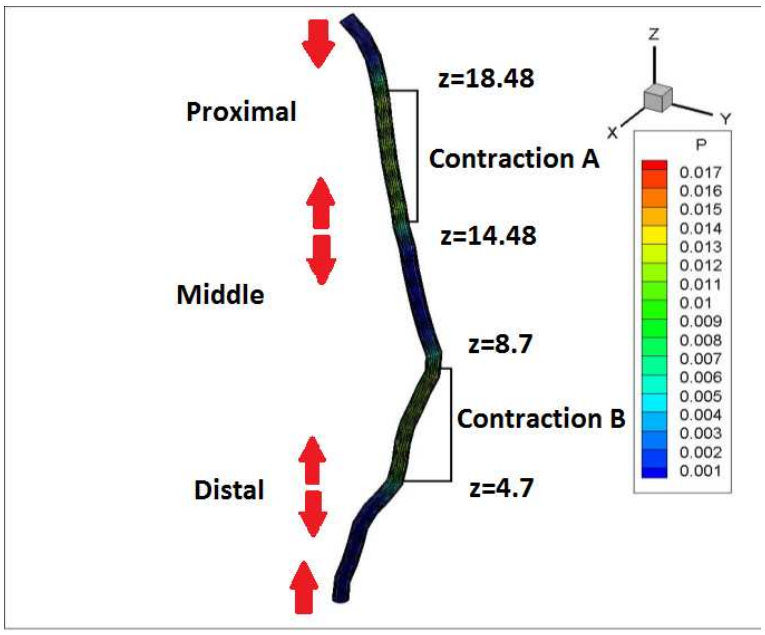

Figure 6.1: Contraction A and B in the proximal and distal part of the ureter.

- **Boundary conditions**: A no slip boundary condition is applied between the urine and ureter wall. Different pressure differences (ΔP) are applied between the inlet and outlet of the ureter in order to simulate the healthy condition and dysfunctional PUJ. For a healthy ureter, according the study by Shafik [40], the pressure difference between the resting pressure in the PUJ and the resting pressure in the UreteroVesical Junction (UVJ) is between 0.36 and 0.73 mmHg. A pressure difference of 0.4 mmHg is applied in order to simulate the healthy ureter in this work. For dysfunctional

PUJ, no resting pressure difference is described between the renal pelvis and PUJ. This is because the renal pelvis has the same resting pressure as UVJ [40], so there is no pressure difference between the resting pressure in the PUJ and in the UVJ.

Table 6.1: The boundary conditions, contraction parameters and material properties of the four simulations performed in this work

Simulation	Condition	Material Properties	Velocity of Contractions	ΔP	Contraction Force
1	Dysfunctional PUJ	Nonlinear	3.5,1.75 (cm/s)	0 (mmHg)	1200 (dyne)
2	Normal	Nonlinear	3.5,1.75 (cm/s)	0.4 (mmHg)	1200 (dyne)
3	Normal	Linear	3.5,3.5 (cm/s)	0.4 (mmHg)	1200 (dyne)
4	Effect of drug	Nonlinear	3.5,3.5 (cm/s)	0 (mmHg)	200 (dyne)

6.3 Investigation on the Effect of Linear and Non-linear Ureter Wall Tensile properties on Urine Velocity in a Healthy Ureter

In this section, the effect of linear and nonlinear tensile properties on urine bolus velocity in a healthy ureter is studied. Two contractions move longitudinally along the ureter with a velocity of 3.5 cm/s. Figure 6.2(a,b) show the magnitude of the urine velocity in Z-direction in the bolus using nonlinear (a) and linear (b) material properties.

Figure 6.2(b) shows that the maximum urine velocity in the longitudinal direction is slightly higher when using a wall with linear tensile properties. In order to have a better understanding of the bolus velocity, the average velocity is calculated using an equation for the velocity profile for laminar flow in a pipe [85];

$$U_r = 2U_{avg}[1 - \frac{r^2}{R^2}] \tag{6.1}$$

Where U is velocity, r is the point radius from the centre and R is radius of

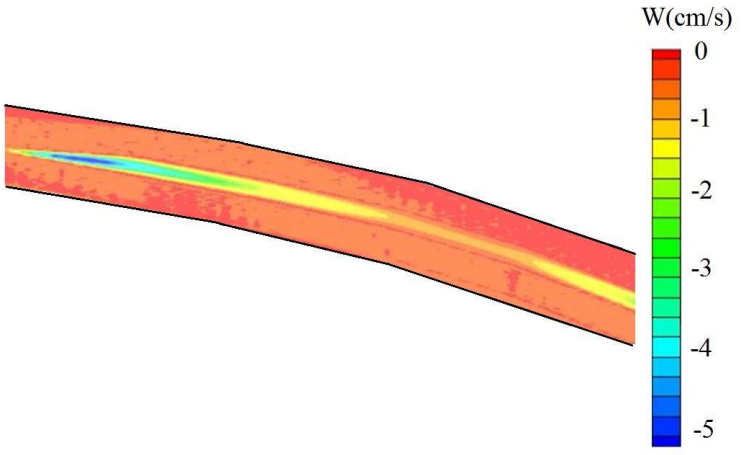

(a)

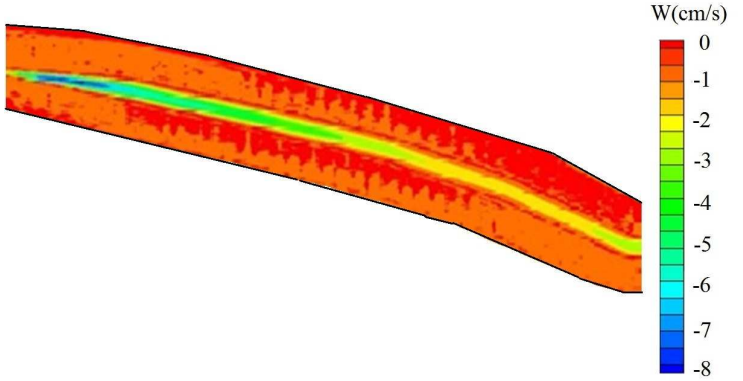

(b)

Figure 6.2: The magnitude of urine velocity in the Z-direction. (a) Bolus between the two contractions with non-linear material properties. (b) Bolus between the two contractions with linear material properties.

the pipe. The maximum velocity occurs at the centreline where r=0 and can be extracted easily from the simulation. The average velocity is therefore calculated as:

$$U_{avg} = \frac{U_{max}}{2} \tag{6.2}$$

The average urine velocity with nonlinear and linear tensile properties for the ureteral wall are plotted in Figure 6.3. For the non-linear material model, the

average velocity in the bolus is around 3.5 cm/s, similar to the speed of the contraction movement. The model using linear tensile properties shows higher average urine velocity due to the large deformation of the ureteral wall during the contraction. The linear tensile model overestimates the ureteral wall deformation during the contraction and expansion of the lumen. This causes a higher average-velocity in the centre of the ureteral lumen. Yet, the nonlinear material model of ureteral wall has shown to be more realistic.

As the average urine velocity traveling in vicinity of the contraction is the same as the velocity of the contraction itself in a healthy ureter [17, 40], it can be concluded that the use of non-linear tensile properties model showed a better agreement to what is occurring in a native system.

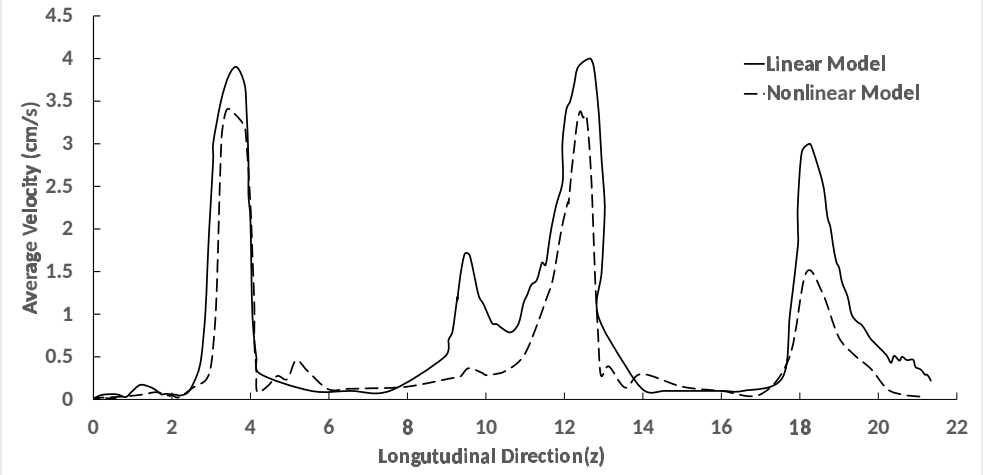

Figure 6.3: Comparison between the average velocity of urine in the ureter using models with linear and nonlinear tensile properties (T=1 second).

6.4 The Urodynamic Responses in Healthy and Pathological Conditions

6.4.1 Ureteral Wall Shear Stress Distribution

The study of shear stress and consequent shear strain of biological tissue is important because excessive shear strain can deform the cell wall, interfere with biological functions and in some cases cause tissue damage.

In this section, the wall shear stress distribution of the ureteral wall are studied under both the presence and the absence of a pressure difference, mimicking the healthy and pathological conditions respectively. Contractions A and B travel with a velocity of 3.5 cm/s and 1.75 cm/s respectively. A pressure difference of 0.4 mmHg is applied in order to simulate the healthy condition.

Figure 6.4 shows the wall shear stress at T=0.3, 0.6, 1.0 seconds in the absence of the pressure difference and Figure 6.5 show the wall shear stress at T=0.3, 0.6, 1.0 seconds in the presence of the pressure difference.

The results from both simulations show that the shear stress is significantly higher around the contraction region. It is clear that highest shear stress occurs at the proximal part of the ureter, in the vicinity of the PUJ. The figure also shows that the maximum value of shear stress decreases as the peristalsis propagates towards the UVJ.

The results show that the maximum shear stress on the wall is dependent on the velocity of the contraction in the ureter. The shear stress behind the contraction B is 75% lower than that around contraction A due to its lower peristaltic velocity.

These results show that the proximal part of ureter, in the vicinity of the PUJ, can be subjected to high shear stress and may result in wall deformation in that region. The occurrence of high shear stress at the proximal part of ureter described by this study supports other computational [54] and experimental stud-

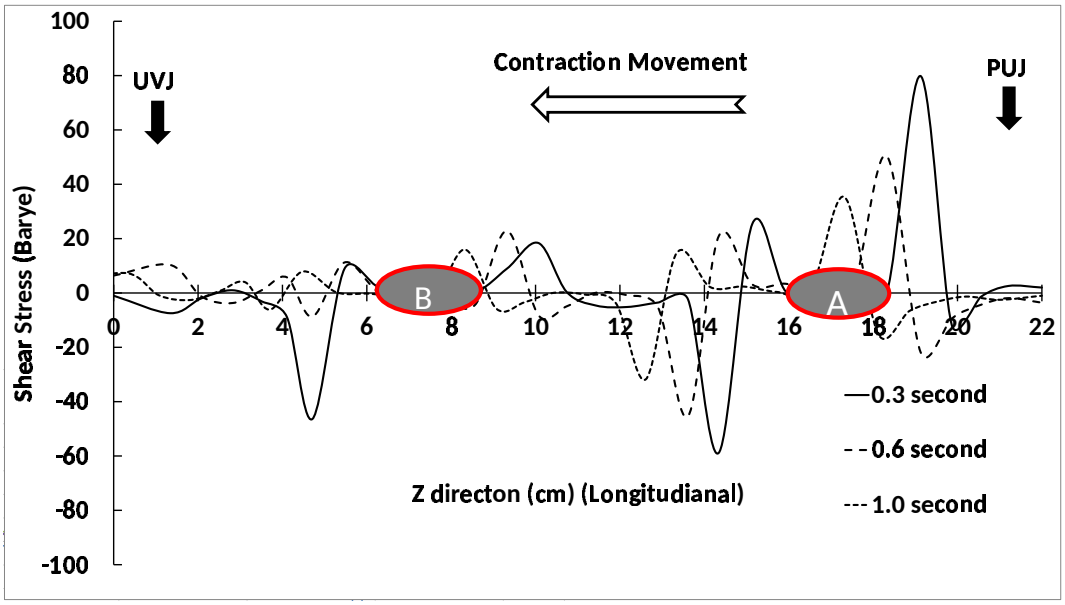

Figure 6.4: Wall shear stress in the absence of the pressure difference (Dysfunctional PUJ). The positions of contractions A and B are shown.

ies [27, 28] in which the possibility of wall deformation and consequent proximal ureter rupture was reported. Proximal ureter rupture is a perforation of the ureter which causes a series of problems such as infection and renal impairment.

There is a 25% drop in the maximum shear stress between the simulations in which a pressure difference of 0 and 0.4 mmHg were applied across the ureter. These results also indicate the importance of the presence of the PUJ in the urinary system which maintains the pressure difference in the ureter, thereby decreasing the shear stresses level on the proximal part of ureter.

6.4.2 Reflux

Next in this study, the possibility of the reflux formation in a dysfunctional PUJ condition was investigated. In urodynamics , the reflux phenomenon is an interesting subject, since one of the most common disease in urinary system is the presence of the Urinary Tract Infection (UTI) due to the reflux carrying the bactria into the kidney.

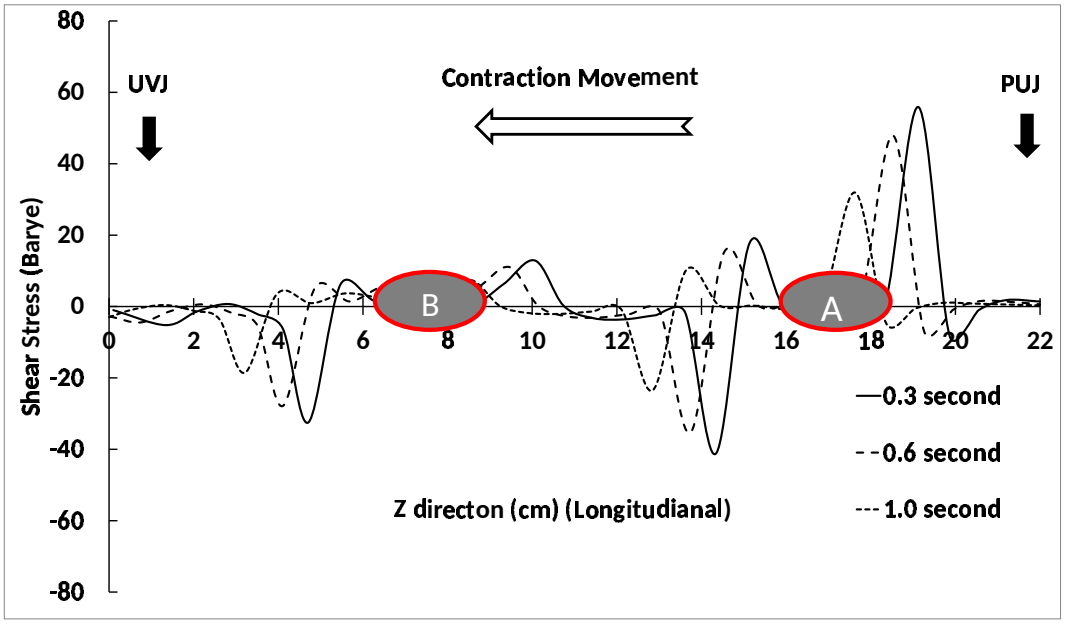

Figure 6.5: wall shear stress in the presence of the pressure difference of 0.4mmHg(healthy). The positions of contractions A and B are shown.

To investigate the reflux, both contractions A and B are set to travel with the same speed of 3.5 cm/s. There is a pressure difference of zero between the inlet and outlet. Figure 6.6(a,b) shows the urine velocity vectors behind the moving contraction A and B respectively after 0.5 seconds. The figures show a high backward velocity, confirming the occurrence of reflux behind both contractions A and B.

The proximal part of the ureter and the pelvic spindle are more likely to be sites of urine reflux. These results also indicate the importance of the presence of PUJ in the urinary system which prevents any reflux into the renal pelvis from the ureter. These wall shear and velocity vector investigations have shown that the high shear stress and reflux usually occurs at the beginning of the closing the lumen at the start of the simulation time.Both phenomena are gradually decrease by propagation of the peristalsis while the lumen is completely closed by a normal contraction force.

These results indicate that the location at which the pacemaker initiates the

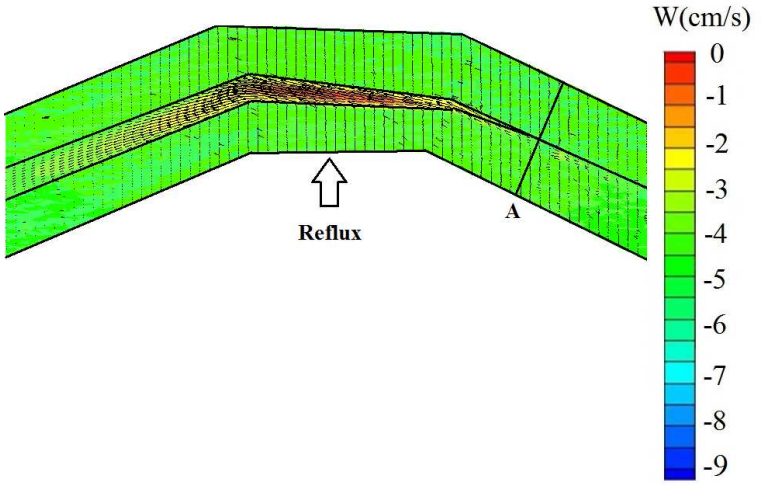

(a)

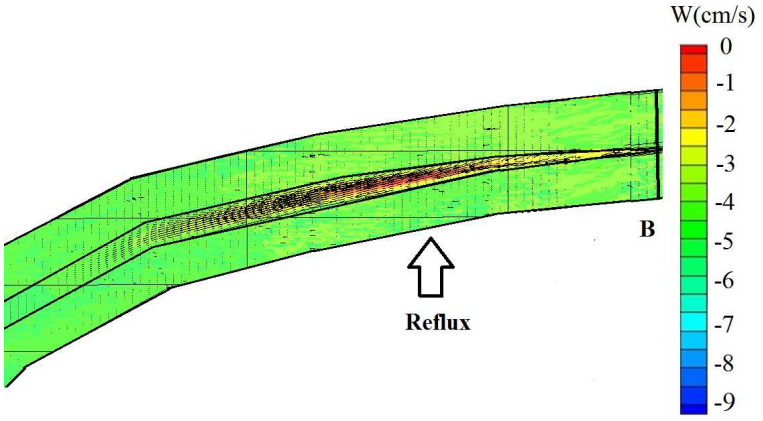

(b)

Figure 6.6: (a) The presence of the reflux behind of the contraction A. (b) The presence of reflux at the behind contraction B.

contraction is crucial. Since the pacemakers are located in many locations in the upper urinary tract, including the renal pelvis, it can be concluded that not all peristaltic movement will cause reflux or high shear stresses at the beginning of the ureter. The magnitude of high shear stress and reflux at the upper part of ureter might be dependent on where the contraction is initiated. There is a large volume of research on the pacemaker activities in different parts of the upper urinary system. In some research, it was concluded that the primary origin of electrical activity at pacemaker sites is the renal pelvis and the pacemaker sites

on the ureter are secondary and described as latent pacemaker sites [6].

6.4.3 Pressure Gradient Distribution

Figure 6.7 shows the magnitude of the urine pressure gradient in the absence of any pressure difference at T = 0.5 seconds. The magnitude of the pressure gradient in the ureter is calculated using post processing software *Tecplot* in the X, Y and Z directions:

$$\overrightarrow{|\bigtriangledown p|} = \sqrt{(\frac{\partial p}{\partial x})^2 + (\frac{\partial p}{\partial y})^2 + (\frac{\partial p}{\partial z})^2} \tag{6.3}$$

Analysis of the urine pressure distribution during peristalsis shows that the maximum pressure gradient in the ureter occurs behind the moving bolus. These results support the experimental data reported by Weinberg [31] showing that the maximum ureteral luminal pressure during peristalsis permanently occurs behind the moving bolus.

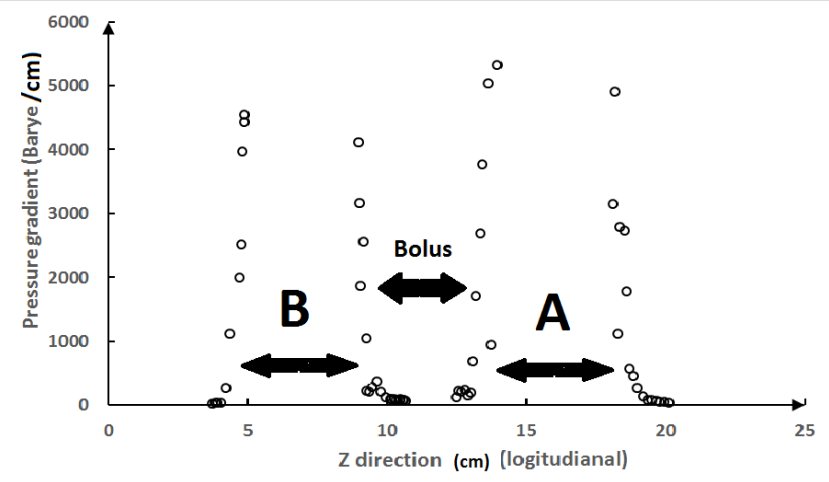

Figure 6.7: Pressure gradient magnitudes immediately before and after contractions A and B.

6.5 The Urodynamic Responses under the Influence of Relaxation Drug

Numerical and experimental analysis of the ureter function under various vasodilators have been examined in prior studies [86, 87]. A highly depressed amplitude of the peristalsis is known to be a consequence of taking vasodilators, which are used to promote the passage of stones through the urinary system. Drugs such as *Alpha Adrenoreceptor Blockers*, $Diclofenac$, $Nifedipine$, $Tamsulosin$ all result in a significant reduction in ureteral contraction pressure of between 20 to 65% [87].

To simulate the depressed ureteral contraction, a zero pressure difference condition was applied between the inlet and outlet of the ureter. Next, a relatively low force of 450 dynes was applied to simulate a weaker contraction, which prevented a complete closure of the lumen area. The contraction velocities for both A and B were 3.5 cm/s.

The aim of this simulation was to assess the possibility of reflux occurring during peristaltic movement in patients with inadequate contraction force resulting from taking vasodilators. This model created a reduced contact pressure describing a deterioration in peristaltic functionality.

Figure 6.8 shows the results from the impaired ureter system with a lower contraction force. It shows the presence of continuous reflux behind the contraction. during peristaltic movement at T = 0.3 and 1 seconds. The results confirm that a patient taking vasodilators is more exposed to the risk of ureteric reflux. Although the urine velocity in this model is to some extent smaller than that seen in a normal contraction, the reflux velocity almost remains unchanged.

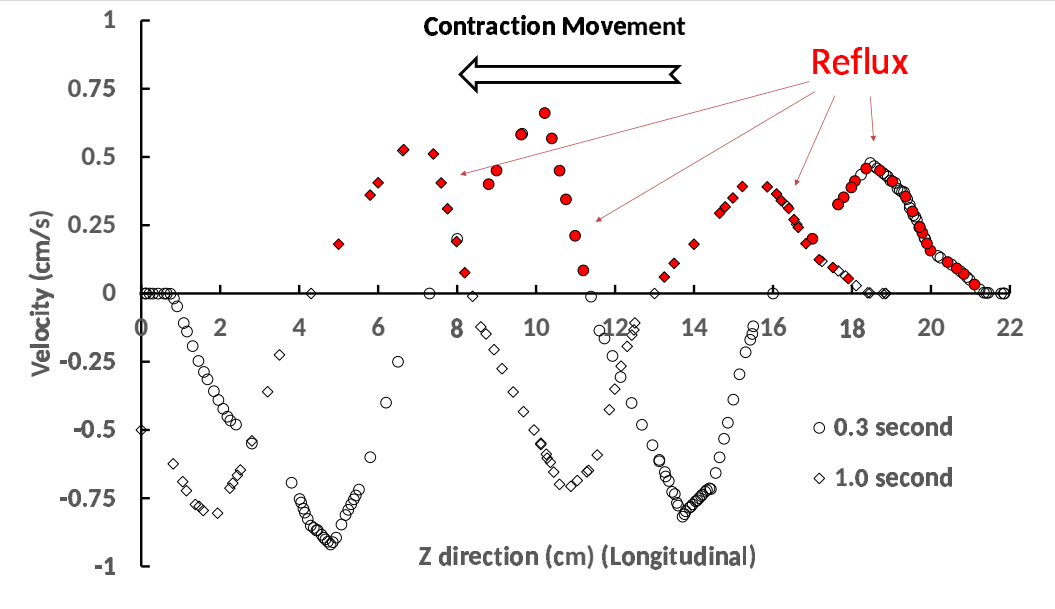

Figure 6.8: Velocity profile in contraction A and B in the ureter.

6.6 Summary

In this chapter, the urodynamic responses were investigated under different conditions, including linear and nonlinear tensile properties, the absence and presence of a pressure difference and finally the low contraction force. The comparison between the nonlinear and linear tensile models for a healthy condition was examined and the results showed that the contraction speed and average urine velocity correlated more closely, as expected in the native system, when nonlinear tensile properties were used. In this aspect, the model of the ureter wall used in this work is therefore more accurate than in previous work.

It was shown that with no pressure gradient, there was an increase of 25% in the maximum wall shear stress at the proximal part of the ureter. These results indicates the importance of PUJ in the urinary system which maintains the pressure difference in the ureter, thus decreases the shear stresses level on the proximal part of ureter. The other important result from this work is to show how an inefficient contraction which doesnt completely collapse the ureteral wall and close the lumen can increase the possibility of continuous reflux during the propagation of peristalsis.

Chapter 7

Conclusions, Limitations and Future Work

7.1 Conclusions

Computational modelling of the ureteral system and its potential application in medicine has received a significant amount of research attention in recent years. The complexity of the physiological phenomena occurring in the ureter makes a comprehensive simulation of every aspect of the urinary system extremely difficult. Consequently developing a computational platform which can simulate the dynamic functionality of the ureteral system more precisely can not only help physicians with a better understanding of the exact mechanisms behind each particular ureteral disease, but also has the potential to be used in the design and development process of a variety of medical components, including ureteral stents and catheters, prior to clinical trials.

In the Introduction 1, a comprehensive literature review on the ureteral physiology was conducted with a focus on several topics: the anatomy of the ureter, the theory behind the ureteral peristaltic function, the effects of various pathological conditions and the effects of a variety of drugs on the ureter functionality. In

this chapter, several experimental studies performed to investigate urodynamics as well as the ureteral peristalsis were discussed. Both invasive and non invasive techniques were described. Subsequently, a number of studies on the computational modelling of the ureteral system were presented and the pros and cons of each study were discussed. It was concluded that many of these studies used a series of assumptions to simplify the model and none of the previous computational simulations of the uretery system modelled essential parameters including the actual geometry of the ureter, viscoelasticity properties of the ureteral wall and the multi-dimensional peristaltic movements. As a result, the aim of the present study was to computationally model a ureteral system that accurately mimics the dynamic functionality of the actual urinary system by incorporating anatomically correct geometry and the non-linear elastic properties of a native ureter.

The objective of this research was met using our in-house Computational Fluid Dynamics (CFD) platform, known as $CgLes$, to model the urine flow, coupled with our in-house Finite Element (FE) platform, known as Y-*code*, to model the non-linear, non-linear properties of the ureteral wall. The discretization of different $Navier$-*stokes* equations terms in control volume method was explained. Then, the projection method and boundary conditions used in $Cgles$ code to solve the fluid domain were described. The simulation of the ureteral wall deformation was conducted using the in-house the Y-code. The stress and strain relationship of the finite element method in the solid domain were explained and the corresponding governing equations were introduced. Finally, to simulate the interaction between the fluid and solid domains, the novel Immersed Boundary (IB) method was introduced to simulate moving boundaries.

Chapter 3 described the simulation of the mechanical properties of the ureteral wall, including tensile properties and geometry. In this chapter, two models of thick walled tube made of linear and non-linear mechanical properties were used. The nonlinear properties of the ureteral wall were integrated into the Y-code using the equivalent strain technique. Both computational and theoretical analyses were conducted and the deformation of each resulting model was evaluated under the same external pressure. It was shown that the computational and theoretical

analysis were in good agreement. The results showed that the radial displacement of the cylindrical shell varies linearly for the elastic and nonlinearly for the non-elastic material. It was concluded that modelling the tube wall as *Hookean* results in an overestimation of the strain when the pressure is increased. It was shown that implementation of nonlinear stress-strain properties was more accurate and more closely matched the native ureteral wall.

In Chapter 4, the development of a more anatomically accurate ureter model geometry was presented, along with a number of approaches to optimise the mesh resolution for this complex model. The $3D$ model of the ureteral system was extracted from CT scan images of an actual human ureter. A mesh quality study was performed to obtain a good compromise between computational cost and precision. Five different solid meshes with various numbers of nodes and elements were examined with the Von Misses stress variable used as a benchmark. For the fluid analysis, similarly, several mesh independent studies were conducted on seven fluid domains, using the central velocity as a bench mark. Our investigation to obtain the optimised grid resolution for the solid and fluid domains has concluded that, after considering the available computational resources, solid Mesh 4 with 6700 elements in the solid part and fluid Domain 4 with $64\times448\times680$ cells over X, Y and Z directions respectively, were the most suitable choices for the computational simulation of the ureteral system with coupled $Cgles$-Y. Finally, an algorithm was developed to create the IB points from the solid part and implemented in the Y-code to enable the extraction of surface nodes from the non-symmetric boundary surface of the ureter.

In Chapter 5, the ureteral peristaltic contraction was simulated by integrating two separate contraction models in order to find which provides the most precise results. One model implemented a constant radial force acting on the cross-sectional area which travels axially along the ureter model with the same speed as the actual human ureter contraction. The second model uses an individual time-window frame for each cross-section along the ureter with the purpose of emulating the relaxation and contraction of individual muscles with fixed positions across time. Finally, a new algorithm was developed in order to implement the concept of IAP into the Y-code. The computational results confirmed the

IAP has a significant impact on the computational results. It was also shown that the time-window-frame contraction model exhibited better agreement with the existing clinical data, compared with the constant radial force contraction model.

In Chapter 6, a comprehensive study was conducted on the uretral peristaltic movement with focus on the urodynamic parameters and urodynamic responses under different pathological conditions. The result showed that the shear stress was significantly higher around the contraction region and that using a linear material for the ureteral wall led to a higher urine velocity in front of the contraction region. For lower amplitude peristalsis, the reflux behind the contraction area remained unchanged.

7.2 Limitations

A clinical study was designed and developed in collaboration with Whipps Cross hospital with the purpose of validating our computational simulation. The aim was to obtain clinical data from several patients, including accurate anatomical geometry of ureter, urodynamic measurements, urine production and pacemaker activities. The ethics application to conduct this study was submitted in November 2015 but was unfortunately rejected at an early stage of the project. Consequently for this study, we had no choice but to use clinical data from the literature, which was not obtained from a specific patient. Although the use of non-patient-specific clinical data did not cause a significant mismatch between the simulated and measured data, it is essential in future studies of this nature to conduct clinical studies on specific individual patients to validate the computational simulation and improve the efficacy of our computational platform. As described in Chapter 1, a peristaltic contraction consists of a multidirectional movement including both longitudinal and circular contractions. In the present study, the longitudinal muscle contraction was not simulated to minimise the complexity of the simulation. Consequently the synchronization between longitudinal and circular contractions was not considered. For the final simulations, the geometry of

ureter was also simplified to a star shape due to limited computational resources. In future study, the longitudinal contraction will also be simulated in the model to create a more realistic peristaltic motion. As described in Chapter 2, the fluid code (*Cgles*) was fully parallelised but the solid code (Y-code) was only partially parallelised. This caused a significant delay to solve the solid part at each time step. Moreover, *Cgles* was parallelised using the MPI method, which is more efficient than the open MP method used in Y-code. Using two different parallelisation methods limited the number of clusters which could be used for this study. For future work, the Y-code needs to be fully parallelised using the MPI method to reduce computational time. The available local computational nodes to run the solid and fluid domains concurrently were limited. Although the UK national supercomputing service (Archer), with more than 4920 computational nodes, was also available for our research, the access to this service was sporadic. For academic research projects Archer only offered limited hours with a limited number of nodes. This limitation to the available computational power constrained the compromise between dense meshes, which maximised accuracy, and coarser meshes that could be completed in a reasonable time frame.

7.3 Future Works

Future work in this area will involve improving the performance of the code, to resolve the limitations caused by high computational cost. To this end, the Y-code must be fully parallelised. This will allow case studies with higher mesh resolution to be completed in a shorter time. In the present study, the longitudinal muscle contraction was not simulated. In an actual ureter, the ureteral peristaltic motions are the result of the combined longitudinal and radial muscle contractions. For the future study, proper synchronization between the longitudinal and radial muscle contraction will be conducted in order to improve the accuracy of the simulation. Conducting a broad range of experimental analyses, using an in-vitro set up, is essential to validate the computational results and evaluate the performance of the code. A wide range of computational studies should be conducted on different ureteral diseases such as vesicoureteral reflux,

ureteral obstruction and megaureter to improve our understanding of the mechanisms behind each particular disease. In addition, the effects of certain drugs on ureteral functionality such as the effect on the frequency and amplitude of the circular muscle or the sequence of peristaltic contraction-relaxation cycles can be simulated numerically.

Appendices

Publications:

- Computational simulation of the urinary system. **G. Hosseini**, E. Avital and J. J. R. Williams. Proceedings of the world congress on Engineering and Computer Science 2012 Vol II, ISBN: 978-988-19252-4-4
- Simulation of the Upper Urinary System. **G. Hosseini**, E. Avital, J. S. Green and J. J. R. Williams, Critical Reviews in Biomedical Engineering, 41(3):259-68 January 2013

Bibliography

[1] CE Constantinou. Renal pelvic pacemaker control of ureteral peristaltic rate. *American Journal of Physiology*, 226(6):1413–1419, 1974.

[2] CE Constantinou. Contractility of pyeloureteral pacemaker system. *Urologia Internationalis*, 33(6):399–416, 1978.

[3] T Morita, G Ishizuka, and S Tsuchida. Initiation and propagation of stimulus from the renal pelvic pacemaker in pig-kidney. *Investigative Urology*, 19(3):157–160, 1981.

[4] K Golenhofen and J Hannappel. Normal spontaneous activity of pyeloureteral system in guinea-pig. *Pflugers Archiv-European Journal of Physiology*, 341(3):257–270, 1973.

[5] S Tsuchida, T Morita, T Harada, and Y Kimura. Initiation and propagation of canine renal pelvic peristalsis. *Urologia Internationalis*, 36(5):307–314, 1981.

[6] A.J. Wein, L. Kavoussi, W. Partin, and C.A. Peters. *Campbell-Walsh Urology*. Elsevier Saunders, 2012.

[7] R. Weiss, M.L. Wagner, and B.F. Hoffman. Localization of the pacemaker for peristalsis in the intact canine ureter. *Invest Urol*, 5:42–48, 1967.

[8] WJ. Lammers, HR. Ahmed, and k. Arafat. Spatial and temporal variations in pacemaking and conduction in the isolated renal pelvis. *American Journal of Physiology*, 270:567–574, 1996.

[9] S. Shimizu. The initiation and propagation of canine pelviureteral contraction studied through visual observation and simultaneous electromyographic recording, translated by nippon heikatsukin gakkai zasshi,. *Japan*, 14:9–16, 1978.

[10] O. Yamaguchi and CE Constantinou. Renal calyceal and pelvic contraction rhythms. *American Journal of Physiology*, 257:788–795, 1989.

[11] R.M. Vadapalli, A. Roychowdhury, A. Kaila, and A. Vadapalli. *Pearls and Pitfalls of CT and MR Urography :What Residents Must Know know, Educational Exhibit, DOI-Link: http://dx.doi.org/10.1594/ecr2014/C-0507.*

[12] F. Hammersen. *Color Atlas of Cytology, Histology and Microscopic Anatomy.* Thieme, 1980.

[13] J. P. Finberg and W. S. Peart. Function of smooth muscle of the rat renal pelvis response of the isolated pelvis muscle to angiotensin and some other substances. *British Journal of Pharmacology*, 39:373–381, 1970.

[14] J. R. Hrynczuk and T. W. Schwartz. Rhythmic contractions in the renal pelvis correlated to ureteral peristalsis. *Investigative Urology*, 13:29–30, 1975.

[15] C. E. Constantinou and J. R. Hrynczuk. The incidence of ectopic peristaltic contractions. *Urologia Internationalis*, 31:476–488, 1976.

[16] C. E. Constantinou and J. R. Hrynczuk. Urodynamics of the upper urinary tract. *Investigative Urology*, 14:233–240, 1976.

[17] F. Kiil. *The Function of the Ureter and Renal Pelvis: Pressure Recordings and Radiographic Studies of the Normal and Diseased Upper Urinary Tract of Man.* W.B. Saunders, 1957.

[18] G.D. Wemyss-Holden, M.R. Rose, S.R. Payne, and H.J. Testa. Non-invasive investigation of normal individual ureteric activity in man. *Journal of Eurology*, 1993.

[19] J.R Woodside and T.A. Borden. The pressure-flow relationship of the normal ureter. *Invest Urol*, 1980.

[20] L. Ohlson. Morphological dynamics of ureteral transport i shape and volume of constituent urine fractions. *American Journal of Physiology*, 256:19–28, 1989.

[21] L. Ohlson. Morphological dynamics of ureteral transport ii prestaltic patterns in relation to flow rate. *American Journal of Physiology*, 256:29–34, 1989.

[22] I. Karnak, al. et, and a. rez. The effects of flow rate, length and external pressure upon the pressure required for fluid to flow through a ureter. *BJU International*, pages 335–338, 2001.

[23] V.J. OConor and P Dawson-Edwards. Role of ureter in renal transplantation: Studies of denervated ureter with particular reference to ureteroureteral anastomosis. *Journal of Urology*, 82:566–572, 1959.

[24] L.R. Wharton. The innervation of the ureter with respect to denervation. *Journal of urology*, 28:639–673, 1932.

[25] E. Schick and E.A. Tanagho. The effect of gravity on ureteral peristalsis. *Journal of Urology*, 1973.

[26] M. Eken, T. Akbas, and T. Arpaci. Spontaneous rupture of the ureter. *SMJ*, 56(2):129–131, 2015.

[27] S.K. Choi, S. Lee, S. Kim, T.G. Kim, and K.H. Yoo. A rare case of upper ureter rupture: Ureteral perforation caused by urinary retention. *Korean J Urol.*, 53(2):131–133, 2012.

[28] E. Pampana, S. Altobelli, M. Morini, and A. Ricci. Spontaneous ureteral rupture diagnosis and treatment. *Case Reports in Radiology*, 2013.

[29] F. Osmon, L. N. George, M. Emil, and N. Peter. A novel videomicroscopic technique for studying rat ureteral peristalsis in vivo. *world J Urology*, 27(2):256–270, 2009.

[30] R. Woodburne and J. Lapides. The ureteral lumen during peristalsis. *American Journal of Anatomy*, 133:255–258, 1972.

[31] S. L. Weinberg. Ureteral function: Ii. the ureteral catheter and the urometrogram. *Investigative Urology*, 12(4):255–261, 1975.

[32] B. Tilling and C. E. Constantinou. Videomicroscopic imaging of ureteral peristaltic function in rats during cystometry. *Journal of Pharmacological and Toxicological*, 35:191–202, 1996.

[33] D. Kim, G. T. , Anthony, and J.r. Keeley. The role of ureteral relaxation in the propotion of stone passage. In *Annual International Urolithiasis Research Symposium.*, Bristol Urological Institute, Southmead Hospital, Westbury-on-Trym, Bristol, 2007.

[34] CA Lewis, MJ Coptcoat, SSC Carter, AJW Hilson, JEA Wickham, and PJR Shah. Radionuclide imaging of ureteric peristalsis. *British Journal of Urology*, 63(2):144–148, FEB 1989.

[35] U. Patel and MJ Kellett. Ureteric drainage and peristalsis after stenting studied using colour doppler ultrasound. *Br J Urol*, 77:530–535, 1996.

[36] H. Roshani, NF. Dabhoiwala, T. Dijkhuis, Kurth KH., and Lamers WH. An in vivo endoluminal ultrasonographic study of peristaltic activity in the distal porcine ureter. *Journal of Urology*, 163:602–606, 2000.

[37] R. Venkatesh, J. Landman, and SD Minor. Impact of a double-pigtail stent on ureteral peristalsis in the porcine model : Initial studies using a novel implantable magnetic sensor. *J Endourol*, 19:170–176, 2005.

[38] H. Roshani, NF. Dabhoiwala, and S. Tee. A study of ureteric peristalsis using a single catheter to record emg, impedance, and pressure changes. *Tech Urology*, 5:61–66, 1999.

[39] U. Ulmsten and J. Diehl. Investigation of ureteric function with simultaneous intraureteric pressure recordings and ureteropyelography. *Radiology*, 117:283–289, 1975.

[40] A. Shafik. A study of the ureteric pressure profile in the normal and pathologic ureter. *Scand J Urol*, 32:14–19, 1998.

[41] A.J. Young. Evaluation of novel technique for studying ureteral function in-vivo. *Journal of Endourology*, 21(1), 2007.

[42] H. Watanabe, Y. Nakagawa, and M. Uchida. Tests to evaluate the mechanical properties of the ureter technical report. *Americal Society for Testing and Materials*, pages 275–282, 1994.

[43] F.C.P. Yin and Y.C Fung. Mechanical properties of isolated mammalian ureter segments. *American Journal of Physiology*, 221(5), 1971.

[44] YC Fung. Elasticity of soft tissue in simple elongation. *Am J Physiol*, 213(6):1532–1544, 1967.

[45] JT Apter and P Mason. Dynamic mechanical properties of mammalian ureteral muscle. *American Journal of Physiology Published*, 221:266–272, 1971.

[46] JT Apter, WW Graessley, and Biophys J. A physical model for muscular behaviour. *Biophys J*, 1970.

[47] J. C. Burns and T. Parkes. Peristaltic motion. *Journal of Fluid Mechanics*, 29:731–743, 1967.

[48] M. Manton. Long-wavelength peristaltic pumping at low reynolds number. *Journal of Fluid Mechanics*, 68:63–75, 1975.

[49] T. Zien and S. Ostrach. A long wave approximation of peristaltic motion. *Journal of Biomechanics*, 3:63–75, 1970.

[50] L. M. Srivastava and V. P. Srivastava. Peristaltic transport of a physiological fluid. part i, ii and iii. *Biodheology*, 20:153–185, 1983.

[51] A. Shapiro, M. Jaffrin, and S. Weinberg. Peristaltic pumping with long wavelengths at low reynolds number. *Journal of Fluid Mechanics*, 37:799–825, 1969.

[52] S. Takabatake and K. Ayukawa. Numerical study of two-dimensional peristaltic flows. *Journal of Fluid Mechanics*, 122:439–465, 1982.

[53] S. Takabatake, K. Ayukawa, and A. Mori. Peristaltic flow in circular cylindrical tubes under finite wavelengths and finite re. *Journal of Fluid Mechanics*, 193:267–283, 1988.

[54] Bahman Vahidi and Nasser Fatouraee. A numerical simulation of peristaltic motion in the ureter using fluid structure interactions. In *Annual International Conference of the IEEE Engineering in Medicine and Biology Society*, pages 1168–1171, 2007.

[55] B. V. Rathish-Kumar and K. B Naidu. A numerical study of peristaltic flow. *Computers and Fluids*, 24:161176, 1995.

[56] Q. Xiao and M. Damodaran. A numerical investigation of peristaltic waves in circular tubes. *International Journal of Computational Fluid Dynamics*, 16(2):201–216, 2002.

[57] M. Graw and H. Engelhardt. Simulation of physiological ureteral peristalsis. *Urology International*, 41(1):1–8, 1986.

[58] Jimnez-Lozano. *Peristaltic Flow with A.J.pplication to Ureteral Biomechanics*. PhD thesis, Notre Dame university, Indiana, 2009.

[59] B. Vahidi and N. Fatouraee. A biomechanical simulation of ureteral flow during peristalsis using intraluminal morphometric data. *Journal of Theoretical Biology*, 298:42–50, APR 7 2012.

[60] R Glowinsky. *Fictitious Domain Methods for Viscous Flow Simulation,Computational Fluid Dynamics Review*. Wiley, 1995.

[61] R.V. Loon, P.D. Anderson, F. N Van de Vosse, and S. J. Sherwin. Comparison of various fluidstructure interaction methods for deformable bodies. *ComStruc*, 85(11-14):833–843, 2007.

[62] C.W. Hirt, A.A. Amsden, and J.L. Cook. An arbitrary lagrangianeulerian computing method for all speeds. *Comp Phys*, 14:227–253, 1974.

[63] J. Donea, S. Jiuliani, and J.P. Halleux. An arbitrary lagrangianeulerian finite element method for transient dynamic fluidstructure interactions. *Comput Method Appl Mech Eng*, 33:689723, 1982.

[64] W.K. Hughes, T.J.R.and Liu and T. Zimmerman. Lagrangianeulerian finite element formulation for incompressible viscous flow. *Comput Method Appl Mech Eng*, 29:329349, 1981.

[65] B. Houa, X. Baib, C. Xing, and B. Lub. Label-free detection of single-stranded dna binding protein based on a cantilever array. *Talanta*, 109:173–176, 2013.

[66] C. Peskin. Flow patterns around heart valves: A numerical method. *Journal of Computational Physics*, 10:252–271, 1972.

[67] C.S. Peskin. Numerical analysis of blood flow in the heart. *J. Comput. Phys*, 25:220, 1977.

[68] C.S Peskin and D.M. McQueen. *Fluid Dynamics of the Heart and Its Valves, In Case Studies in Mathematical Modeling: Ecology, Physiology, and Cell Biology.* PrenticeHall, Englewood Cliffs, 1996.

[69] M.E. Rosar. *A Three-Dimensional Computer Model for Fluid Flow through a Collapsible Tube.* PhD thesis, Courant Institute of Mathematical Sciences, New York University, 1994.

[70] K.M Arthurs, L.C Moore, C.S Peskin, and E.B Pitman. Modeling arteriolar flow and mass transport using the immersed boundary method. *Comput. Phys*, 147:402, 1998.

[71] C. Ji, A. Munjiza, and J.J.R. Williams. A novel iterative direct-forcing immersed boundary method and its finite volume applications. *Journal of Computational Physics*, 231(4):17971821, 2012.

[72] T. G. Thomas and J. J. R. Williams. Development of a parallel code to simulate skewed flow over a bluff body. *Journal of Wind Engineering and Industrial Aerodynamics*, 67(8):155–167, 1997.

[73] A. Munjiza. *A Combined Finite/Discrete Element Method*. John Wiley & sons Ltd, 2004.

[74] J.H Ferziger and M. Peric. *Computational Methods for Fluid Dynamics*. Springer, 2002.

[75] A.J Chorin. Numerical solution of the navier-stokes equations. *Mathematics of Computation*, 22:745–762, 1968.

[76] R. Temam. Sur l'approximation de la solution des equations de navier-stokes par la methode des pas fractionnaires (ii). *Rational Mechanics and Analysis*, 33:377–385, 1969.

[77] A. Cristallo and R. Verzicco. Combined immersed boundary/large-eddy-simulations of incompressible three dimensional complex flows. *77*, 4:3–26, 2006.

[78] A.P. Boresi, R.J. Schmidt, and O.M. Sidebottom. *Advanced Mechanics of the Material*. John Wiley & sons Ltd, 1993.

[79] Carlos G. J., F. Javier Martinez-Reina, Domingo Cruz, J. Blas Pagador, Francisco M. Sanchez-Margallo, and Federico Soria. Fluid structural analysis of urine flow in a stented ureter. *Computational and Mathematical Methods in Medicine*, 2016.

[80] T. Shashikant and R. S Bindu. Effect of mesh size on finite element analysis of plate structure. In *International Journal of Engineering Science and Innovative Technology*, 2015.

[81] J.A. Ross, P. Edmond, J. Coull, and J. Griffiths. Observations on the physiology of the human renal pelvis and ureter. *Journal of Urology*, 1967.

[82] S. Boyarsky. *Urodynamics: Hydrodynamics of the Ureter and Renal Pelvis*. Academic Press, 1971.

[83] K.T. Bush, D.A. Vaughn, X. Li, M.G. Rosenfeld, D.W. Rose, S.A. Mendoza, S.K. Nigam, and Biol Dev. Development and differentiation of the ureteric

bud into the ureter in theabsence of a kidney collecting system. *Dev Biol*, 298(2):571–584, 2006.

[84] CE. Constantinou, JJ. Granato, and DE. Govan. Dynamics of the upper urinary tract: V-accommodation in the rate and stroke volumes of ureteral peristalsis as responses to transient alterations in urine flow rate. *Invest Urology*, 29:249–264, 1974.

[85] I. Granet. *Fluid Mechanics*. Prentice Hall, 1996.

[86] I. Mudraya and L Khodyreva. Ureteric function and upper urinary tract urodynamics in patients with stones in kidney and ureter. Technical report, Research insititue of urology Russia, 2012.

[87] K. Davenport, A.G. Timoney, and F.D. Keeley. The role of ureteral relaxation in the promotion of stone passage. *Renal Stone Disease, 1" Annual International Urolithiasis Research Symposium*, 2007.